Report Title: New Mechanistic Models of Long Term Evolution of Microstructure and Mechanical Properties of Nickel Based Alloys

Type of Report: Final Scientific/Technical Report

Reporting Period Start Date: 01/01/2015
Reporting Period End Date: 12/31/2017

Principal Authors: Jamie Kruzic, Professor
Oregon State University
Corvallis, OR 97331
541-908-5178
jamie.kruzic@oregonstate.edu

T. Matthew Evans, Associate Professor
Oregon State University
Corvallis, OR 97331
541-737-8535
matt.evans@oregonstate.edu

P. Alex Greaney, Assistant Professor
University of California, Riverside
Riverside, CA 92521
951-827-2884
agreaney@engr.ucr.edu

Report Date: 5/15/2018
DOE Award Number: DE-FE0024065

Submitting Organization: Oregon State University
Office of Post Award Administration
PO Box 1086
Corvallis, OR 97339-1086
DUNS Number: 053599908

Disclaimer

Abstract

The report describes the development of a discrete element method (DEM) based modeling approach to quantitatively predict deformation and failure of typical nickel based superalloys. A series of experimental data, including microstructure and mechanical property characterization at 600°C, was collected for a relatively simple, model solid solution Ni-20Cr alloy (Nimonic 75) to determine inputs for the model and provide data for model validation. Nimonic 75 was considered ideal for this study because it is a certified tensile and creep reference material. A series of new DEM modeling approaches were developed to capture the complexity of metal deformation, including cubic elastic anisotropy and plastic deformation both with and without strain hardening. Our model approaches were implemented into a commercially available DEM code, PFC3D, that is commonly used by engineers. It is envisioned that once further developed, this new DEM modeling approach can be adapted to a wide range of engineering applications.

Table of Contents

List of Figure Captions

List of Tables

1. Executive Summary

This project developed a novel discrete element method (DEM) based modeling approach to quantitatively predict deformation and failure of nickel-based superalloys. Ni-based superalloys are important for a wide variety of power generation systems, including industrial gas power turbines, advanced ultra-super critical steam turbines, nuclear reactors, and aerospace turbine engines. A potential advantage of DEM when modeling deformation and failure originates from its stochastic formulation that naturally captures local microstructure and property variations because heterogeneity is an integral part of DEM assemblies. This presents a potential opportunity for DEM to simulate failure processes in a more spontaneous and realistic manner than continuum-based approaches. While the technical effectiveness of the model is not currently ready for widespread use, this project demonstrated an important first step and proof of principle. Feasibility was considered by incorporating our model into a commercially available DEM code, *PFC*^{3D} v5, that is commonly used by engineers. It is envisioned that once further developed, this new modeling approach can be adapted to a wide range of engineering applications.

2. Project Accomplishments and Summary of Activities

This is the final report submitted for this project. The scope of this project was to create and validate a discrete element method (DEM) based modeling approach to quantitatively predict deformation and failure of typical nickel-based superalloys. The project ended on December 31, 2017 after a no-cost extension was requested and granted because of delays that were incurred because 1) we were not able to hire the post-doctoral scholars until midway through the first quarter and 2) one post-doctoral scholar left the project early. The no-cost extension allowed Dr. Agnieszka Truszkowska to complete the project.

Table 1 summarizes the status of the project milestone objectives for the final report, and progress against those milestones. The table is followed by a discussion of the project accomplishments and activities. The report will describe the experimental data that was collected for determining inputs for the model, the data that was collected for validation of the model, and finally a description of the model development and validation against experimental data.

Table 1 Milestones

Milestone Description	Planned Completion Date	Actual Completion Date	Status
Microstructure and material parameter inputs for model have been determined.	12/31/16	12/31/17	Complete
DEM model developed and validated	12/31/16	12/31/17	Complete for anisotropic elastic single crystals and isotropic non-hardening and hardening plasticity. Polycrystal and creep behavior are still being developed.

2.1. Microstructure and material parameter characterization

2.1.1. *Model Nickel Based Superalloy Nimonic 75*

We selected a relatively simple, model solid solution Ni-20Cr alloy (Nimonic 75). Nimonic 75 is ideal for this study because it is a certified tensile and creep reference material (Gould and Loveday, 1990; Ingelbrecht and Loveday, 2000), and we acquired certified rods of material from LGC Standards. The as-received microstructure did not have the expected microstructure of grain boundary carbides, so we annealed the as-received Nimonic 75 at 600 °C for 400 hours to observe the microstructure evolution. The annealed microstructure has been characterized and compared with the as-extruded microstructure by optical microscopy (OM), scanning electron microscopy (SEM), energy dispersive x-ray spectroscopy (EDS), and electron backscatter diffraction (EBSD).

2.1.2. *Qualitative Microstructure and Phase Identification*

Figure 1 shows the optical microscopy comparison of the microstructures before and after annealing. It is found that the number of intergranular carbides is significantly increased after the annealing treatment to give the expected microstructure for Nimonic 75. Figure 2 shows the phase identification by SEM/EDS mapping. Three phases exist in the as-received state (Figure 2a): Ni-20%Cr matrix phase (Circle A), inter- & intra-granular Cr-rich carbides (Arrows B) and large polyhedron-shaped Ti nitrides (Arrow C). After heat treatment, Cr-rich carbides (Arrows B, Figure 2a) changes to CrMn-rich carbides (Arrows B, Figure 2b) and they are mostly distributed along the grain boundaries. The Ti nitride phase (Arrow C, Figure 2a) changed to TiCrMn carbonitride (Arrow C, Figure 2b).

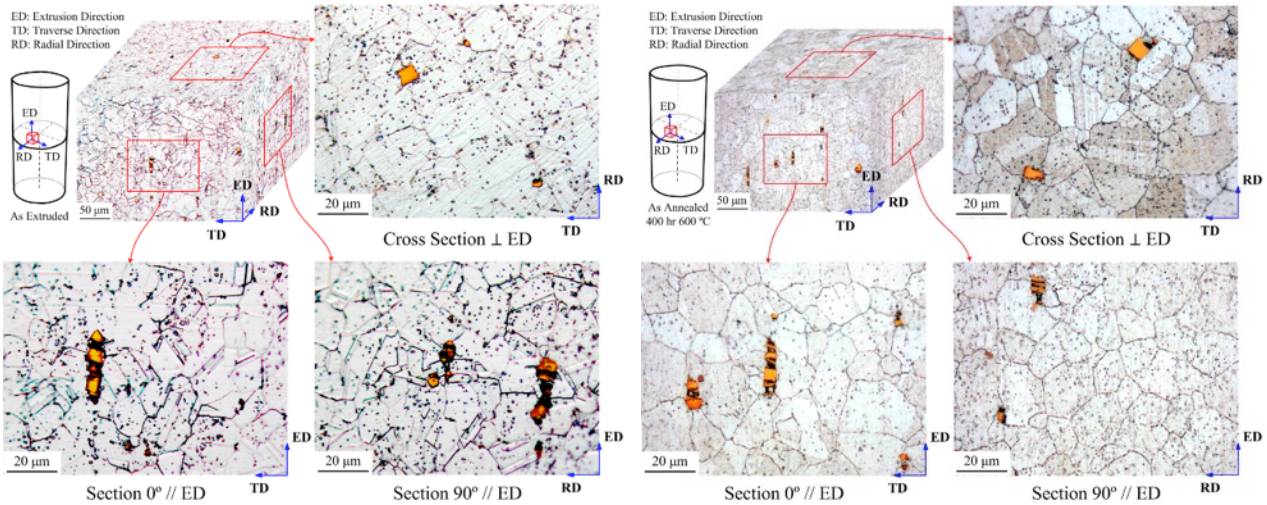

(a) (b)

Figure 1. Optical microstructure of Nimonic 75 on three orthotropic planar sections: (a) as-received; (b) annealed at 600 °C for 400 hours.

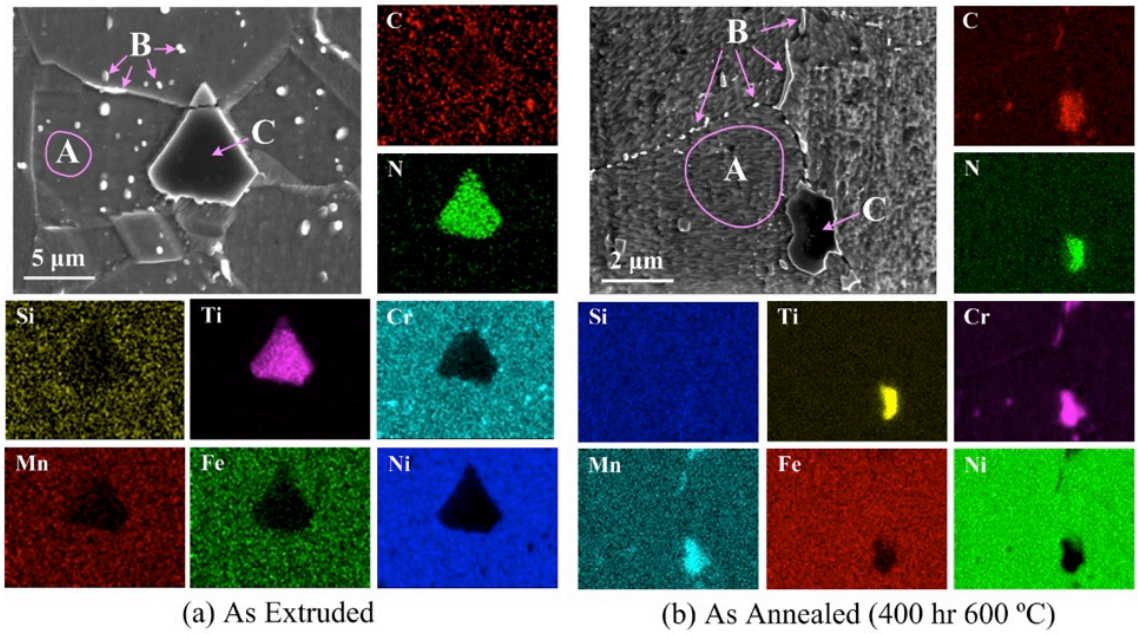

Figure 2. Phase identification by SEM/EDS mapping: (a) as-received; (b) annealed at 600 °C for 400 hours.

2.1.3. *Intergranular and Intragranular Carbides*

As shown in **Error! Reference source not found.**a, before annealing the carbides are found more frequently inside grains and twins rather than at boundaries. Intergranular carbides are sparsely distributed along grain boundaries (GBs) and triple junctions (TJs). Carbides can also be found at twin fronts (TFs) and coherent twin boundaries (TBs), but are few in quantity. After annealing (**Error! Reference source not found.**b), carbides are observed most frequently at the grain boundaries. Carbides at twin fronts (TFs) and twin-grain boundaries (TGBs) also significantly increase in number with fewer found at coherent twin boundaries (CTBs). Carbides can also be found at twin-twin boundaries (TTBs), which is rarely observed before annealing.

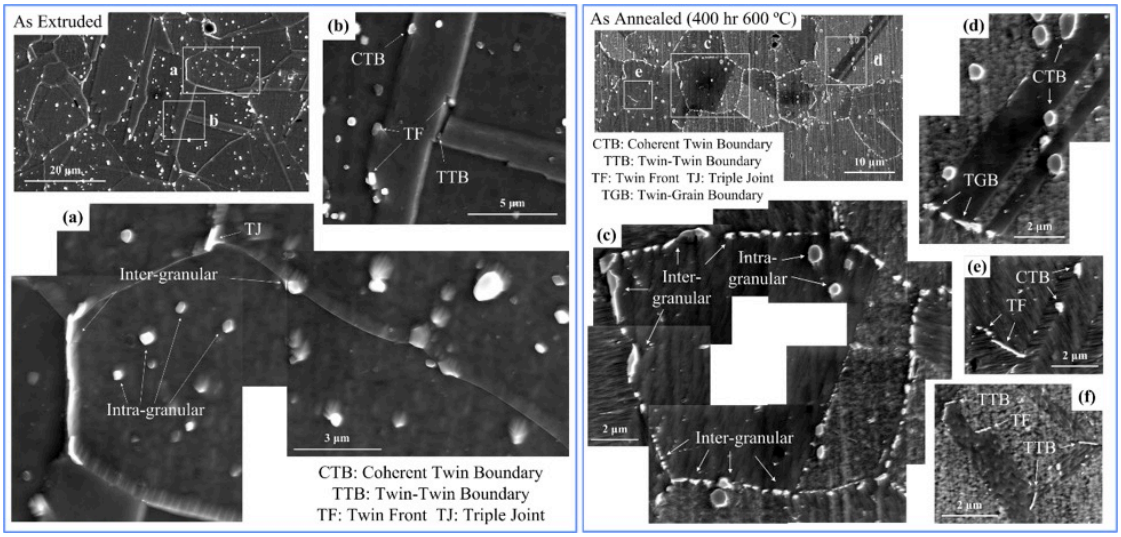

Figure 3. SEM observation of carbides before (a) and after (b) annealing at 600 °C for 400 hours.

2.1.4. *Grain Boundary Segregation*

Figure 4a shows a HR-STEM EDS mapping of a triple joint in the as-received state. No chemical segregation in shown at grain boundaries but a small decrease of Ni and a small increase of Cr are shown at the triple joint. Figure 4b shows a HR-SEM EDS mapping of special grain boundaries after annealing treatment. The special grain boundary has a misorientation of 30°/<1 1 1>, which is vulnerable to creep void initiation (Zhang and Field, 2013).

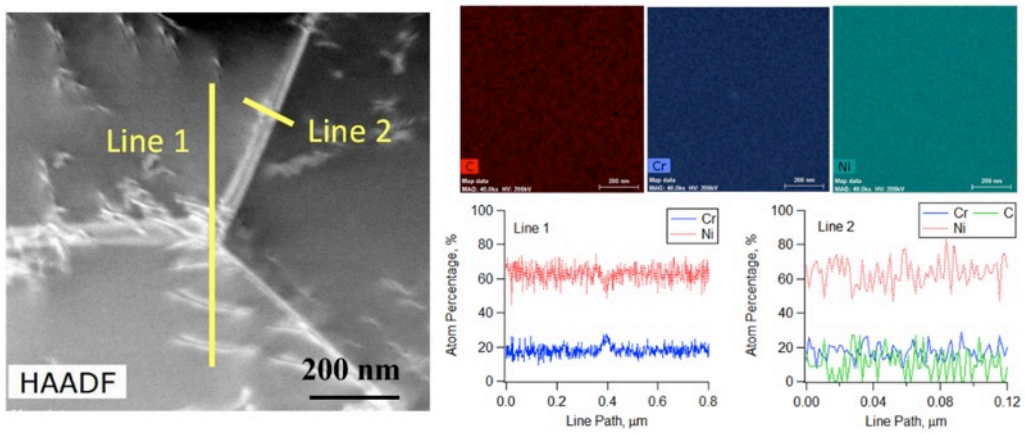

(a) As Extruded (HR-STEM EDS Mapping)

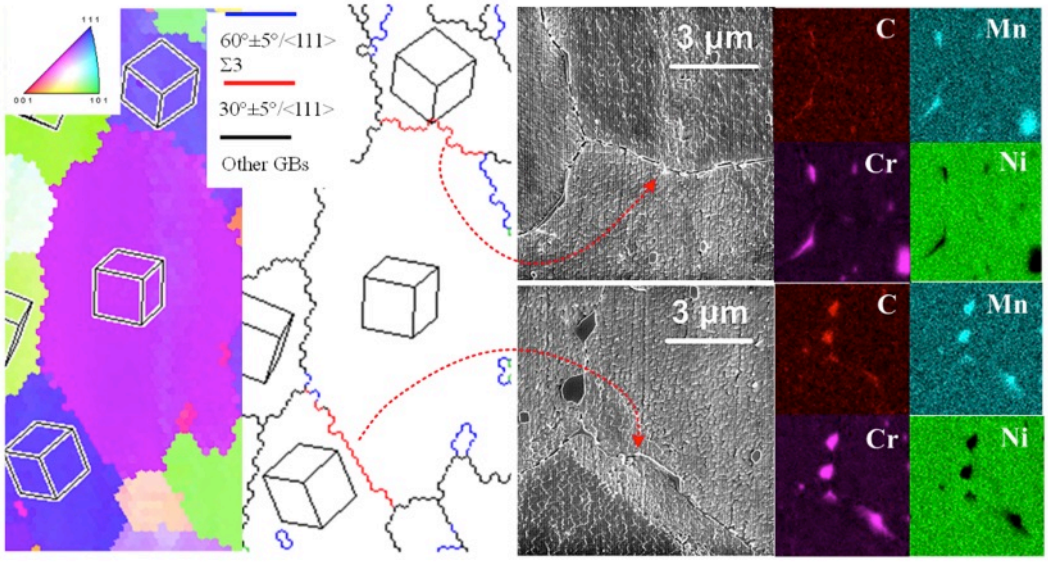

(b) As Annealed - 400 hr 600 ºC (HR-SEM EDS Mapping)

Figure 4. (a) HR-STEM EDS mapping of a triple joint in the as-received state. (b) HR-SEM EDS mapping of special grain boundaries (30°/<1 1 1>) after annealing at 600 °C for 400 hours.

2.1.5. *Statistical Quantification of Grain Size and Orientation*

Statistical quantification of the microstructure was obtained by EBSD mapping (Figure 5). Distributions of grain size & shape (Figure 6), grain orientation (Figure 7), and grain boundary misorientation (Figure 8) have been generated for both the as-received and annealed states.

Grain size and shape distributions do not change after annealing treatment if twins are not considered. Annealing twins may grow by recrystallization as indicated by the slight increase of small grain area in Fig. 6a. From the pole and inverse pole figures (Figure 7), a weak FCC <1 1 1>-<1 0 0> fiber texture is shown in the material. The texture is further weakened after annealing treatment. The misorientation distribution of grain boundary shows slight decreases of 60° <1 1 1> (∑3) primary and 40°/<1 0 1> (∑9) secondary twin boundaries (TBs). This is likely ascribed to the coalescence of coherent twin boundaries during the growth of annealing twins. The measured grain size distribution enables our polycrystal tessellation described later in the report.

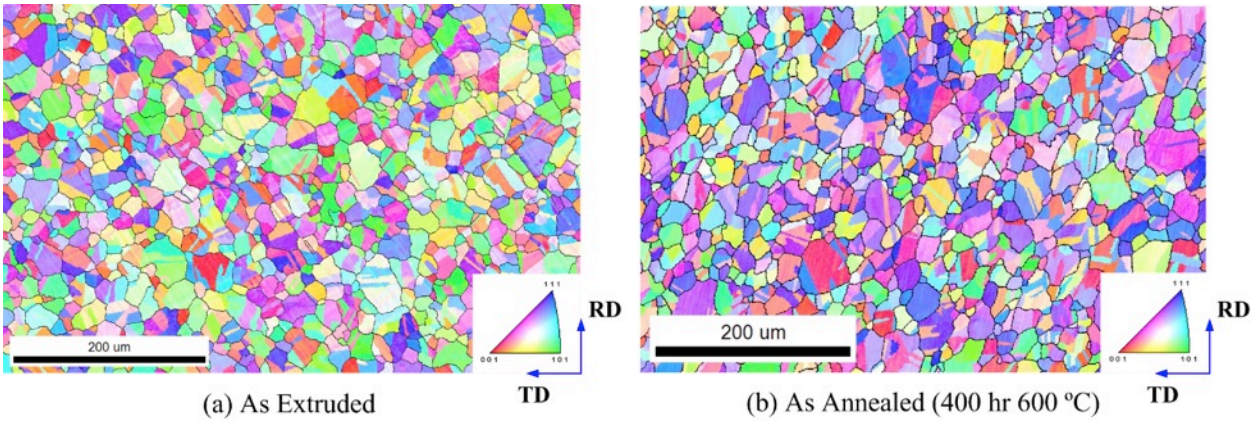

Figure 5. Crystal orientation map obtained by EBSD: (a) as-received; (b) annealed at 600 °C for 400 hours.

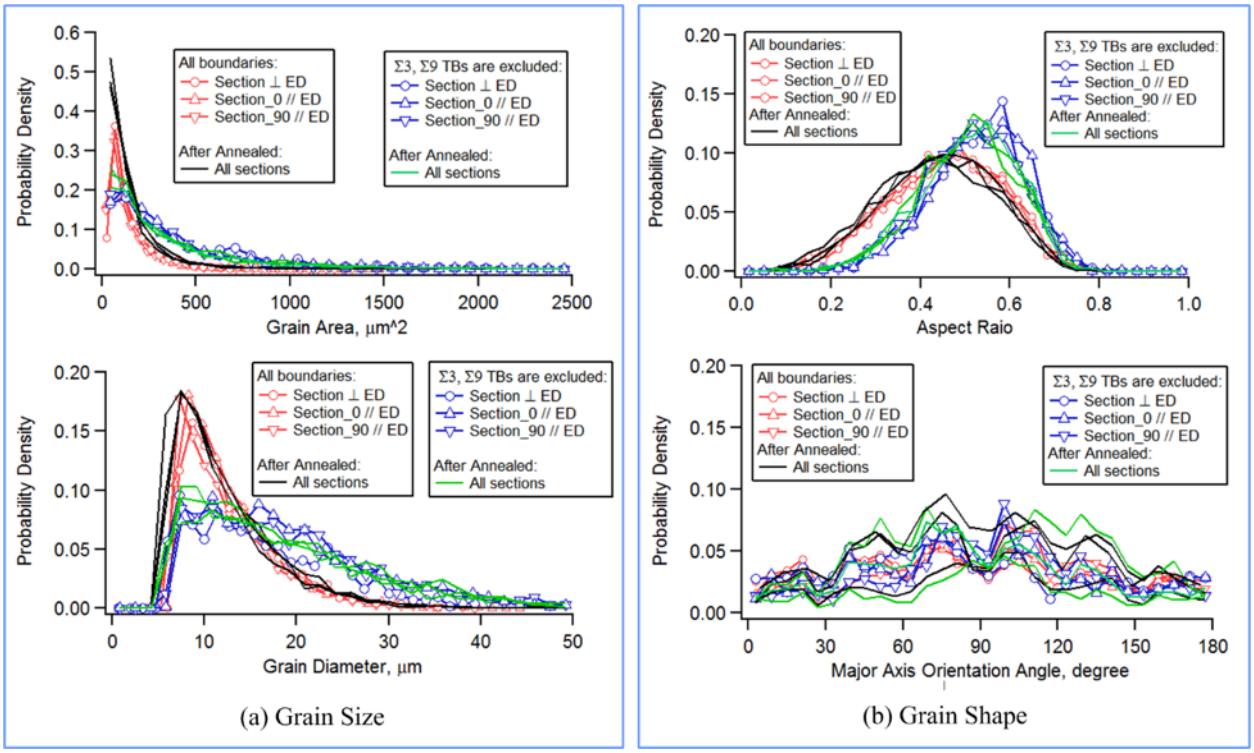

Figure 6. Grain size and grain shape distributions: (a) as-received; (b) annealed at 600 °C for 400 hours.

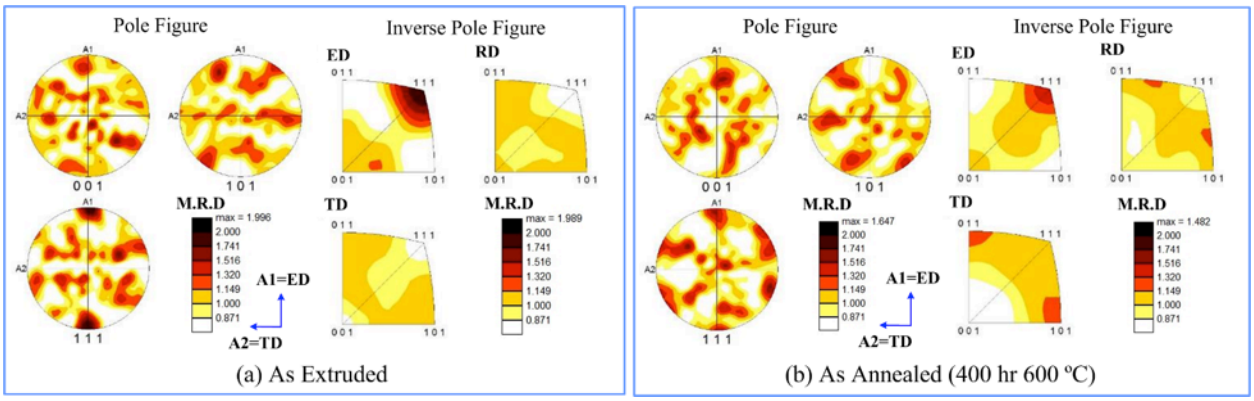

Figure 7. Grain orientation distribution: (a) as-received; (b) annealed at 600 °C for 400 hours.

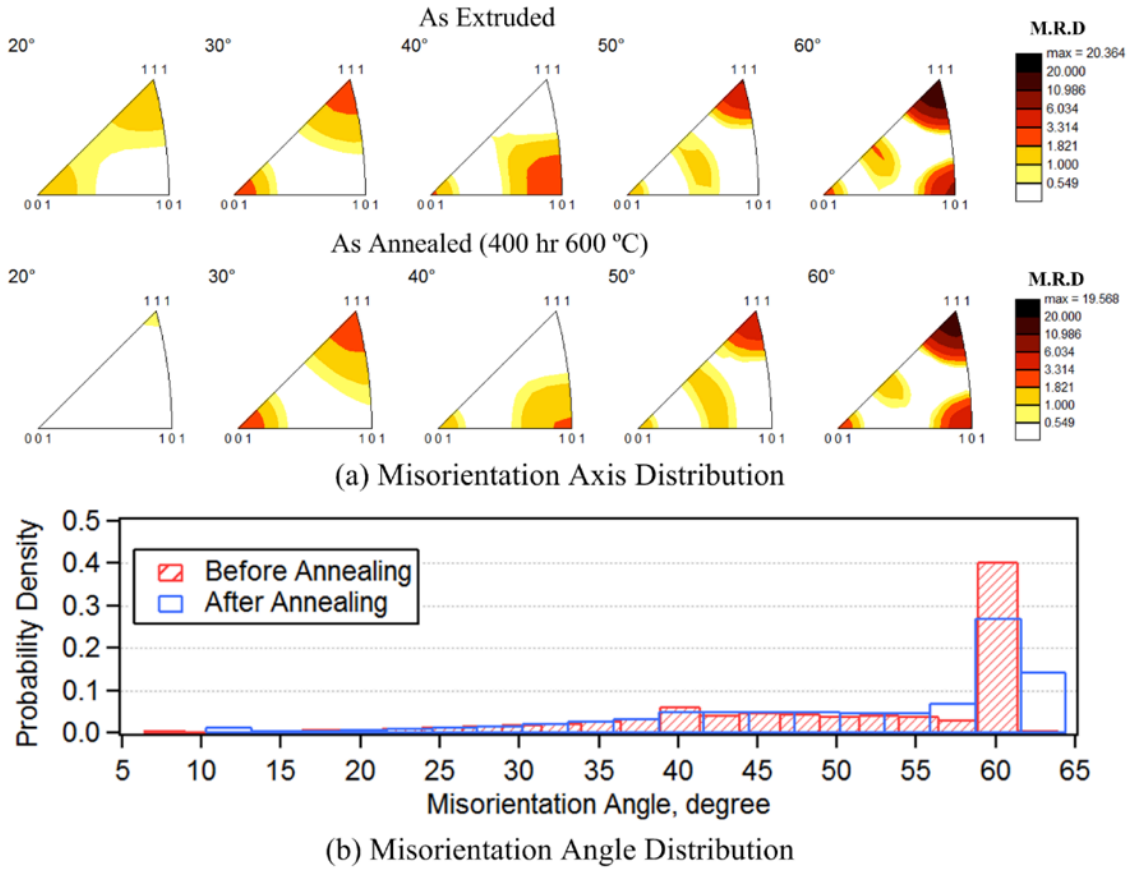

Figure 8. Grain boundary misorientation before and after annealing: (a) misorientation axis distribution; (b) misorientation angle distribution.

2.1.6. *Elastic-Plastic Behavior of Nimonic 75 Subjected to Monotonic Tension at 600 ºC*

Quasi-static monotonic tension experiments for Nimonic 75 were conducted across a wide range of strain rates at the temperature of 600 ºC. The short-term elastic-plastic behavior of the material and its sensitivity to strain rate were evaluated. Critical parameters for DEM model input were determined, including polycrystalline Young's modulus and proportional limit, and

single-crystal critical resolved shear stress (CRSS). In addition, we have identified important features of visco-plastic deformation, work hardening, and dynamic softening. The detailed results are presented in the following sections.

2.1.6.1. Materials and Experiments

We annealed the as-received certified reference material Nimonic 75 at 600 °C for 400 hours to obtain the desired microstructure of grain boundary carbides. A dog-bone cylinder-shaped testing specimen was designed for the high-temperature tension experiment. The geometry and dimensions of a typical tensile testing specimen are shown in Figure 9a. The gage section and the grip section of the high-temperature testing specimen were designed to be long enough to allow the usage of the induction heating copper coil (Figure 9b). Epsilon 3448 high-temperature extensometer with a gage length of 25 mm was used to measure the engineering strain (Figure 9b). Three K-type thermocouples were attached on the specimen surface by spot welding at three locations in the gage section: the midpoint, 12.5 mm above the midpoint, and 12.5 mm below the midpoint (Figure 10a). Before each test, the induction copper coil was tuned to ensure a uniform temperature distribution within the gage section (Figure 10b).

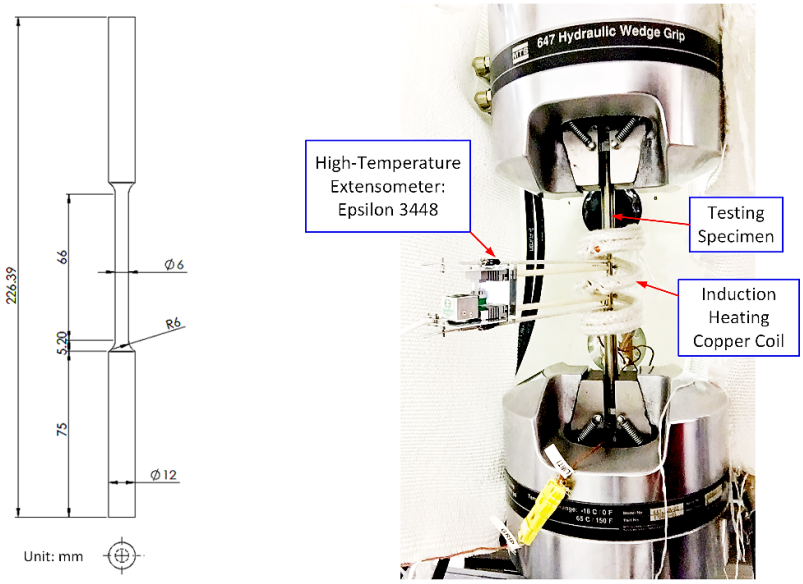

(a) (b)

Figure 9 (a) Geometry and dimension of tensile testing specimen; and (b) the experimental setup for monotonic tension at high temperature.

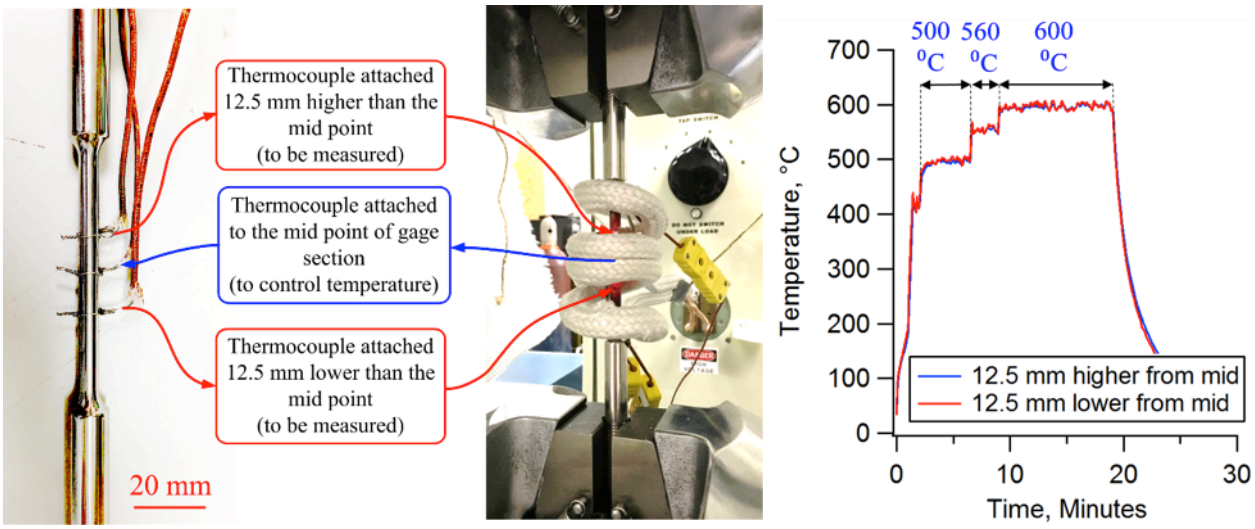

Figure 10. (a) High-temperature tensile specimen and conduction copper coil to heat up the specimen. (b) Verification of uniform temperature distribution within the gage section.

Monotonic tension was applied by position control at four constant speeds: 0.001 mm/s, 0.01 mm/s, 0.1 mm/s, and 1 mm/s. Load and position signals were recorded by the load frame. The engineering strain was measured by high-temperature extensometer. After heating up to 600 ºC, each specimen was loaded up to a tensile strain of 10% and unloaded. The choice to unload the specimen at a tensile strain of 10% is to prevent contact of the extensometer arms with the induction heating coil when the arms open during tension. After the experiment was completed, the actual strain rate was calculated from the measured engineering strain. For each strain rate, we conducted two tests to evaluate the repeatability.

2.1.6.2.Experimental Results

Figure 11 presents the stress-strain response of Nimonic 75 monotonically tensioned at 600 ºC across four strain rates: 1.70×10^{-5} /s (Figure 11a), 1.45×10^{-4} /s (Figure 11b), 1.43×10^{-3} /s (Figure 11c), and 1.43×10^{-2} /s (Figure 11d). True stress and true strain were also calculated and plotted in Figure 11as well. The true stress and true strain are calculated from the engineering stress and engineering strain using the simple relations:

$$\sigma = S(1+e) \qquad \text{Equation 1}$$

$$\varepsilon = \ln(1+e) \qquad \text{Equation 2}$$

where S and e are engineering stress and engineering strain, respectively. σ and ε are true stress and true strain, respectively. In Figure 11a-d, an inset that magnifies the initial yielding region of the stress-strain curve is embedded. From Figure 11, the strain rate effect on the elastic-plastic behavior of the material can be clearly observed.

2.1.6.3. Polycrystalline Young's Modulus, Proportional Limit, and Single-Crystal Critical Resolved Shear Stress (CRSS)

Young's modulus can be experimentally determined by dynamic or static methods. Dynamic modulus can be obtained from a specimen vibrated in the flexural mode. Static modulus can be defined as the slope of a straight line that best fits the linear elastic portion of the stress-strain curve, which is obtained from specimen subjected to monotonic tension at a quasi-static loading rate. Since static and dynamic methods are associated with isothermal and adiabatic processes, respectively, dynamic modulus is slightly greater than static modulus, being ~0.2% greater at room temperature and ~1% greater at 1000 °C (Betteridge and Heslop, 1974). The proportional limit represents the termination of the linear elastic portion of the stress-strain behavior and is an indication of the onset of plastic deformation. There is no universal mathematical method to determine the proportional limit.

To reliably determine the Young's modulus and the proportional limit from the experimental data, we have proposed the following analytical procedure. We linearly fit the stress-strain data in a section starting from zero stress to a "high-bound" stress level using the least squares method. The slope of the least square regression line is calculated as Young's modulus for this stress-strain section. The coefficient of determination (R^2) that indicates how well data fit the regression line can be calculated as:

$$R^2 = 1 - \frac{SS_{res}}{SS_{tot}} = 1 - \frac{\sum_i (y_i - f_i)^2}{\sum_i (y_i - \bar{y})^2} \qquad \text{Equation 3}$$

where f_i is the fit value and $\bar{y} = \frac{1}{n}\sum_{i=1}^{n} y_i$ is the mean of the data in the fitting section. By fixing the starting point (zero stress) and increasing the "high-bound" stress level, we fit a series of stress-strain sections and obtain the regression line slope and the R^2 as a function of the increasing "high-bound" stress level. As a higher R^2 indicates better fitting, the "high-bound" stress corresponding to the highest R^2 is thus taken as the proportional limit. The associated slope of the regressed line is taken as the Young's modulus of the material tested at the specific loading condition.

Based on the analytical procedure described above, the determination of Young's modulus and proportional limit for Nimonic 75 tested at 600 ºC is illustrated in Figure 12. The Young's modulus and proportional limit corresponding to each strain rate are summarized in Table 2 and Figure 14a. It is found the strain rate effects on the Young's modulus and proportional limit are trivial.

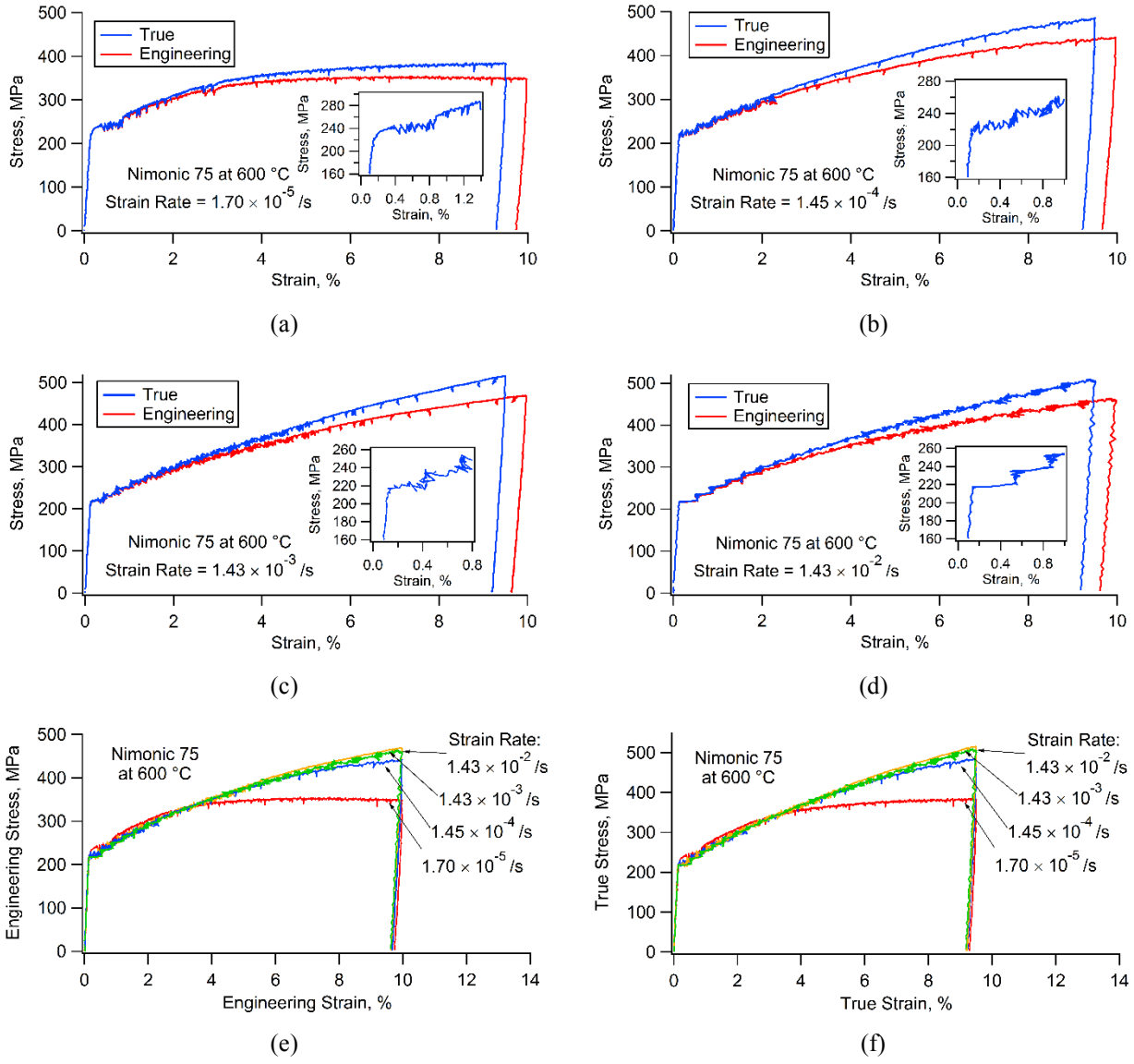

Figure 11. Stress-strain response of Nimonic 75 tested under monotonic tension at 600 ºC: (a) strain rate of 1.70×10^{-5} /s; (b) strain rate of 1.45×10^{-4} /s; (c) strain rate of 1.43×10^{-3} /s; (d) strain rate of 1.43×10^{-2} /s; (e) engineering stress-engineering strain responses for all four strain rates in one plot; (f) true stress-true strain responses for all four strain rates in one plot.

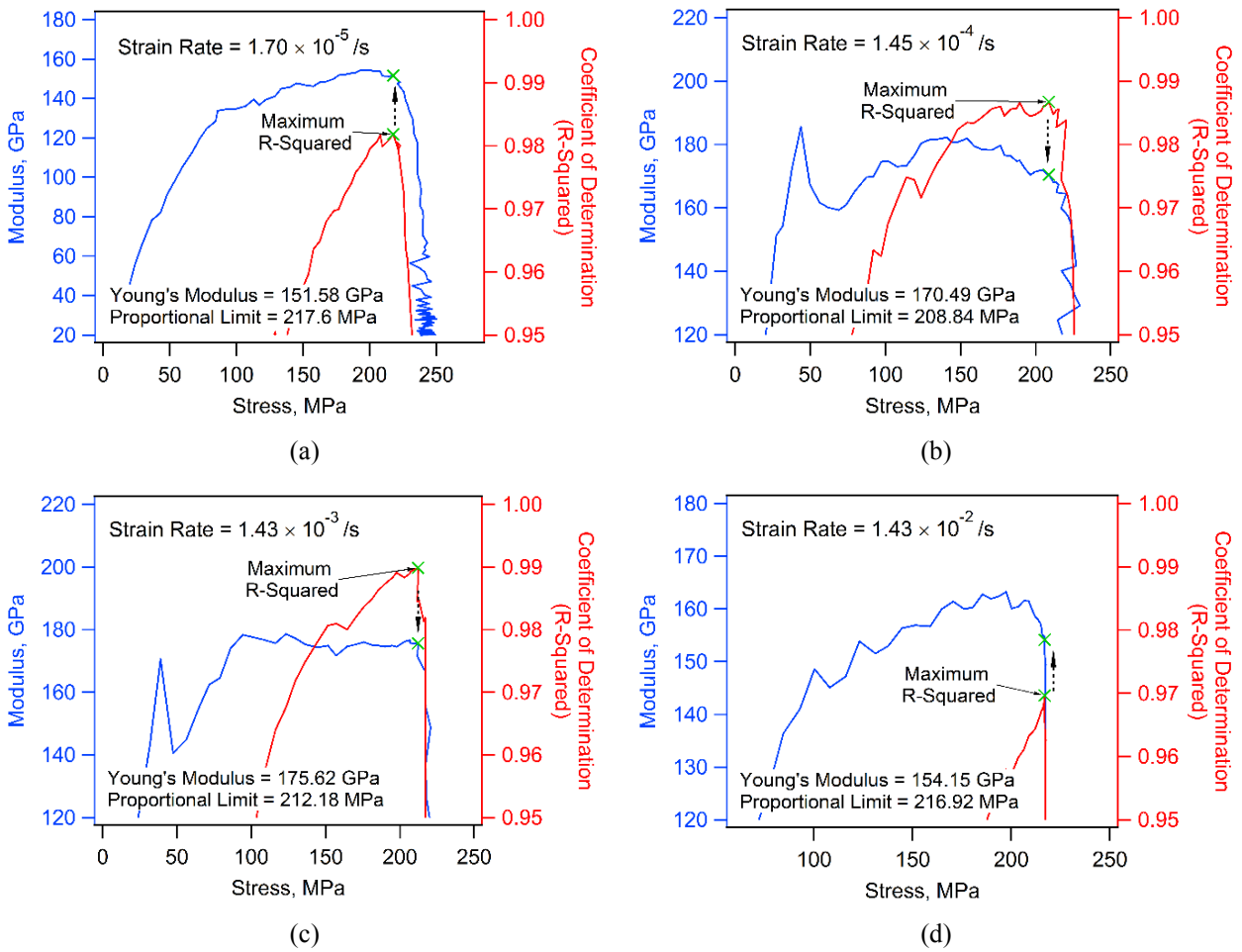

Figure 12. Young's modulus and proportional limit determined by finding the maximum value of the coefficient of determination (R^2) as a function of the "high-bound" stress level in the fitting section: (a) strain rate of 1.70×10^{-5} /s; (b) strain rate of 1.45×10^{-4} /s; (c) strain rate of 1.43×10^{-3} /s; (d) strain rate of 1.43×10^{-2} /s.

Table 2. Polycrystalline Young's modulus, proportional limit, and single-crystal CRSS for Nimonic 75 subjected to monotonic tension at 600 °C.

Strain Rate (/s)	Young's Modulus (GPa)	Proportional Limit (MPa)	Single-Crystal CRSS (MPa)
1.70×10^{-5}	151.58	217.60	24.07
1.45×10^{-4}	170.49	208.84	23.10
1.43×10^{-3}	175.62	212.18	23.47
1.43×10^{-2}	154.15	216.92	23.40

In (Akhtar and Teghtsoo, 1971), the critical resolved shear stress (CRSS) for single-crystal Ni-Cr alloys with different compositions was measured as a function of increasing temperature (up to 620 K). It was concluded that for all Ni-Cr compositions, CRSS decreases with increasing temperature. Above 500 K, the CRSS becomes nearly independent of temperature. The trend of CRSS versus the temperature is seen in Figure 13a. In Figure 13, the CRSS at 0 K is denoted as τ_0. The CRSS above 500 K is referred to as the plateau stress τ_p. Figure 13b shows how we deduced the CRSS for single-crystal Ni-20Cr alloy to be 36.8 MPa and 23.1 MPa at room temperature (strain rate = 1.66×10^{-4}) and 600 ºK (873 ºK) (strain rate = 1.45×10^{-4}), respectively, by interpolating the data for the various Ni-Cr compositions.

CRSS is thought to be dependent on strain rate. To estimate the single-crystal CRSS at various strain rates, we propose a way to assess the strain-rate sensitivity of single-crystal CRSS via the strain-rate sensitivity of the polycrystal proportional limit. We assume a structural relationship exists between single crystal CRSS $(\tau_{CRSS})_{Single}$ and polycrystal proportional limit $(\sigma_P)_{Poly}$

$$(\sigma_P)_{Poly} = M \times F \times (\tau_{CRSS})_{Single} \qquad \text{Equation 4}$$

where M is the Taylor factor and is known to be 3.06 for FCC material having random texture. F denotes the strengthening factor that accounts for the grain-size hardening effect (Hall–Petch relation) and precipitation hardening effect. As the CRSS (23.1 MPa) for Ni-Cr alloy was measured at a strain rate of 1.66×10^{-4} /s in (Akhtar and Teghtsoo, 1971), the structural factor can be estimated by the polycrystalline proportional limit $(\sigma_P)_{Poly}$ (208.84 MPa) measured at 1.45×10^{-4} /s in our monotonic tension experiment. Thus, the value of $M \times F$ can be estimated to be 9.04. Consequently, an estimation of single-crystal CRSS can be acquired by applying the structural relationship (Equation 4) on the polycrystalline proportional limit, which is summarized in Table 2 and Figure 14b.

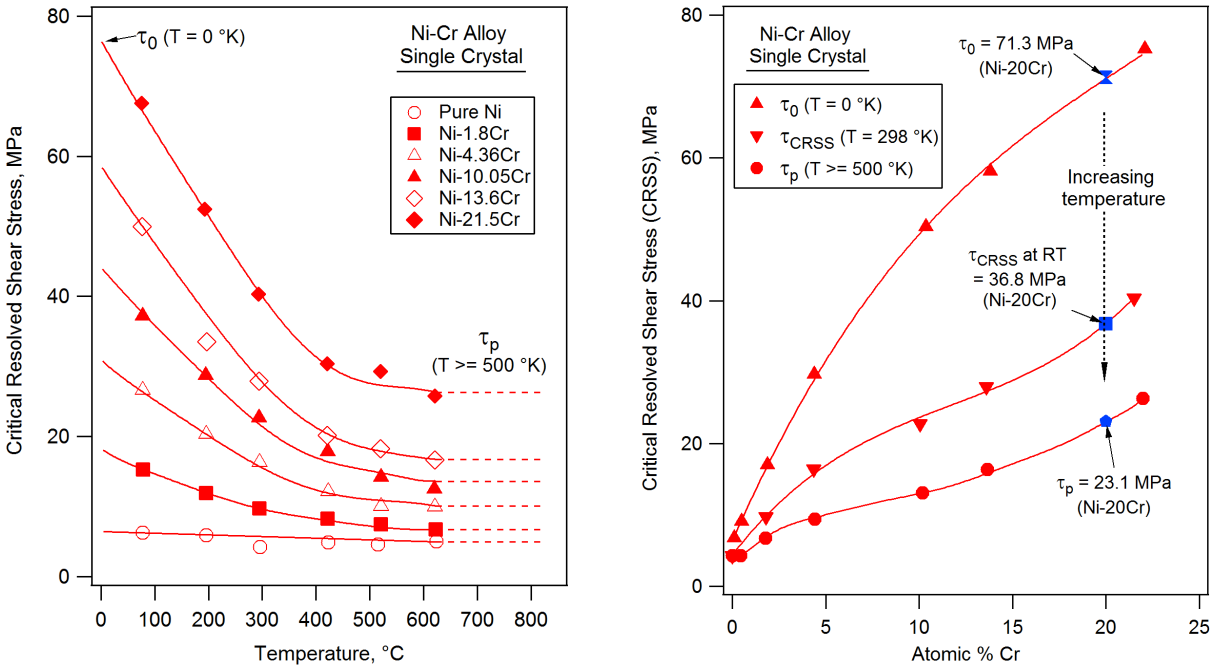

(a) (b)

Figure 13. Comparison of Young's modulus and proportional limit at RT and 600 °C with those in literature: (a) Young's modulus; (b) proportional limit.

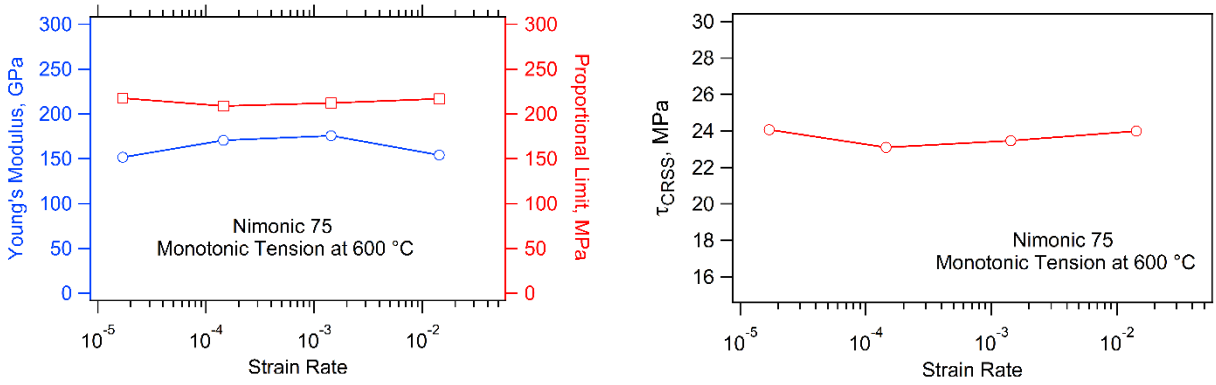

(a) (b)

Figure 14. Strain rate effects on the polycrystalline Young's modulus and proportional limit (a), and the estimated single-crystal critical shear resolved stress (CRSS) (b) for Nimonic 75 subjected to monotonic tension at 600 ºC.

2.1.6.4. Features of Visco-Plastic Behavior, Work Hardening and Dynamic Recovery

Figure 15a presents the true stress-true plastic strain curves for all the four strain rates. The plastic strain is calculated by subtracting the elastic part from the total strain. A detailed examination of the stress-plastic strain curves for all four strain rates reveals that the entire

plastic deformation (up to total strain of 10 %) of the material consists of two stages: Stage I–a plastic flow plateau following immediately the initial yielding, and Stage II-a power-law plastic flow with strain hardening rate being gradually decreased. A schematic of this two-stage plastic flow is illustrated in Figure 15b.

To capture the feature of Stage-I plastic plateau, two parameters are identified: plateau stress ($\sigma_{Plateau}$) and plateau strain range ($\Delta\varepsilon_{Plateau}$). The plateau stress ($\sigma_{Plateau}$) sets the stress level of the perfectly plastic flow. The plateau strain range ($\Delta\varepsilon_{Plateau}$) indicates the plastic strain range during which the plastic plateau occurs and can serve as an indication of the starting of the Stage-II plastic deformation. The strain-rate dependence of $\sigma_{Plateau}$ and $\Delta\varepsilon_{Plateau}$ is summarized in Table 3 and Figure 16. It is visualized that as the strain rate is increased, the plateau stress decreases. A similar trend exists for the plateau strain range up to the strain rate of 1.43×10^{-3} /s.

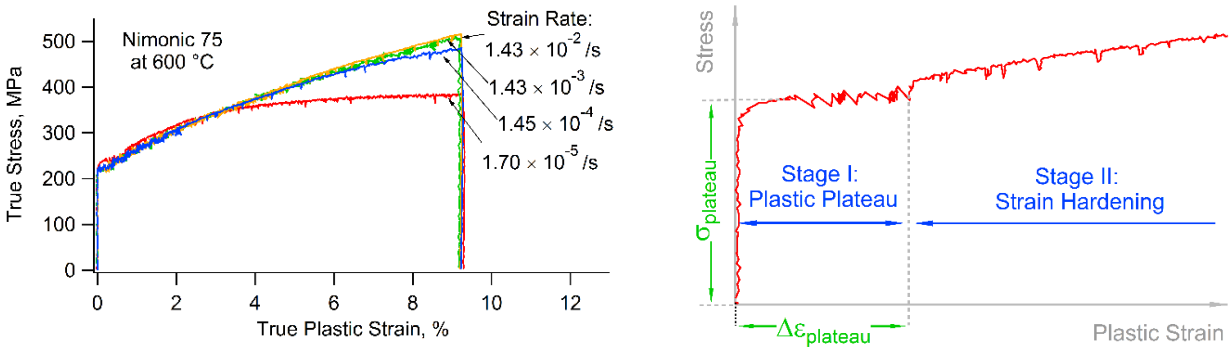

Figure 15. (a) True stress-true plastic strain curves for Nimonic 75 tested under monotonic tension at 600 ºC; (b) schematic of two-stage visco-plastic behavior.

Table 3. The plateau stress ($\sigma_{Plateau}$) and plateau strain range ($\Delta\varepsilon_{Plateau}$) during Stage-I plastic plateau for Nimonic 75 subjected to monotonic tension at 600 °C.

Strain Rate (/s)	Plateau Stress, $\sigma_{Plateau}$ (MPa)	Plateau Strain Range, $\Delta\varepsilon_{Plateau}$ (%)
1.70×10^{-5}	245.00	0.687
1.45×10^{-4}	225.26	0.397
1.43×10^{-3}	220.00	0.308
1.43×10^{-2}	218.57	0.399

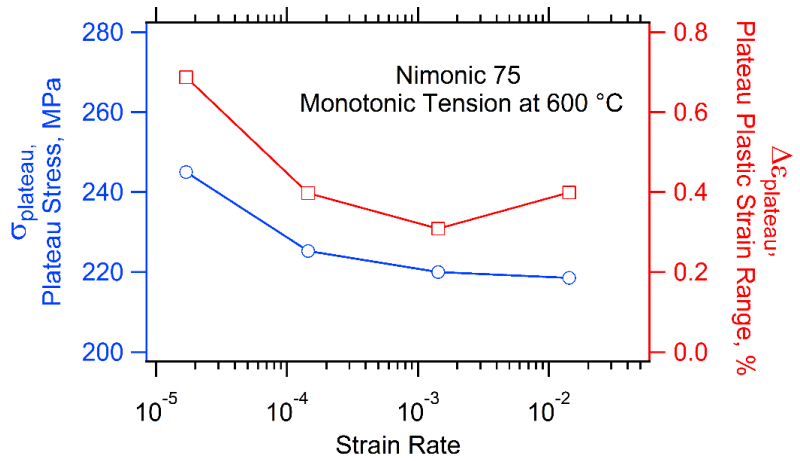

Figure 16. Strain rate effects on plateau stress ($\sigma_{Plateau}$) and plateau strain range ($\Delta\varepsilon_{Plateau}$) during the Stage I plastic plateau.

Figure 15a shows that a power-law relation exists between the stress and plastic strain during Stage-II plastic deformation. The description using Ramberg–Osgood relationship (Ramberg and Osgood, 1943) seems simple and straightforward. However, the Ramberg–Osgood relationship is purely phenomenological and does not reflect any physical mechanism. Fundamentally, the plastic flow is accommodated by dislocation slip. During plastic deformation, multiplication and accumulation of dislocations can lead to strain hardening. Particularly for hot deformation, the net increase of dislocation is essentially contributed by two competitive processes: dislocation accumulation and dislocation annihilation, which reflect the strain hardening effect and the dynamic recovery effect, respectively. Therefore, to appropriately account for the physics behind Stage-II plastic deformation, a model that inherently quantifies the evolution of dislocations, such as the Kocks-Mecking constitutive equation (Kocks and Mecking, 2003), is more promising.

2.1.7. *Strain Rate Effects on the Serration Plastic Flow of Nimonic 75 at 600 ºC*

Analysis on the serrated plastic flow for Nimonic 75 based on the experimental tensile data is presented here. This is important since the stick-slip behavior of serrated flow can be captured and simulated with the DEM model; indeed, serrations often emerge from our model formulation. Figure 17a displays the true stress-true strain curves for Nimonic 75 alloy subjected to monotonic tension at 600 °C at strain rates from 1.70×10^{-5} s^{-1} to 1.43×10^{-2} s^{-1}. For better data visualization, the stress-strain curves are shifted along the strain axis. A glance at the stress-strain curves shows serrated flow appears at all the investigated strain rates. Different serration types are summarized in a serration map as a function of strain rate and strain (Figure 17b). A general trend of early-stage serration type changing from Type A+B to Type C can be readily visualized from Figure 17b. This trend is consistent with the documented Portevin-Le Chatelier (PLC) effect for various solid solution alloys (Rodriguez, 1984; Yilmaz, 2011; Zhang et al., 2017). A detailed identification of serration types for different strain rates will be described in the following.

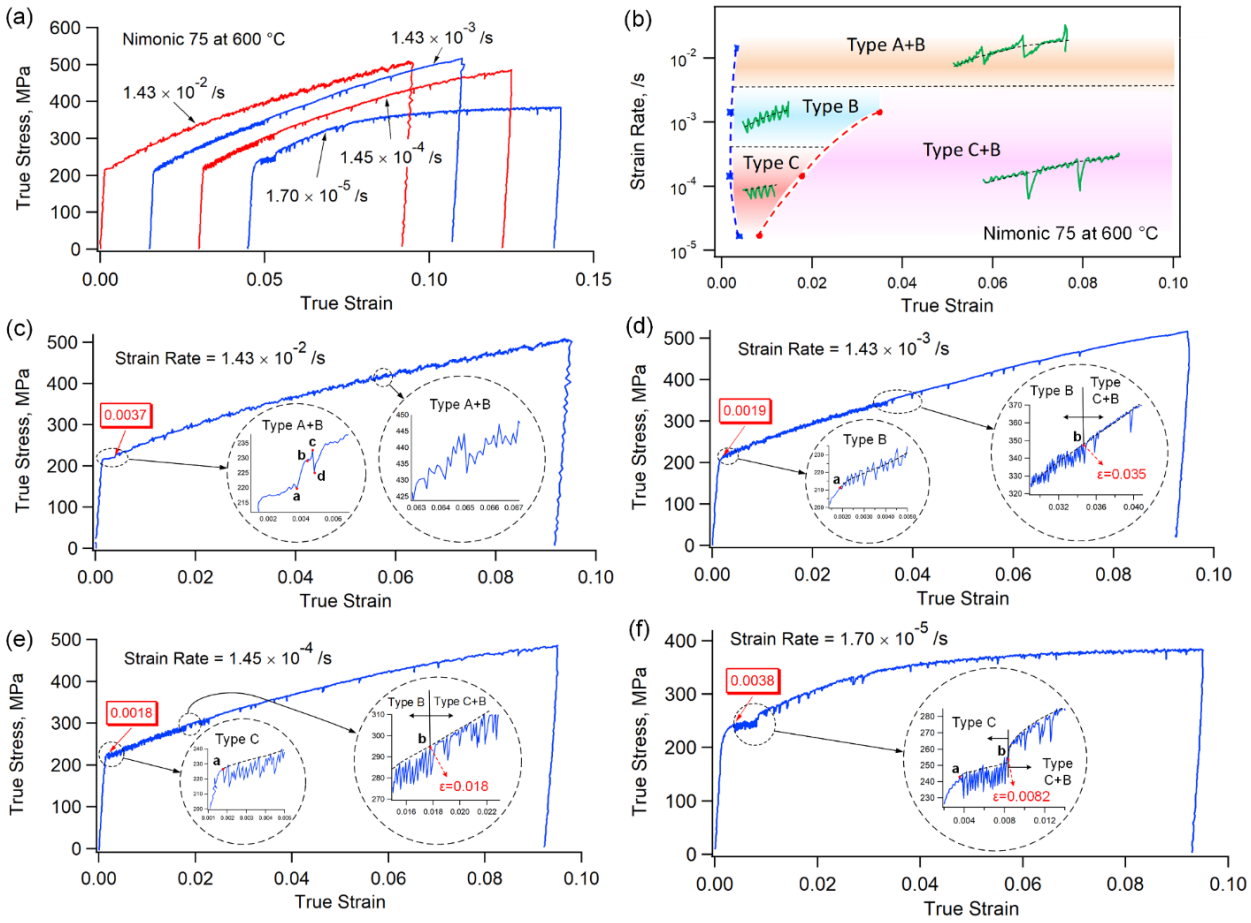

Figure 17. (a) True stress-true strain curves for Nimonic 75 alloy subjected to constant-strain-rate tension at 600 °C; (b) schematic map showing variation of serration type with respect to the strain rate and strain; (c)-(f) identified serration types at strain rates of 1.43×10^{-2} s^{-1}, 1.43×10^{-3} s^{-1}, 1.45×10^{-4} s^{-1}, and 1.70×10^{-5} s^{-1}, respectively.

At a high strain rate of 1.43×10^{-2} s^{-1} (Figure 17c), the material macroscopically yielded at a point with a strain of 0.0015 and a stress of 215.7 MPa. Afterwards, stable plastic flow with low strain-hardening rate ($\Delta\sigma/\Delta\varepsilon \approx 1477.1$ MPa) occured until an abrupt stress rise was detected at a strain of 0.0037 (point a in Figure 17c). The stress rise was composed of two stages. During the first stage, the stress increased rapidly ($\Delta\sigma \approx 9.4$ MPa) until a yielding point b was reached. A second stress increment ($\Delta\sigma \approx 3.1$ MPa) was followed until a peak stress (point c in Figure 17c) was reached. It is noted that although the second-stage stress rise is smaller than that in the first stage, the strain hardening rate in the second stage is much higher, comparing $\Delta\sigma/\Delta\varepsilon \approx 17075.2$ MPa for the first stage and $\Delta\sigma/\Delta\varepsilon \approx 20241.5$ MPa for the second stage. The two-stage stress rise reflects the aging effect caused by solute clusters diffusing to mobile dislocations. This solute aging effect reached to a maximum degree at the peak point c (Figure 17c), where dislocation was pinned in the solute cloud. Right after the peak stress, the stress dropped extremely rapidly, bringing the stress back to slightly above the general level of the stress-strain curve. The stress drop is believed to be associated with the release of the pinned dislocation. The amount of stress drop might be used to indicate the accumulated obstacle effect to the moving dislocation arisen from the forest dislocation and the solute cloud. The previous observed stress rise and stress drop behavior describes a typical Type A serration. The reason why we designate Type A+B to this

serration event in Figure 17c is based on the fact that small oscillation of stress was observed prior to, during, and after the stages of stress rise and stress drop even at the very beginning of the serrated plastic flow. Such a secondary Type-B stress oscillation accompanying the primary Type-A serration becomes more obvious with more accumulation of strain (Figure 17c).

When the strain rate is controlled at a lower value of 1.43×10^{-3} s^{-1}, serrated flow was detected by the stress drop at a strain of 0.0019 (point a in Figure 17d). A stress rise followed immediately after the stress drop. The strain hardening rates of the stress drop and the stress drop were of the same order. Sequences of stress drop and stress rise followed successively, appearing to oscillate about the general level of the stress-strain curve. This is a typical Type-B serration behavior. We found that such a Type-B serration terminated at a strain of 0.035 (point b in Figure 17d), where the stress-strain curve exhibited an abrupt stress drop followed by a gradual stress rise turning the stress back to the general level. According to the documented serration shapes, the serration changed from Type B to Type C at point b. It is noted that Type C serration did not occur continually. Instead, there is a strain interval between two sequential counts of Type-C "tooth," in which one stress drop and one stress rise are included. What's more, stress oscillation in small magnitude was present in the stress-strain curve between two sequential Type-C "teeth." Therefore, we identify the serrated flow after point b to be of Type C+B.

At a low strain rate of 1.45×10^{-4} s^{-1}, serrated flow started with a detection of stress drop at 0.0018 strain (point a in Figure 17e). The following stress rise brought the stress back to the general level stress-strain curve. Subsequent stress drop and stress rise follow the same fashion and occur continuously. Therefore, a typical Type C serration was identified after the onset of the serrated flow at this strain rate. At a strain of 0.018 (point b in Figure 17e), the continuous Type C serration, where one Type-C "tooth" is followed by the other, breaks. Instead, a Type C+B serration behavior similar to the later stage of serrated flow at the strain rate of 1.43×10^{-4} s^{-1} was observed. The general trend of the serration-type changing from Type C to Type C+B was identified for the strain rate at 1.70×10^{-5} s^{-1} as well. But there exist two importance features for the strain rate of 1.70×10^{-5} s^{-1}, making it different from the case at strain rate of 1.45×10^{-4} s^{-1}. First, the general locus of the stress-strain curve in the initial Type C serration stage shows a near-zero strain hardening rate. This mechanical response is very similar to the yield plateau caused by Lüder's band propagation often observed in mild steel. However, in annealed mild steel, a typical inhomogeneous plastic deformation always starts with an upper yield stress signifying the termination of the elastic deformation, and proceeds at a decreased stress level known as the lower yield stress. In the current case (Figure 17f), there is no upper yield stress for the onset of inhomogeneous deformation. In addition, all the stress jumps and drops are below the general locus of the stress-strain curve (Figure 17f). Second, at the transition strain where serration changed from Type C to Type C+B, the strain hardening rate of the general stress-strain locus increased abruptly and gradually decreased with the increasing strain. This is different from the strain rate at 1.45×10^{-4} s^{-1}, where a continuity of strain hardening exists at the transition strain from Type C serration to Type C+B serration (see Figure 17e).

As consequence of the interactions between mobile dislocations and solute atoms, mobile dislocations can become pinned by the solute atmosphere when sufficient solute concentration is reached. Macroscopically, the pinning event is detected when a peak stress is reached during the stress rise segment. With the aid of additional applied stress, the pinned dislocations can overcome the barrier energy and move freely, resulting in a rapid stress drop. Therefore, we consider the *stress drop* as the most important macroscopic parameter that is directly correlated

to the dynamic strain aging effect caused by the interaction between mobile dislocations and diffusing solutes. In this regard, we extract the stress drop $\Delta\sigma_{drop}$ from the serrated flow and investigate its variance with respect to increasing strain in different types of serrated flow in our material.

Stress drop $\Delta\sigma_{drop}$ is defined as the difference between the local maximum stress (peak stress) and its successive local minimum stress. For a Type A+B or Type C+B serration where a mixing of Type B serration is present, a primary $\Delta\sigma_{drop}$ (for Type A or C) is distinguished from a secondary $\Delta\sigma_{drop}$, which is lower in magnitude and represents the stress drop associated with the mixed Type B serration. The definitions are schematically illustrated in Figure 18a. The variations of stress drop with respect to the increasing strain at various strain rates are summarized in Figure 18b-Figure 18e. As the original $\Delta\sigma_{drop}$ data (see the marks in Figure 18b-Figure 18e) are scattered within certain ranges, we smooth the data into trend lines (see the solid lines in Figure 18b-Figure 18e) using the moving average algorithm.

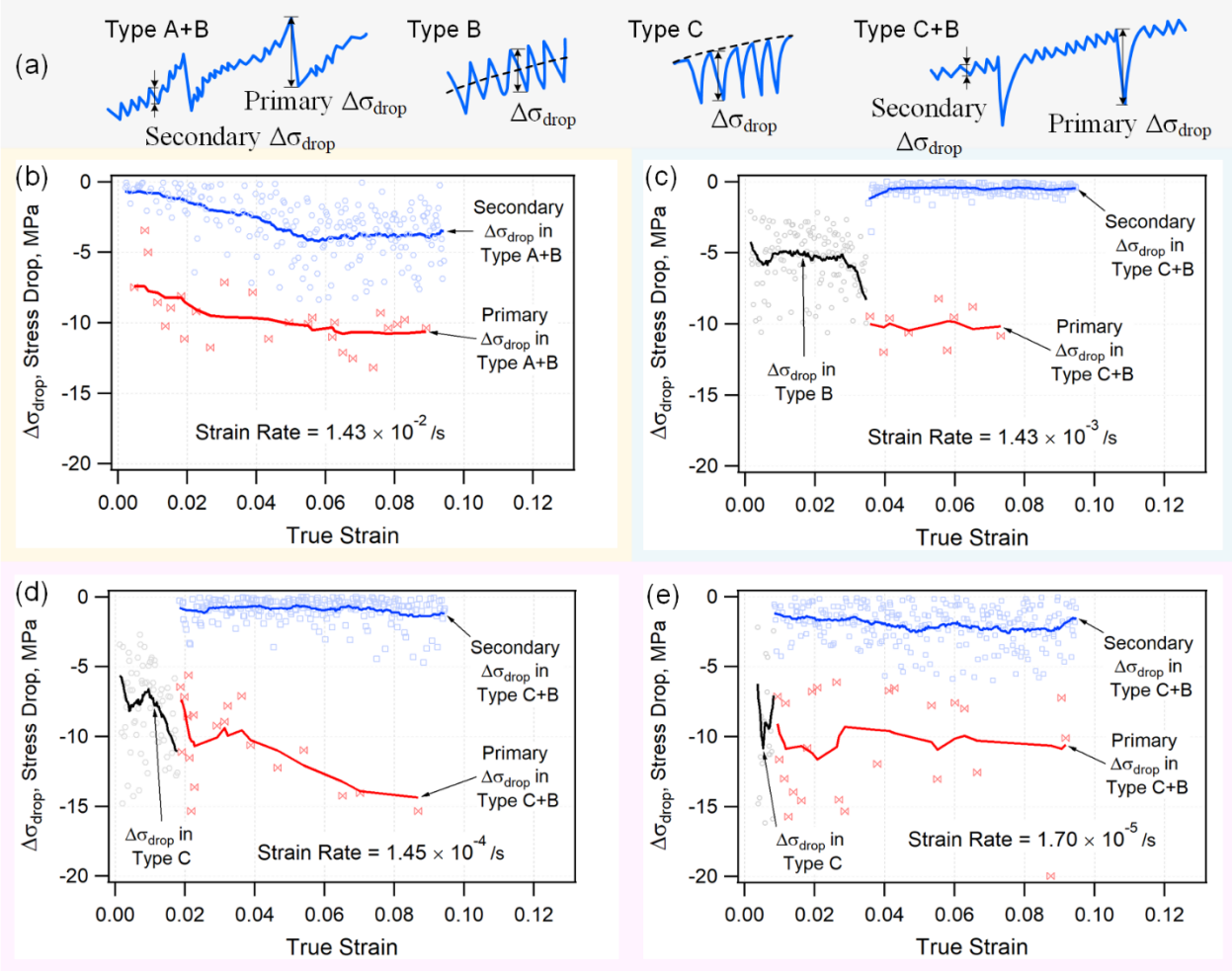

Figure 18. Variations of stress drop with respect to the increasing strain at various strain rates: (a) schematics illustrating the definitions of stress drops in different types of serrations; (b)-(e) stress drops at strain rates of 1.43×10^{-2} s^{-1}, 1.43×10^{-3} s^{-1}, 1.45×10^{-4} s^{-1}, and 1.70×10^{-5} s^{-1}, respectively.

For the high strain rate of 1.43×10^{-2} s^{-1} (Figure 18b), the primary Type A $\Delta\sigma_{drop}$ increases continuously from ~6 MPa at the onset of serration to a saturation value of ~11 MPa at the strain of 0.06. Likewise, such a trend is exhibited in the secondary Type B $\Delta\sigma_{drop}$, where it initially increases from a small magnitude of 0.5 MPa and approaches to saturation (~4 MPa) at 0.06 strain. For the higher strain rate of 1.43×10^{-3} s^{-1} where Type B followed by Type C+B serration is exhibited, the Type B $\Delta\sigma_{drop}$ increases slowly from a magnitude of 4 MPa to a strain of 0.03%, at which a rapid increase of $\Delta\sigma_{drop}$ was continued until it reaches ~9 MPa at a transition strain of 0.035. In the subsequent Type C+B serration flow, both the primary and secondary $\Delta\sigma_{drop}$ stay almost unchanged at 10 MPa and 0.5 MPa, respectively. For the two lower strain rates of 1.45×10^{-4} s^{-1} and 1.70×10^{-5} s^{-1} (Type C serration followed by Type C+B), some common observations are obtained: (1) the $\Delta\sigma_{drop}$ is continuous at the transition strain at which serration type changes from Type C to Type C+B the early-stage; (2) secondary $\Delta\sigma_{drop}$ in the Type C+B serration is insensitive to the strain and remain in small magnitudes 1~2 MPa in average. However, there exists an important difference between these two strain rates. At the strain rate of 1.45×10^{-4} s^{-1}, the Type C $\Delta\sigma_{drop}$ increases monotonically from ~6 MPa to ~15 MPa in the entire strain range. However, at the strain rate of 1.70×10^{-5} s^{-1}, $\Delta\sigma_{drop}$ oscillates between 6 MPa and 10 MPa in the Type C stage. When the serrated flow enters the Type C+B stage, the primary $\Delta\sigma_{drop}$ only exhibits a very small increasing from 9 MPa to 10.5 MPa. It is noticed that such an increasing trend is visualized from the average trend line. Actually, the scattering of the primary $\Delta\sigma_{drop}$ during this stage is much higher than that shown in the strain rate of 1.45×10^{-4} s^{-1}.

As described above, the $\Delta\sigma_{drop}$ in Type B and Type C serrations (except for the slowest strain rate of 1.70×10^{-5} s^{-1}) shows a general positive correlation to the increasing strain. The same trend applies for the primary $\Delta\sigma_{drop}$ in Type A+B and Type C+B serrations. This common observation signifies that the collective pinning strength (or the aging effect) exerted to the mobile dislocations by the solute cloud and the obstacle defects (majorly immobile forest dislocations in our alloy) becomes aggregated. This is likely attributed to the fact that the immobile dislocations are multiplied as the material undergoes plastic deformation. Another reason could be related to the strain-induced vacancy concentration (Militzer et al., 1994). Vacancies can be generated and segregate at dislocations and grain boundaries by movement of dislocation jogs during high temperature deformation. Because vacancies in the vicinity of dislocations are sinks of diffusion solute atoms, it is reasonable to derive that the increased plastic strain will lead to an increasing solute aging effect. Applying the suggested mechanism above, it is also reasonable to explain the oscillation of $\Delta\sigma_{drop}$ in the Type C stage at the slowest strain rate of 1.70×10^{-5} s^{-1}. We know that the upper bound of the Type C serrated stress-strain response forms a yielding plateau, which bears almost zero strain hardening (Figure 17f). The absence of a macroscopic strain hardening in this stress-strain segment suggests that the accumulation of immobile dislocations is minimal. Therefore, the pinning effect resulted from the interaction between obstacle and the solute atoms is unchanged.

2.1.8. *Fracture Stress, Fracture Strain and Fracture Behavior of Nimonic 75 at 600 º*

In order to capture the fracture behavior in the DEM model, the fracture stress and fracture strain of Nimonic 75 subjected to tension at 600 ºC was determined. We carried out tension experiments with two strain rates (1.43×10^{-2} s^{-1} and 1.43×10^{-3} s^{-1}) without using an

extensometer. We use the strain-position relationship obtained in the previous 10%-tension experiment to extrapolate the strain beyond 10% using the position data recorded in our current experiment. In this way, we can have the full range of stress-strain response up to fracture (Figure 19a). We repeated each strain rate with three specimens. The fracture stress and fracture strain together with the reduction of area measured from final fracture profile are summarized in Table 1 and Figure 19b. The experimental result turns out that fracture stress and fracture strain are independent of the two investigated strain rates. However, larger reduction of area is found as the strain rate is increased.

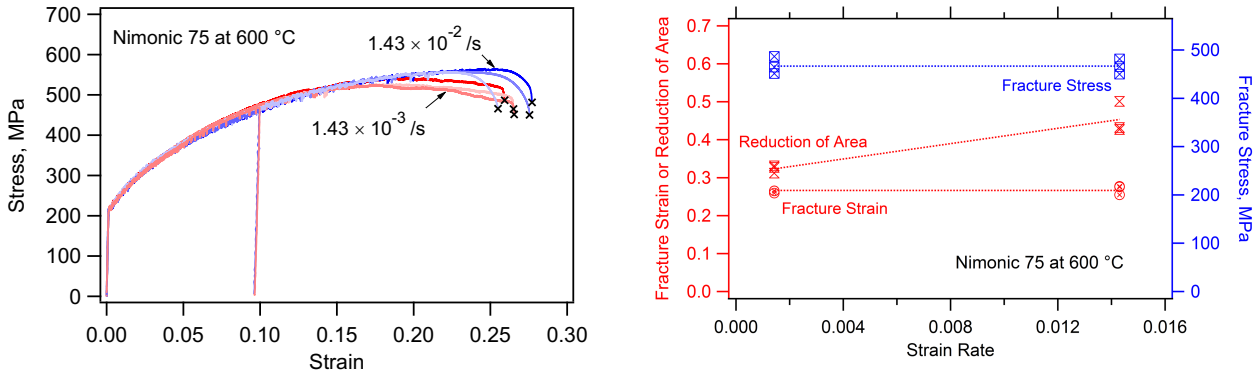

Figure 19. (a) Stress-strain response up to fracture; (b) fracture stress, fracture strain, and reduction of area.

Table 4. Fracture stress, fracture strain, and reduction of area for Nimonic 75 subjected to tension at 600 ºC under strain rates of 1.43×10^{-2} $s^{-1}$and 1.43×10^{-3} s^{-1}.

Strain Rate, s^{-1}	Fracture Stress, MPa	Fracture Strain	Reduction of Area
0.0143	465.79	0.25496	0.501
0.0143	481.54	0.27708	0.432
0.0143	450.23	0.27547	0.427
0.00143	486.68	0.25929	0.327
0.00143	464.8	0.26506	0.312
0.00143	451.49	0.26548	0.331

2.1.9. *Determination of Creep Properties*

Creep tests were conducted at National Energy Technology Laboratory (NETL). Figure 20a shows the creep specimens used in the creep tests. Creep testing was conducted by a ATS 2330-MM lever arm creep frame (Figure 20b). A dual extensometer system (Figure 20c), which is not directly attached to the specimen but is part of a "chassis" that hold the specimen and extensometers together as one, is used to measure the creep strain. Creep samples were heated by an ATS furnace (model 3210). Three thermocouples were directly attached to the specimen using twisted wires to monitor the temperature. The specimen was soaked for one hour before the constant load was applied. Constant load of 160 MPa was applied to three companion creep specimens at 600 ºC. Creep tests were interrupted at 200, 400, and 600 hours. The purpose of carrying out interrupting creep experiments is to characterize the long-term microstructural

evolution so that the correct creep mechanism can be understood and will be implemented into the DEM model.

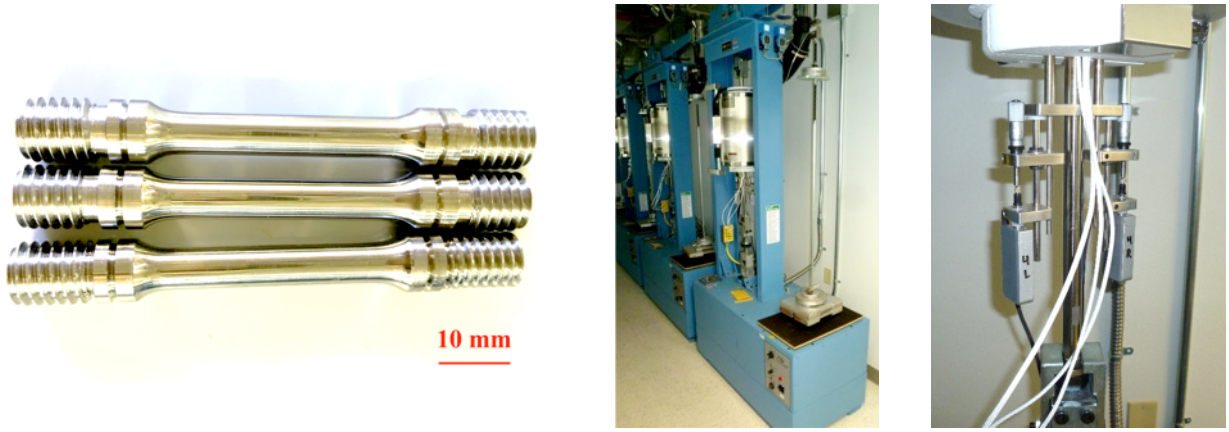

(a) (b) (c)

Figure 20. Creep specimen (a), creep frame (b), and dual extensometer system (c) used for the creep tests conducted at National Energy Technology Laboratory (NETL).

Figure 21a presents the creep curve for the 600-hour creep specimen. A comparison with the certificated results was also made (Gould and Loveday, 1990). The 600-hour specimen shows normal two-stage primary and steady-state creep deformation. The creep curve shows a sigmoidal transient creep stage during the initial ~150 hours, which is a typical creep feature for Nimonic 75 (Betteridge and Heslop, 1974). The creep rate at 400 hour, time to 2% creep strain, and time to 4% creep strain from NETL creep tests are compared to the certificated creep value (Gould and Loveday, 1990) as shown in Table 5. The creep rate at 400 hour stands in the range with two-time standard deviation (2S). However, the time to 2% creep strain and the time to 4% creep strain (extrapolated) stands out of the range with two-time standard deviation (2S). The reason is unclear and will need further investigation. The variance of creep rate at 400 hour with the applied stress is plotted in Figure 21b. The stress exponent n for the creep rate ($\dot{\varepsilon}_{400hr} = A\sigma^n$) can be evaluated to be 6.

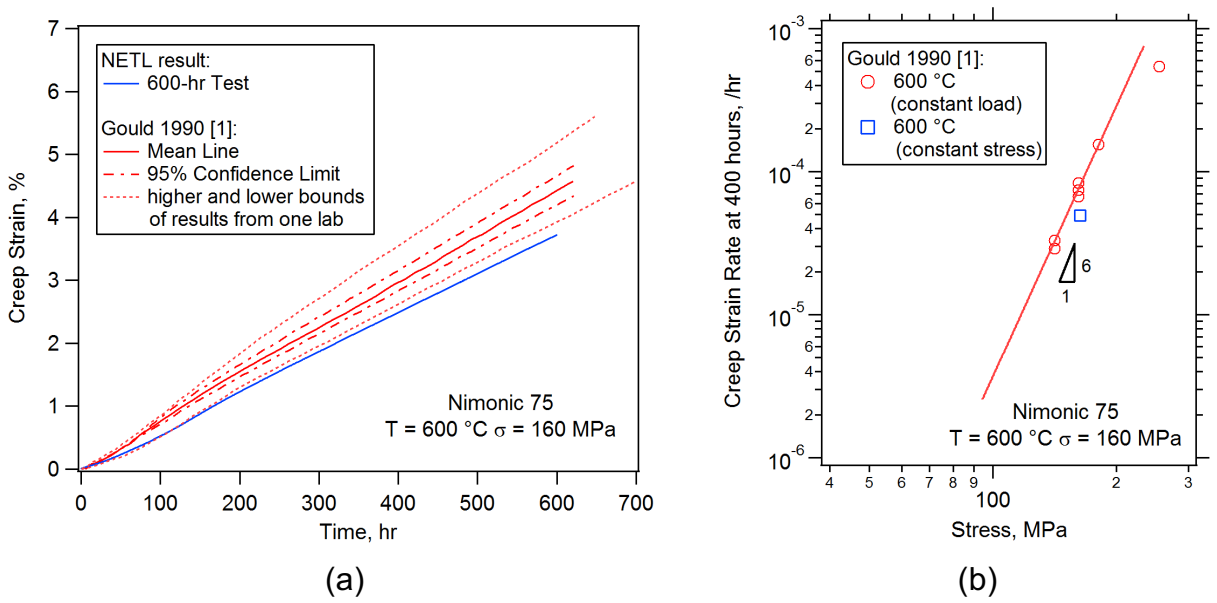

Figure 21. (a) Creep curve from NETL 600-hour creep test and a comparison to creep curves in Ref. (Gould and Loveday, 1990). (b) Variance of creep rate at 400 hour with the applied stress (Gould and Loveday, 1990).

Table 5. Comparison of the certificated creep properties (Gould and Loveday, 1990) with the result from NETL creep tests.

Creep Property	Certified Value (M)	Standard Deviation (S)	NETL Result
Creep rate at 400 hours	72×10^{-4} /hour	5×10^{-4} /hour	62×10^{-4} /hour
Time to 2% creep strain	278 hours	16 hours	320 hours
Time to 4% creep strain	558 hours	30 hours	640 hours (extrapolated)

2.1.10. *Microstructure Evaluation of Nimonic 75 During Creep Deformation*

In order to evaluate the microstructural evolution during creep deformation, three companion specimens were interrupted at 200, 400, and 600 hours, respectively. We have chosen two specimens that have experienced 200-hour and 600-hour creep deformation to assess the microstructure change (Figure 22). The creep strain and creep strain rate corresponding to the two creep deformation stages are listed in Table 6. The microstructure was characterized on the cross-section plane that is perpendicular to the loading direction (or extrusion direction, ED) by optical microscopy (OM), scanning electron microscopy (SEM), energy dispersive x-ray spectroscopy (EDS), electron backscatter diffraction (EBSD). The revealed creep microstructures were compared with the undeformed well-annealed microstructure (400 hours at 600 ºC).

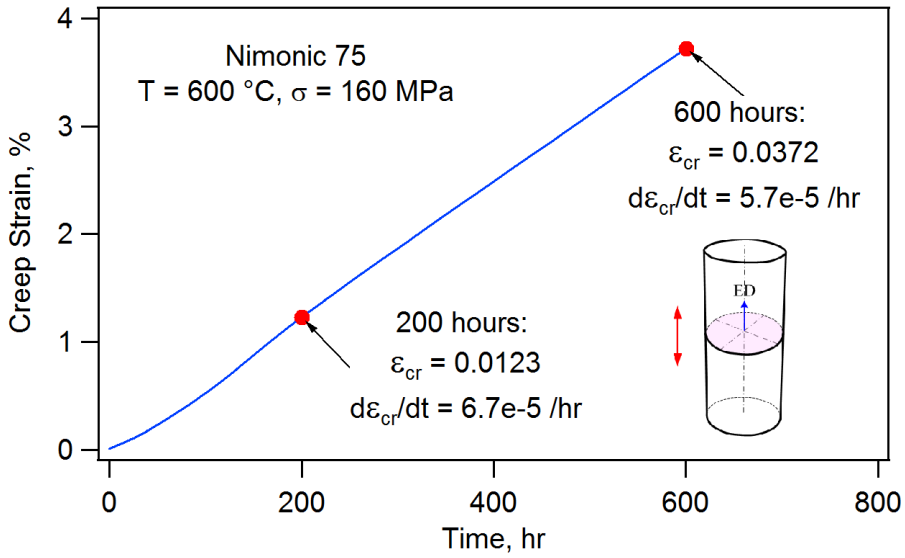

Fig. 1

Figure 22. Creep specimens used to evaluate evolution of creep microstructure.

Table 6. Creep strain and creep strain rate for the two creep samples for microstructure examination.

Specimen	Creep strain	Creep strain rate
200-hour creep sample	0.0123	6.7e-5 /hour
600-hour creep sample	0.0372	5.7e-5 /hour

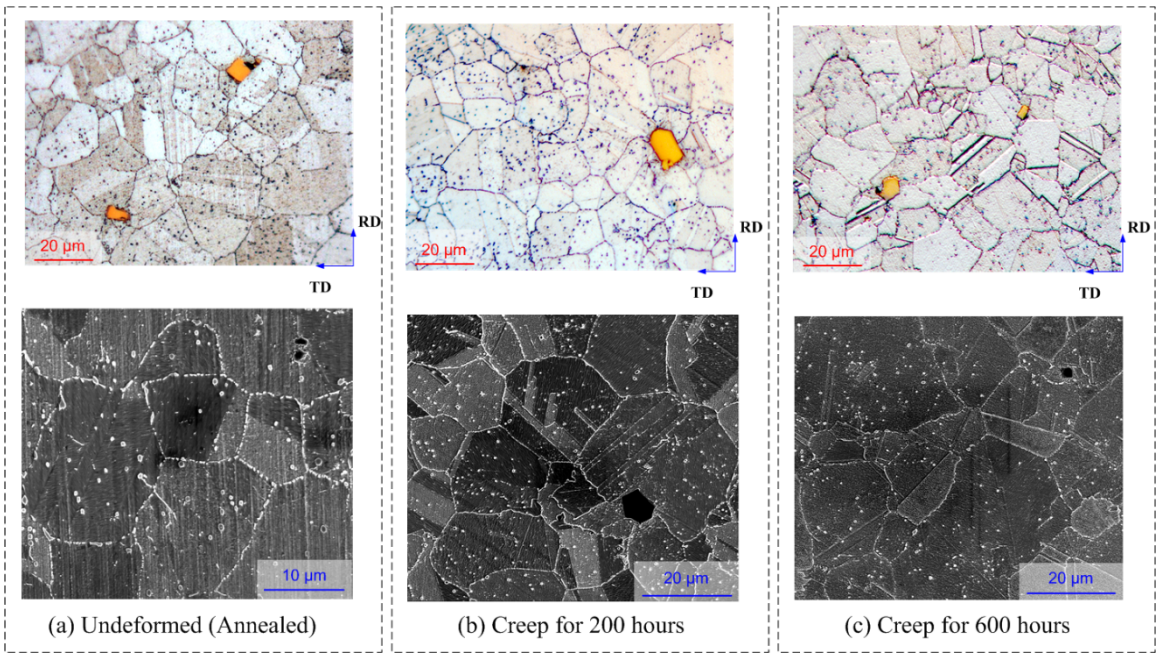

Figure 23. Optical and SEM microstructure of Nimonic 75 characterized on the cross section plane: (a) undeformed state (annealed at 600 °C for 400 hours); (b) creep deformation for 200 hours; (c) creep deformation for 600 hours.

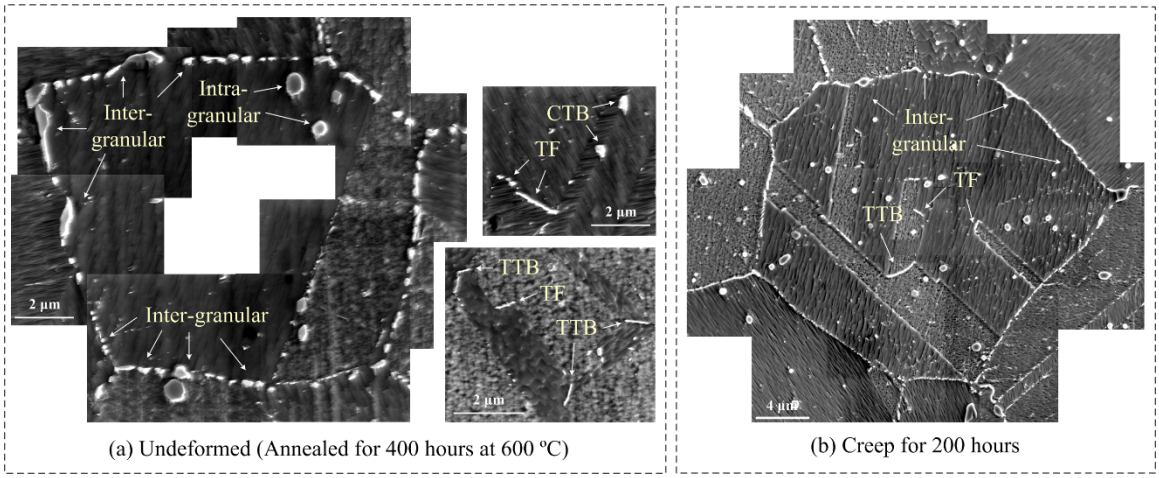

Figure 24. Magnified SEM observation of carbides in the vicinity of one grain before (a) and after (b) creep deformation for 200 hours.

Figure 23 shows the OM and SEM observation of the microstructure compared between the annealed and creep deformed states. It is found inter-granular carbides are increased after creep deformation. Figure 24 presents the magnified SEM micrographs captured in the vicinity of one grain for the undeformed and the 200-hour creep deformation states. As clearly revealed in Figure 24, the number of carbides is significantly increased at grain boundaries (GBs). In particular, the morphology of inter-granular carbides tends to appear more elongated and more continuous compared to the undeformed state. Such a dense distribution of elongated carbides can be found at twin-twin boundaries (TTBs) and twin fronts (TFs) as well. The increase in interfacial carbides coverage at GBs, TFs, and TTBs is suggested to be associated with the local accumulation of interfacial defects that are produced under the externally applied creep stress over the time.

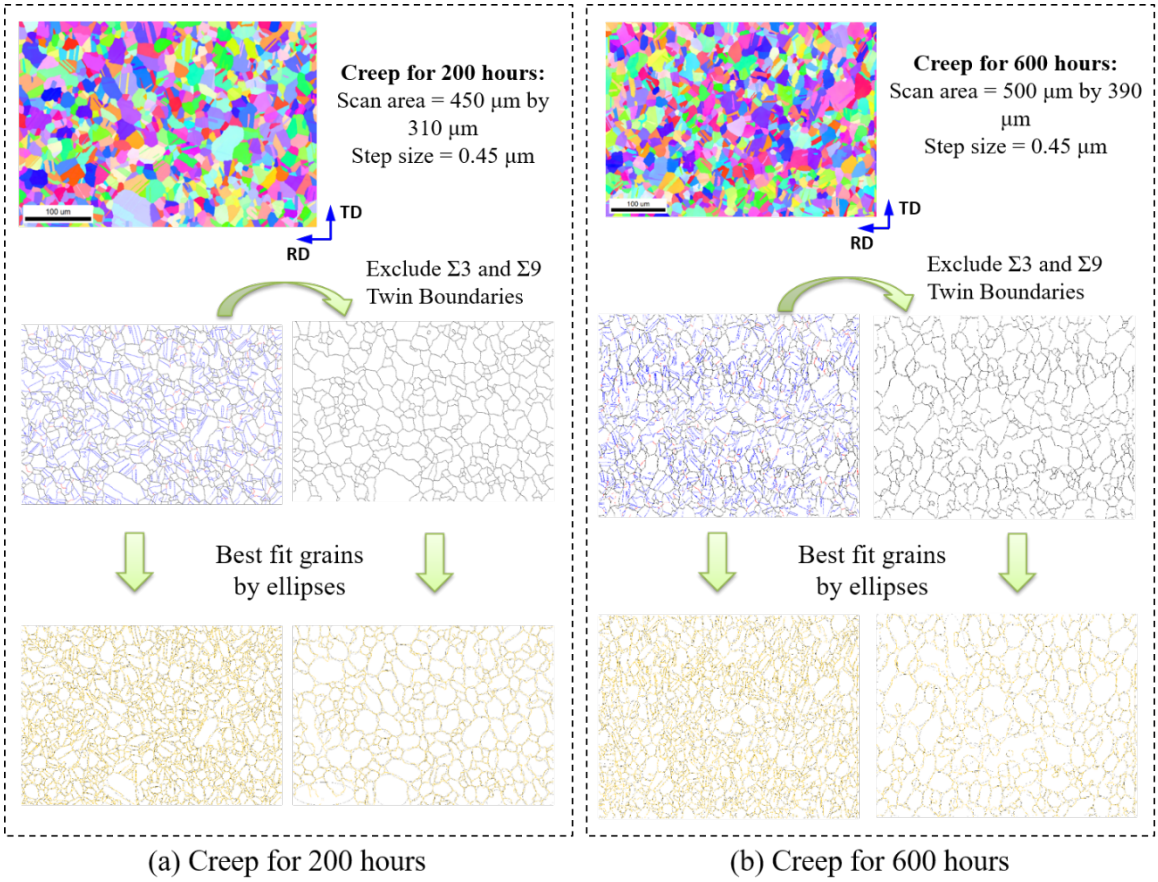

Figure 25. Crystal orientation map and grain boundary map (with and without twin boundaries) obtained by EBSD: (a) after 200-hour creep deformation; (b) after 600-hour creep deformation.

Quantification of the grain structure after creep deformation was obtained by EBSD mapping (Figure 25). Grain size & shape were evaluated with either including or excluding the Σ3 & Σ9 twin boundaries. Grains were best fitted by ellipses. Based on the best fitted ellipses, probability distributions of grain area, grain diameter, grain aspect ratio, and grain orientation were determined, as is shown in Figure 26. A comparison between the undeformed and creep deformed states shows trivial changes in grain morphology during creep deformation.

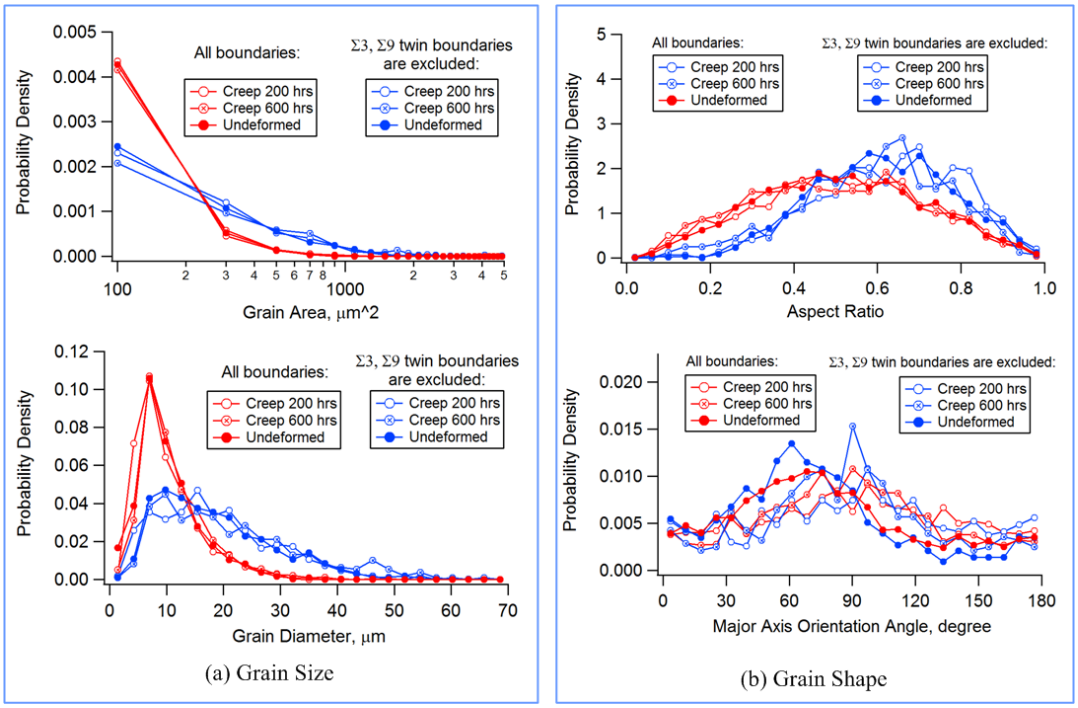

Figure 26. Comparison of probability density distribution of grain size and grain shape between the undeformed (annealed) and creep deformed (200 and 600 hours) states: (a) grain size in terms of area and diameter; (b) grain shape in terms of aspect ratio and major axis orientation.

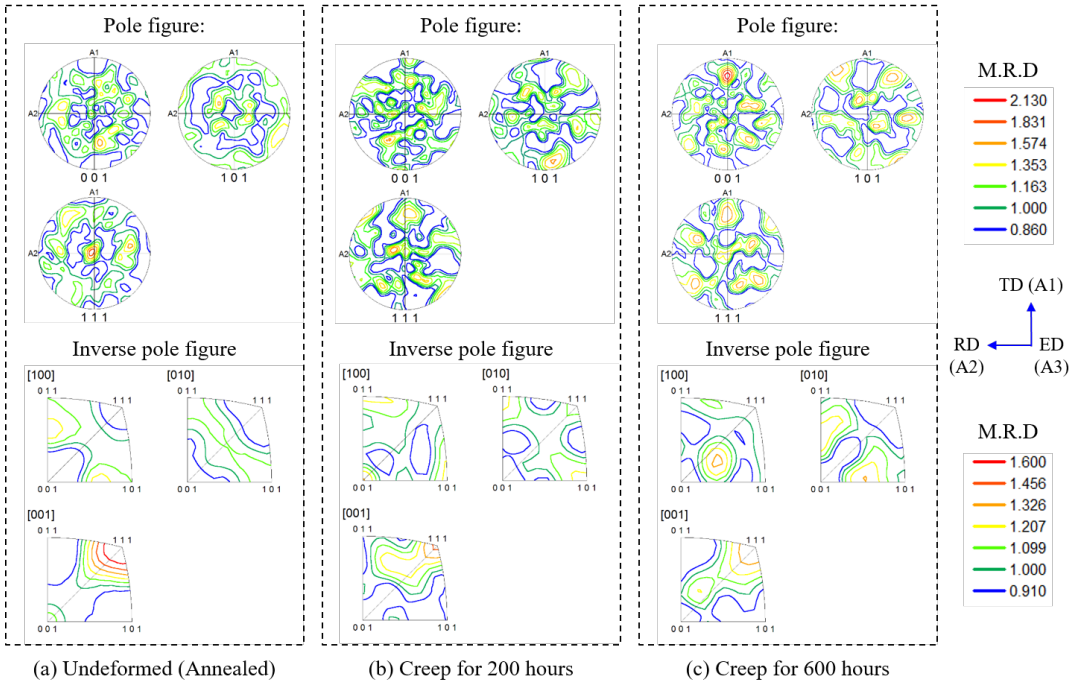

Figure 27. Evolution of grain orientation distribution: (a) undeformed state (annealed at 600 °C for 400 hours); (b) creep deformation for 200 hours; (c) creep deformation for 600 hours.

Evolution of grain orientation distribution is visualized in Figure 27 in terms of pole figures and inverse pole figures. From Figure 27, it is found that the direction of <1 1 1> poles that

converged mostly towards the tensile loading direction (or ED direction) in the undeformed state has a tendency of departure from loading direction. This indicates grain rotation occurs during creep deformation. Such grain rotation results in a weakening of axisymmetric <1 1 1> - <1 0 0> fiber texture that was originally exhibited at the undeformed state and acts as a "relaxation" process that leads to a more random distribution of grain orientations.

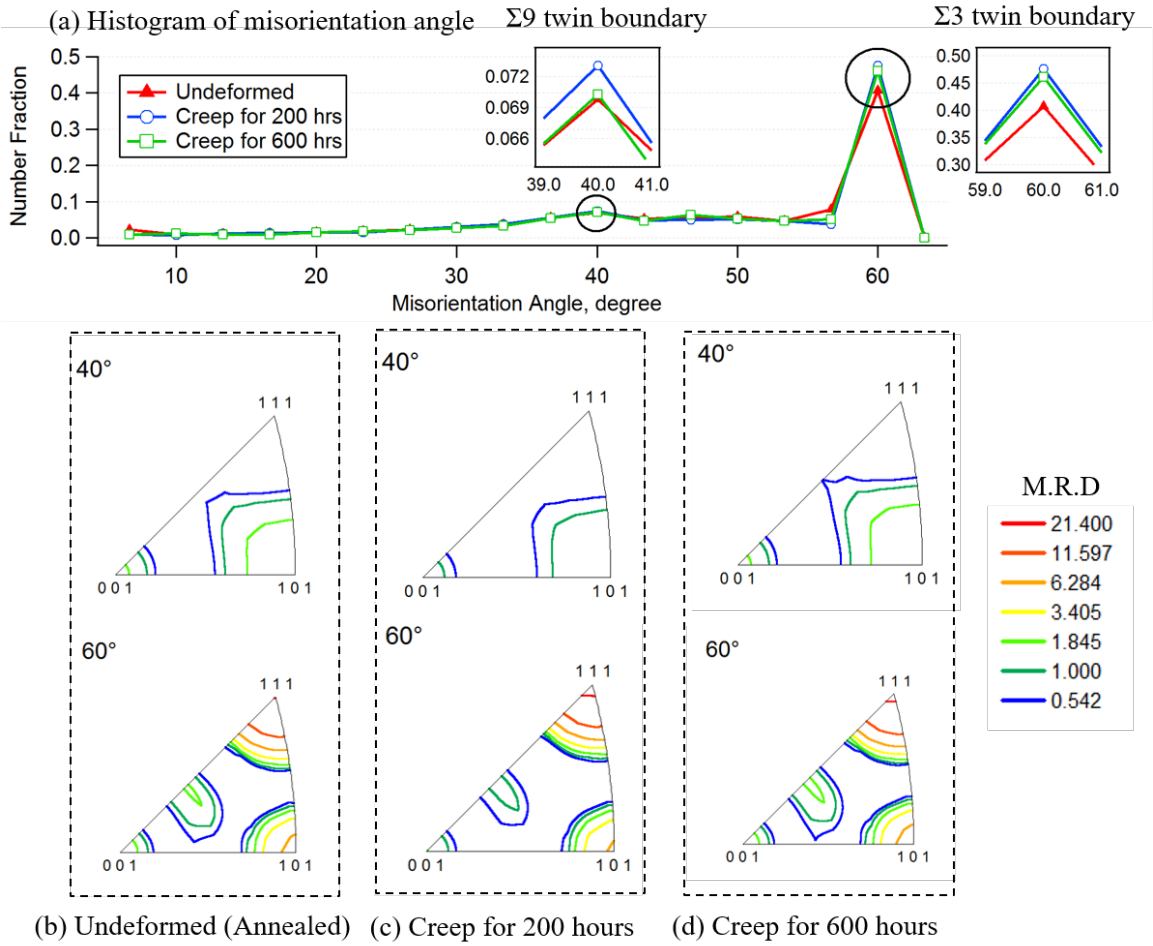

Figure 28. Grain boundary misorientation before and after creep deformation: (a) number fraction histogram of misorientation angle; (b, c, d) misorientation axis distribution for the undeformed and creep deformed states.

The misorientation distribution of grain boundary as displayed in Figure 28 shows slight increase (5% in number fraction) of 60° <1 1 1> (∑3) primary twin boundaries (TBs) after creep deformation. The number fraction change of TBs between 200-hour and 400-hour creep deformations is insignificant. The multiplication of primary twin boundary infers that primary twins are nucleated during the creep deformation process. Overall, the above results give a good measure of the steady-state creep regime microstructure for use in developing the polycrystalline DEM model.

2.2. Discrete Element Method (DEM) Model Development

All simulations were performed using the commercial software *PFC*^{3D} v5 (Itasca Consulting Group, Inc., Minneapolis, MN, USA), though this choice was made purely for convenience based on the authors' previous experience with the software; any number of other commercial or open source DEM implementations are compatible with our approach. Hardware requirements are the same as the *PFC*^{3D} v5 software hardware requirements. Documentation and additional codes employed are available from Matthew Evans upon request: matt.evans@oregonstate.edu.

2.2.1. *The Discrete Element Method*

The discrete element method was originally developed by (Cundall, 1971) for the modeling of rocks and later expanded to soils (Cundall and Strack, 1979). In this introduction, we present major points of the method, while for details of the implementation the reader is referred to (Potyondy and Cundall, 2004). In this work, the three-dimensional version of the DEM with spherical elements is employed.

Traditional DEM is predicated upon the simultaneous solution of Newton's equations of motion for each body in an assembly of discrete particles. Contacting particles interact via simple constitutive relations. Particle overlap is allowed at contacts (the so-called *soft contact* approach), but these overlaps are small relative to particle size (e.g., less than 1%). A given calculation cycle begins by identifying contact points and identifying their unit normals.

Figure 29 shows two interacting spherical elements and an element interacting with a rigid planar wall. The contact plane normal ($\mathbf{n}_c$) is defined by the line segment between the element centroids $\mathbf{x}_{p_i}$ or element centroid and nearest point on the wall, $\mathbf{x}_w$. The contact plane spans the contact point $\mathbf{x}_c$. **N.B.:** In DEM modeling, contacts may be either *real* or *virtual*. Real contacts occur when two bodies are actually in contact or overlapping. Virtual contacts exist when two bodies are proximal but not yet touching (typically, when their surface separation is 10^{-6} times the mean diameter of the two entities). In unbonded assemblies, this serves to provide computational efficiency in the contact detection algorithm (typically the most expensive part of the calculation). In bonded assemblies, however, this separation has physical meaning – two elements are able to have a physical separation, yet still be connected via a bond between them.

Herein, the behavior of elements contacts is described by a linear contact law. The normal force between two contacting elements is given by $F = -kx$ where k is particle stiffness and x is contact overlap. If the two elements are bonded (as they are in this work), an additional normal force is generated due to the presence of the bond, as described subsequently. Shear forces at contacts are linear and formulated incrementally.

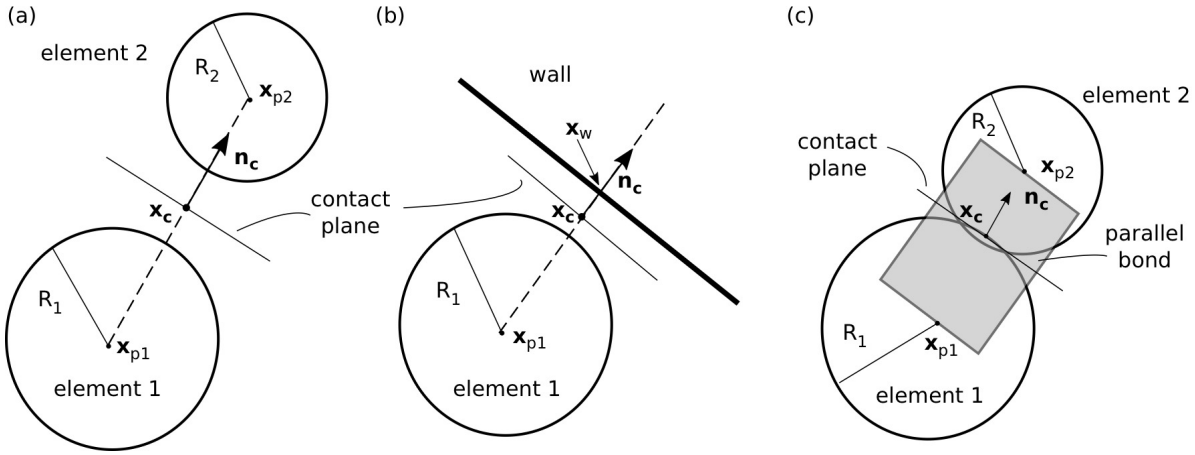

Figure 29. DEM components: (a) two interacting elements, (b) an element interacting with a wall, and (c) two elements bonded with a parallel bond.

The resultant force (and subsequently, the equation of motion) for a single element is defined as:

$$\mathbf{F} = \sum_{i=1}^{N_c} \mathbf{F}_{ci} = m\mathbf{a}, \qquad \text{Equation 5}$$

where the total force $\boldsymbol{F}$ is the sum of forces $\boldsymbol{F}_{ci}$ due to the i^{th} neighboring element; N_c is the total number of contacts the element has formed, m is element mass, and $\mathbf{a}$ is the acceleration. Similarly, the total moment, $\boldsymbol{M}$, experienced by an element is:

$$\mathbf{M} = \sum_{i=1}^{N_c} \mathbf{M}_{ci} = I\dot{\boldsymbol{\omega}} = \left(\frac{2}{5}mR^2\right)\dot{\boldsymbol{\omega}}, \qquad \text{Equation 6}$$

where $\boldsymbol{M}_{ci}$ is the moment on the i^{th} element contact, I is the moment of inertia, $\dot{\boldsymbol{\omega}}$ is the angular acceleration, and we exploit the fact that, for spherical elements, moment is directionally independent. Each contact force $\boldsymbol{F}_{ci}$ and moment, $\boldsymbol{M}_{ci}$, is resolved into a normal component acting along the contact plane normal, $\boldsymbol{n}_c$, and shear component that lies in the plane. As mentioned previously, in simulations of unbound granular materials forces are related to the overlap of impinging elements as shown in Figure 29. Positive overlap generates repulsive force. This sign convention is natural for unbonded materials where contacts only work in compression and so there are no tensile forces, but it is the reverse of the convention typically used in solid mechanics.

To model monolithic materials, elements can be bonded together by replacing the asymmetrical contact laws with cohesive interactions that can support tension. A common scheme for this is the *parallel bond* developed by Potyondy an Cundall (Potyondy and Cundall, 2004) and shown in Figure 29(c). The parallel bond represents two welded elements as a cylinder of material running between the element centers that can transmit both moment and force between the elements. The constitutive law for the parallel bond is used in the differential form:

$$\frac{d\mathbf{F}}{dt} = k_n A \frac{d\mathbf{u}_n}{dt} + k_s A \frac{d\mathbf{u}_s}{dt}$$
$$\frac{d\mathbf{M}}{dt} = -k_n J \frac{d\Delta\theta_t}{dt} - k_s I \frac{d\Delta\theta_b}{dt} \qquad \text{Equation 7}$$

where the force, $\boldsymbol{F}$, due to the normal, $\boldsymbol{u}_n$, and shear, $\boldsymbol{u}_s$, displacements, and the moment, $\boldsymbol{M}$, due to the difference in the twisting, $\Delta\boldsymbol{\theta}_t$, and bending, $\Delta\boldsymbol{\theta}_t$, rotations of the two elements are related by normal, k_n, and shear stiffness, k_s. The geometric terms A, I, and J are the bond's cross-sectional area, moment of inertia, and polar moment of inertia, respectively. For unbonded elements the interaction range is set by the element radii, as discussed previously. Parallel bonds, however, can be installed between any two elements with any equilibrium length, and thus once a DEM assembly is parallel bonded the elements should no longer be considered to be spherical. In this work, assemblies of elements were generated by simulating the dynamic packing of unbonded elements interacting through contact laws. Once a stable packing was achieved, the element-element contact laws were turned off and parallel bonds installed between all pairs of elements with a spacing less than a cutoff separation referred to as the *gap parameter*, $g_{c_{\max}}$, so that a bond is installed between elements i and j if:

$$g_{c_{\max}} \geq \left\| \mathbf{x}_{p2} - \mathbf{x}_{p1} \right\| - \left(R_1 + R_2 \right) \qquad \text{Equation 8}$$

where $\boldsymbol{x}_{p1}$ and $\boldsymbol{x}_{p2}$ are positions of the elements' centroids and R_1 and R_2 the element radii (Figure 1). In this work, the geometric terms A, I, and J are defined by the bond radius which is defined as the radius of the smaller element, $R_b = min\{R^{(1)}, R^{(2)}\}$ or the radius of the element at an element-wall contact.

Each simulation step in DEM consists of computing the total forces and moments for every element using Equation 5 and Equation 6. From these, accelerations, translational and angular velocities, and new element positions are computed with the Verlet algorithm (Verlet, 1967).

2.2.2. *Geometric algorithms and discretization scheme for DEM model*

DEM models are typically used to simulate discontinuous materials with a high degree of spatial heterogeneity. This approach is quite powerful, but implementation for continuum modeling is challenging. Of particular note is the need for force homogenization and equilibration across the sample space. We initially developed an algorithm that iterates forces in the assembly towards a constant value and produces a physically realistic elastic response, as shown in Figure 30.

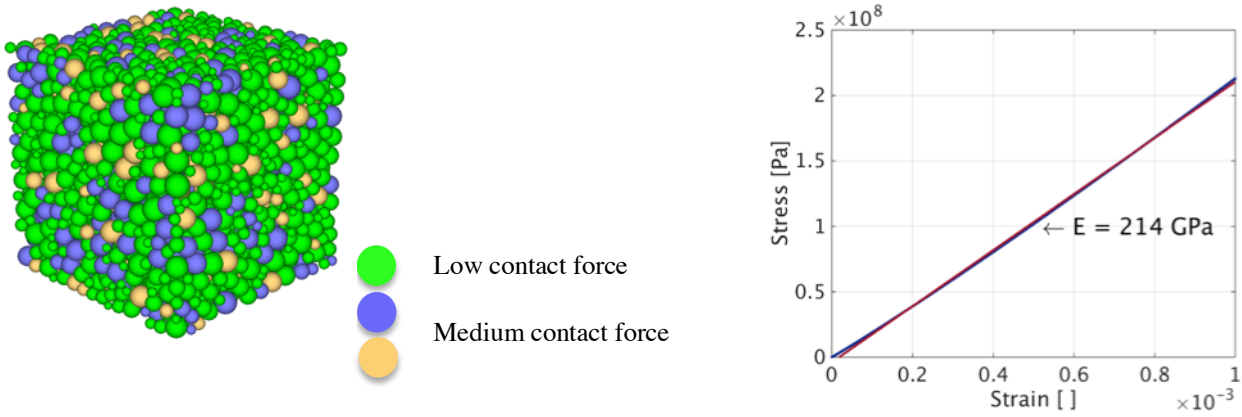

Figure 30. At left is a representation of the contact force distribution in our DEM model and at right is an elastic stress-strain response from our model with a physically realistic solid metal elastic modulus.

While Figure 30 shows an example isotropic response, the polycrystalline Nimonic 75 grain structure has been tessellated for the DEM model by a 3-D Voronoi algorithm that captures our measured distributions of grain size, grain orientation, and grain boundary misorientation. The measurements of those microstructural parameters were described above. As Σ3 and Σ9 annealing twin boundaries are unlikely to be initiation sites for creep damage (Zhang and Field, 2013), these boundaries are excluded for reconstructing the 3-D grain structure. An example of a 3-D tessellation is shown in Figure 31.

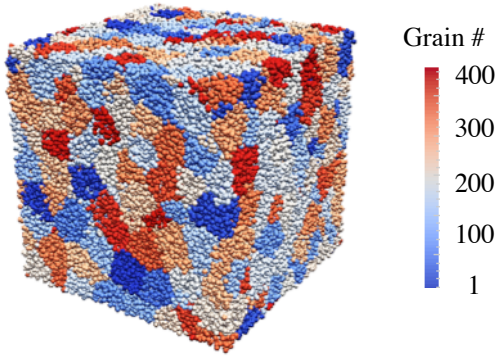

Figure 31. An example DEM model volume of a 3-D grain structure containing 400 crystalline grains.

2.2.3. *Determination of the Elastic Property Inputs for the Model*

To predict the elastic constants off Ni-20Cr as a function of temperature we have first calculated the material's elastic constants at zero Kelvin, and then used the softening of elastic constants in classical molecular dynamics simulations to extrapolate these properties to higher temperatures. Here we first report on the calculation of 0 K elastic properties using density functional theory (DFT), and then on the translation of these results to high temperature properties

2.2.3.1. DFT Calculation of Single Crystal Anisotropic Elastic Constants at 0 K

DFT calculations were performed on a single unit cell of in pure Ni and on a 2x2x2 supercell of Ni-20Cr with the atoms arranged in a special quasi-random structure (SQS) (Zunger et al., 1990). A SQS is an arrangement of the atoms in the supercell that possesses the same element-by-element pair correlation functions as would be found in a truly random solid solution, and thus correctly captures the long range interactions between the alloy constituents in the materials electronic structure. The SQS was generated using a reverse Monte Carlo approach in which Ni-Cr atom pairs are selected randomly and the positions in the supercell switched, and the switch kept or discarded probabilistically based on comparison of the pair distribution function of the trial configuration with that of a random solid solution. It should be noted that the ordering of the solute atoms on the lattice in the SQS breaks the cubic symmetry of the supercell and so elastic properties must be averaged over each of the three <100> type directions. The SQS supercell is visualized in Figure 32.

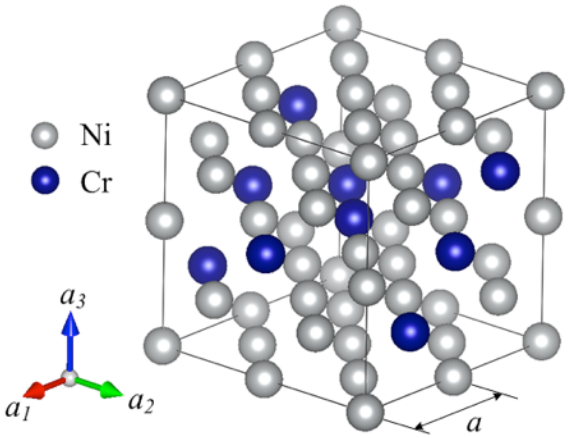

Figure 32. Special quasi-random structure (SQS) 2×2×2 supercell used in the DFT calculation.

The DFT calculations were performed using Vienna Ab initio Simulation Package (VASP). Projector-augmented plane-wave pseudopotentials (PAW) and generalized gradient approximation (GGA) of the exchange-correlation energy by Perdew-Burke-Ernzerhof (PBE) (Perdew et al., 1996) were included in the calculation. Before calculating of the elastic constants, convergence tests were carried out to calculate the total energy in a unit supercell by selecting cutoff energy varying from 260 eV to 480 eV, and Monkhorst-Pack K-point mesh size varying from N=1 to N=4. The purpose of the convergence test is to identify the optimized values of cutoff energy and K-point mesh size so that a reliable, computationally efficient, DFT calculation is enabled. The lattice parameter used in the convergence test is assumed to be 3.52 Å. The optimized K-point mesh size and cutoff energy were obtained to be N = 3 and E_{cut} = 440 eV, respectively (Figure 33). The supercell structure was then relaxed by choosing lattice parameter ranging from 3.51 Å to 3.53 Å. The equilibrium lattice parameter corresponding to the minimum total energy was found to be 3.523 Å (Figure 34).

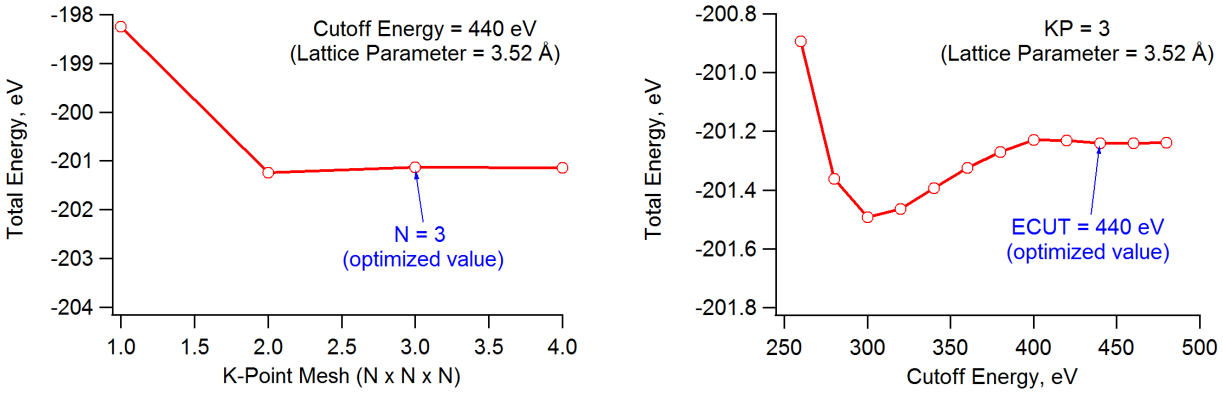

(a) (b)

Figure 33. Convergence tests for optimized K-point mesh size (a) and cutoff energy (b).

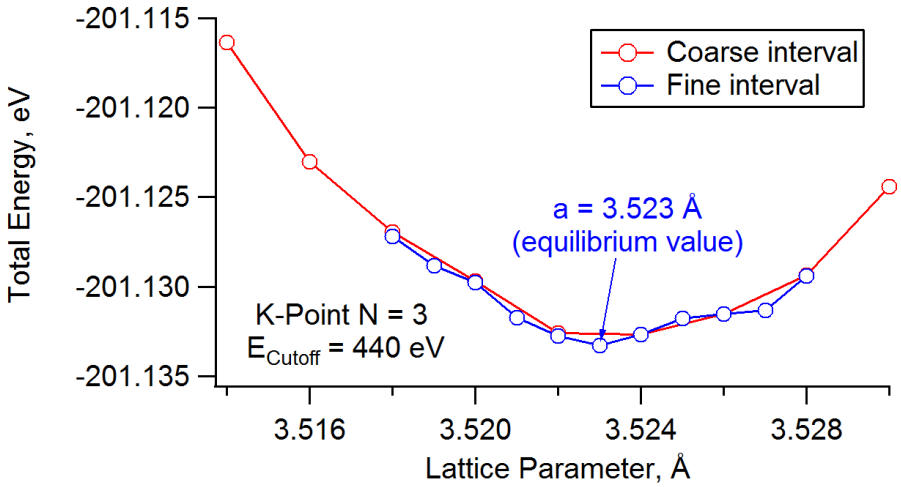

Figure 34. Calculation of equilibrium lattice parameter.

For face centered cubit (FCC) Ni-20Cr alloy, there are three independent anisotropic elastic constants, namely C_{11}, C_{12}, and C_{44}. C_{11} and C_{12} are associated with the bulk modulus B and Zener's modulus C' (or tetragonal shear modulus), which are defined as:

$$B = \frac{1}{3}(C_{11} + 2C_{12}) \qquad \text{Equation 9}$$

$$C' = \frac{1}{2}(C_{11} - C_{12}) \qquad \text{Equation 10}$$

If we elastically deform the unit supercell by applying a hydrostatic strain tensor then

$$\varepsilon_{ij} = \begin{pmatrix} \varepsilon & 0 & 0 \\ 0 & \varepsilon & 0 \\ 0 & 0 & \varepsilon \end{pmatrix} \qquad \text{Equation 11}$$

We are able to determine the bulk modulus B by fitting the calculated total energy E as a function of volume V (Mehl et al., 1990):

$$B = \frac{1}{3}\left(C_{11} + 2C_{12}\right) = V_0 \left.\frac{d^2 E}{dV^2}\right|_{V=V_0} \qquad \text{Equation 12}$$

where V_0 is the equilibrium supercell volume corresponding to the minimum total energy. To obtain the Zener's modulus, we elastically deform the supercell by applying a volume conservative tetragonal strain tensor:

$$\varepsilon_{ij} = \begin{pmatrix} \varepsilon & 0 & 0 \\ 0 & -\varepsilon & 0 \\ 0 & 0 & \varepsilon^2/\left(1-\varepsilon^2\right) \end{pmatrix} \qquad \text{Equation 13}$$

The associated change of total elastic energy can be calculated as:

$$\Delta E = V \sum_{i=1}^{3}\sum_{j=1}^{3} \frac{1}{2}\sigma_{ij}\varepsilon_{ij} = 2VC'\varepsilon^2 + O\left(\varepsilon^3\right) = V\left(C_{11} - C_{12}\right)\varepsilon^2 + O\left(\varepsilon^3\right) \qquad \text{Equation 14}$$

The Zener's modulus C' can be determined by fitting the change of total energy ΔE as a function of ε^2

$$C' = \frac{1}{2V} \left.\frac{d\left(\Delta E\right)}{d\left(\varepsilon^2\right)}\right|_{V=V_0} \qquad \text{Equation 15}$$

where V_0 is the volume corresponding to the minimum change of total energy. If we elastically deform the supercell by applying a volume-conservative orthorhombic strain tensor:

$$\varepsilon_{ij} = \begin{pmatrix} 0 & \varepsilon & 0 \\ \varepsilon & 0 & 0 \\ 0 & 0 & \dfrac{\varepsilon^2}{1+\varepsilon^2} \end{pmatrix} \qquad \text{Equation 16}$$

The associated change of total elastic energy can be calculated as:

$$\Delta E = V\sum_{i=1}^{3}\sum_{j=1}^{3}\frac{1}{2}\sigma_{ij}\varepsilon_{ij} = 2VC_{44}\varepsilon^2 + O\left(\varepsilon^3\right) \qquad \text{Equation 17}$$

So the elastic constant C_{44} can be determined by fitting the change of total energy ΔE as a function of ε^2:

$$C_{44} = \frac{1}{2V}\frac{d\left(\Delta E\right)}{d\left(\varepsilon^2\right)}\bigg|_{V=V_0} \qquad \text{Equation 18}$$

where V_0 is the volume corresponding to the minimum change of total energy. Based on Equation 12, Equation 15, and Equation 18, we calculated the bulk modulus B, Zener's modulus C', and C_{44} for Ni-20Cr alloy to be 204.1 GPa, 60.0 GPa, and 131.7 GPa, respectively (see Figure 35a, b, c). The bulk modulus, Zener's modulus, and elastic constants C_{11}, C_{12}, C_{44} are also compared to DFT calculation for pure nickel, as shown in Figure 35 and listed in Table 7.

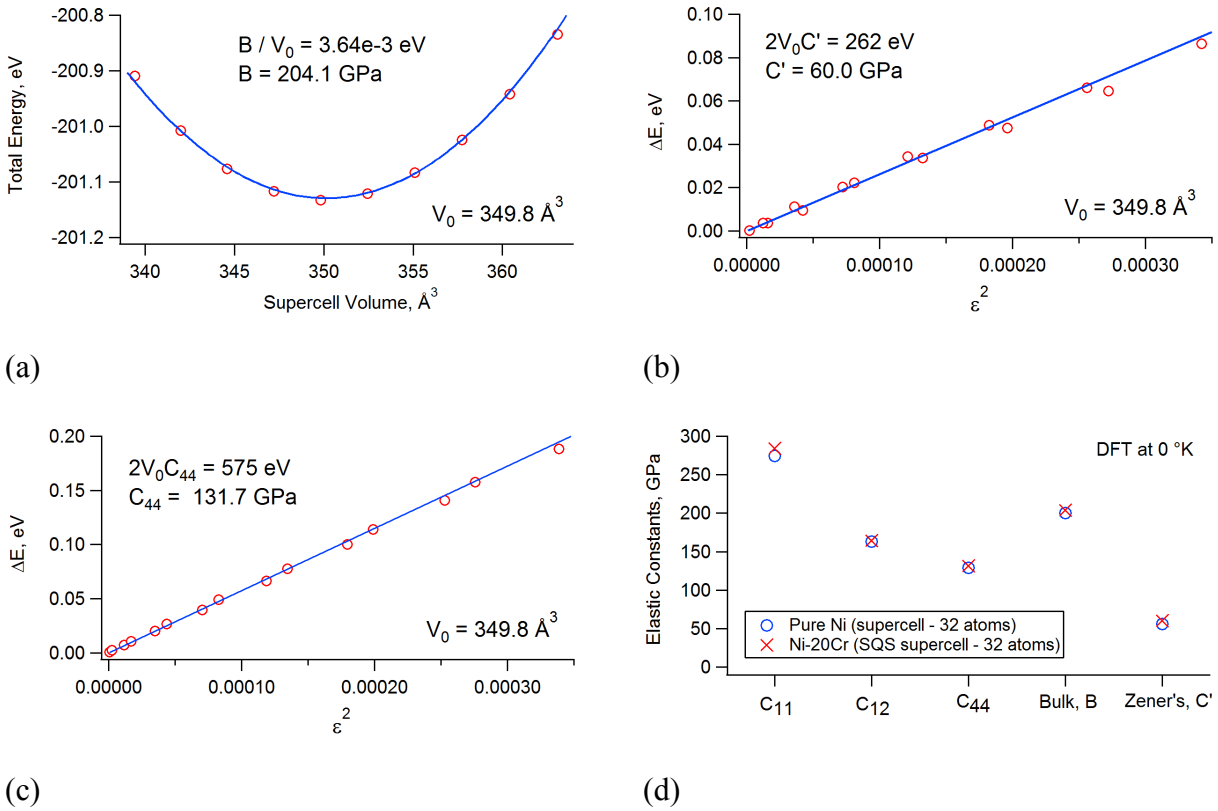

Figure 35. Calculation of bulk modulus B (a), Zener's modulus C' (b), and C_{44} (c) through elastically deforming supercell by applying hydrostatic strain tensor, volume-conservative tetragonal strain tensor and orthorhombic strain tensor, respectively. (d) Comparison of the elastic constants of Ni-20Cr to those of pure nickel.

Table 7. Comparison of 0-K equilibrium lattice parameter, bulk modulus, Zener's modulus, and anisotropic elastic constants calculated by DFT between pure Nickel and Ni-20Cr alloy.

Material	Equilibrium lattice parameter, a, Å	Bulk modulus B, GPa	Zener's modulus C', GPa	C_{11}, GPa	C_{12}, GPa	C_{44}, GPa
Pure Ni (2x2x2 supercell)	3.518	200.1	55.7	274.3	163.0	128.8
Ni-20Cr (2x2x2 SQS supercell)	3.523	204.1	60.0	284.1	164.1	131.7

2.2.3.2. Extrapolation of 0K results to 600°C

The isothermal elastic constants of a material are given by the second derivative of the material's volumetric Helmholtz free energy, F_v, with respect to strain:

$$C_{ij} = \frac{\partial^2 F_v}{\partial \varepsilon_i \partial \varepsilon_j} \qquad \text{Equation 19}$$

This contains two contributions: the curvature of the interatomic potentials, and the change in the internal vibrational energy of the solid as a result of deformation. On increasing the temperature of the solid, both of these contributions change. The system samples more of the curvature of the soft tails of the interatomic potential, and also there is a change in the distribution of occupied phonon modes. The temperature range of interest for this work is around 600°C (873 K), which is much larger that the Debye temperature for Nickel (450 K), and thus we can ignore the quantum mechanical filling of vibrational modes (the second contribution) and use classical molecular dynamics to determine the contribution of the anharmonisity in the interatomic bonding. As these molecular dynamics simulations must be performed using forces obtained from first principles, these calculations are computationally expensive, and thus we have used a set of test simulations with forces obtained from empirical potentials to carefully identify the most computationally efficient set of parameters that yields a meaningful prediction.

Four sets of simulations were performed which test both the validity of using only a 3x3x3 supercell and the ability of the SQS to reproduce the properties of the random solid solution.

Elastic constants were computed from fits to the averaged pressure (stress) response of the materials to quasistatic isothermal deformation of the material at different temperatures. For each simulation, the system was equilibrated under NPT, and then switched to the NVE ensemble with the averaged stress tensor recorded as a function of a slow homogeneous deformation of the simulation box. The interactions of Ni and Cr were modeled using the embedded atom method (EAM), and the average of 20 simulations was used to obtain each datum. Figure 36 shows the comparison of the reported experimentally measured elastic constants of pure Ni along with the elastic constants obtained by us using 108, and 2048 atoms simulation cells. The MD results for the two system sizes fall exactly on top of each other, indicating that the smaller simulation cell captures the elastic softening but includes larger uncertainty. This is an important result for our

future DFT-MD simulations. Secondly the empirical potentials track the overall trend in the softening reasonably well, but over estimate the softening in C_{12} and underestimate the softening in C_{11} and C_{44}. The second plot in Figure 36 shows the comparison of elastic constants of Ni and Ni-20Cr obtained though MD simulations. For the alloy the results are shown for both the large random alloy, and the smaller SQS, indicating that the SQS performs well at reproducing the properties of the random alloy. The elastic constants for the alloy are softer than those of pure Ni, but the softening behavior tracks almost identically.

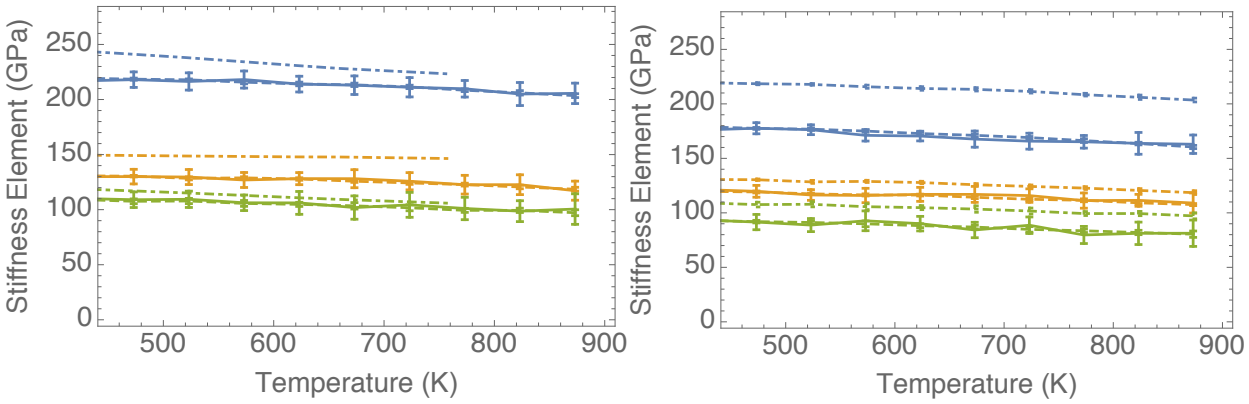

Figure 36. Plots of elastic constants of Ni and Ni-20Cr as a function of temperature above the Debye temperature. C_{11}, C_{12}, and C_{44} are plotted in blue, gold, and green respectively. The left plot shows the comparison of experimental (dot-dashed) and values obtained from MD simulations of 108 atoms (solid) and 2048 atoms (dashed). The right plot shows the comparison of MD obtained elastic constants of Ni (dot-dashed) with Ni-20Cr (solid: 108 atoms, dashed: 2048 atoms).

While the trend in individual elastic constants track the experimental values, the trends in both elastic anisotropy ratio, $2C_{44}/(C_{11}-C_{12})$, and Poisson's ratio do not follow the experimental trend (Figure 37). This indicated a limitation of using EAM potentials, which are fit to reproduce 0 K elasticity, the crystal's lattice parameter, and the binding energy, but not to reproduce the anharmonicity in the interatomic bonding. It should be noted that the 0 K DFT results do a much better job at reproducing the anisotropy ratio (2.31 for Ni and 2.20 for Ni-20Cr).

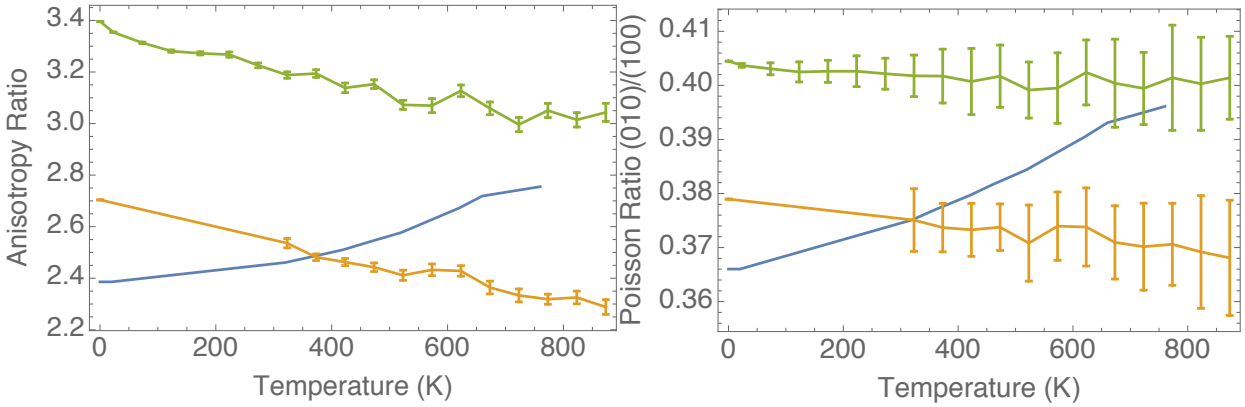

Figure 37. Plots of the anisotropy ratio (left) and (100) Poisson's ratio (contraction along (010)/due to stress along (100)) for Ni and Ni-20Cr as a function of temperature above the Debye temperature. Blue line is experimentally results for Ni, gold for Ni obtained with MD using EAM potentials, and the green line for Ni-20Cr from MD with EAM.

While the results above indicate a problem with the EAM for capturing subtleties in the temperature dependence of elastic response of Ni alloys, the EAM prediction for the averaged isotropic properties of the Ni-20Cr alloy is reasonable, as shown in Figure 38. Both plots show the experimentally measured Young's modulus for poly crystalline Ni-20Cr. The computed temperature dependent values of the elastic stiffness tensor as used to compute the polycrystalline Young's modulus using both the Voigt (average stiffness) and Reuss (average compliance) models which provide lower and upper bounds, respectively, for the elastic response of a polycrystalline assembly.

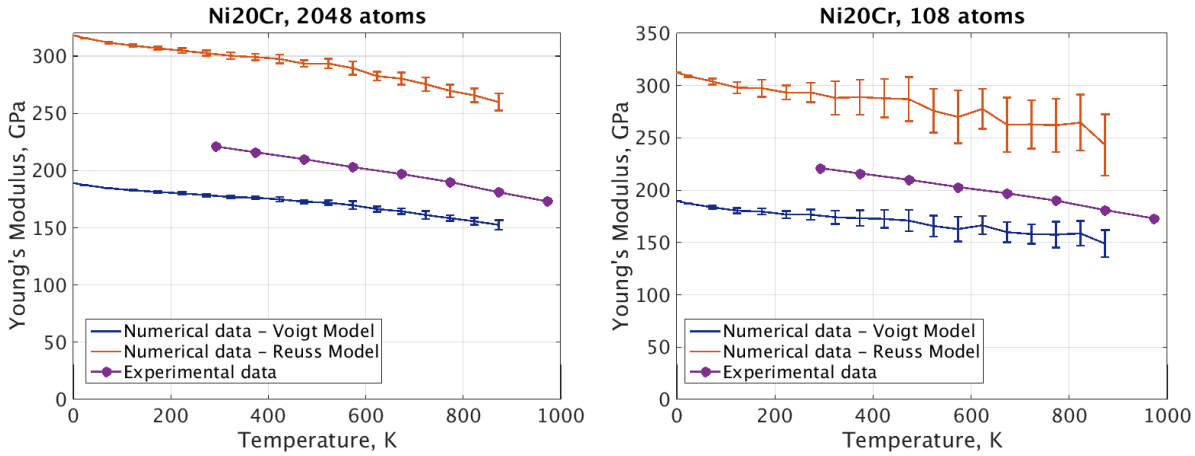

Figure 38. Young's modulus in terms of elastic constants computed with molecular dynamics at different temperatures compared against experimental data. Left image are results for 2048 atoms and right image are ones for 108 atoms built with special-quasi-random structures.

From these results we conclude that, for our current needs in this project, the experimentally obtained elastic constants for Ni can be extrapolated to higher temperature by fitting Watchman's functional form of the elastic softening:

$$C_{ij}(T) = C_{ij}^{o} - B_{ij} T e^{-\frac{T_M}{T}}, \qquad \text{Equation 20}$$

where C^o_{ij} is the 0 K elastic constant, B_{ij} is a parameter related to the Gruneisen parameter, and T_M is a temperature related to the Debye temperature for vibrations along the ijth deformation mode. The elastic constants for Ni-20Cr at high temperature can be obtained to a first approximation by shifting the C^o_{ij} for pure Ni to that for Ni-20Cr that we have already computed using DFT. Thus, in this manner we have identified an initial set of elastic constants for our model.

2.2.4. *Isotropic elasticity in DEM*

2.2.4.1. General model components of isotropic elasticity model in DEM for metallic materials

Two main components of the isotropic elasticity model were: i) Creation of representative DEM assemblies that can be used for simulation of continuum solids, ii) Ensuring the same elastic response in tension and compression characteristic of crystalline metallic materials.

While heterogeneity of DEM is a powerful and advantageous feature for modeling of continuum solids, its extent has to be controlled in order to obtain meaningful continuum behavior. Figure 39a shows a typical DEM assembly with a highly heterogeneous element size distribution. A broad size distribution, characteristic of many granular materials, leads to large local heterogeneity of materials and phenomena such as force percolation (Figure 39b and Figure 39c) where minority of elements carry majority of forces. To avoid this in continuum modeling the isotropic elasticity model had its size distribution reduced to $\Delta R = \bar{R}/6$ where $\bar{R}$ is the arithmetic mean element radius. This size distribution prevents crystallization and keeps random element arrangement, while allowing for less variation in material properties and element force propagation capabilities.

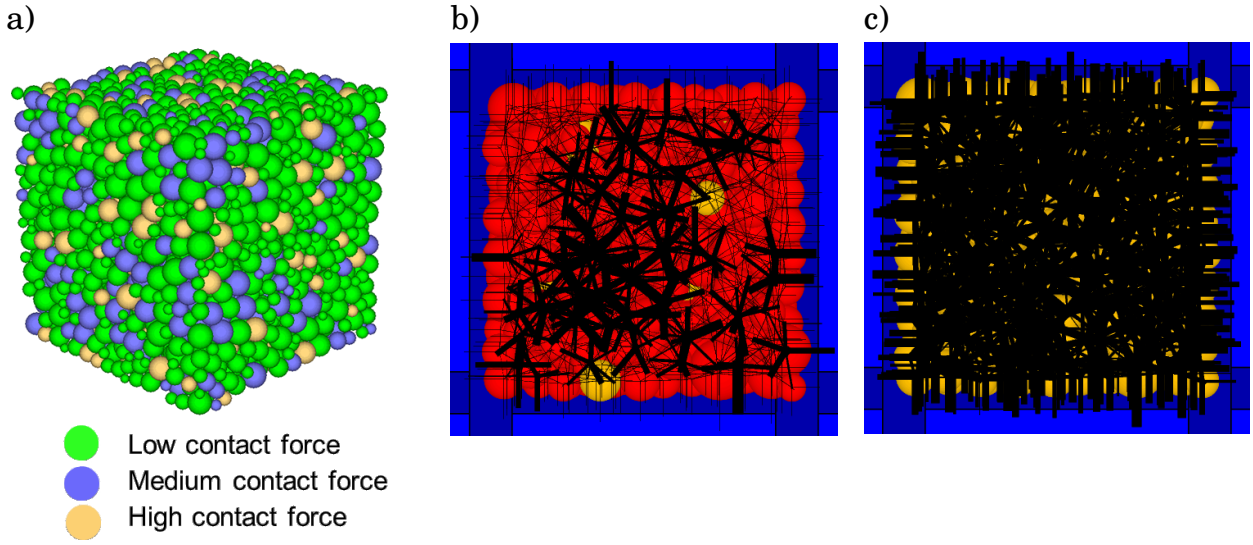

Figure 39. Stress distribution in a DEM assembly: a) Typical, non-uniform stress distribution in a granular medium. Colors indicate the relation of average force on a particle to assembly mean; b) and c) - force percolations; thickness of the bar is proportional to the magnitude of the force at a given contact. b) Force percolation characteristic for non-uniform assemblies as in a) - majority of the load is carried by only small number of particles; c) Greatly reduced force percolation after assembly generation and pre-processing steps applied in this work.

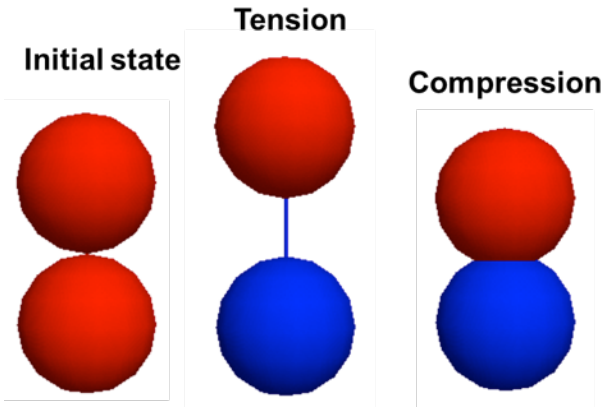

Figure 40. Two bonded elements subject to first tension, then compression. Material response needs to be the same in tension and compression in order for DEM models to correctly capture metal behavior.

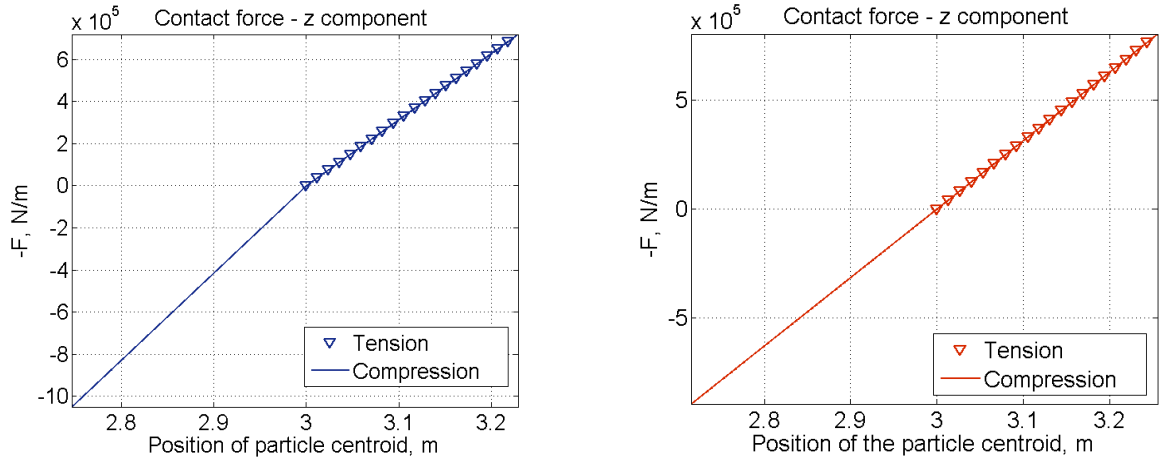

Figure 41. Force vs. displacement of the upper element from Figure 40. In the plot on the left, the slope of the line changes in compression. In the plot on the right, the slope does not change, which is the desired behavior.

To ensure the elastic tension-compression response characteristic of metallic materials, element stiffnesses were set to zero and only the parallel bonds contributed to material deformation. As shown in Figure 40-Figure 41, a non-zero element stiffness results in different force-displacement response in compression and in tension, which is not desirable in most of this work.

2.2.4.2. Assembly generation

Element assemblies were generated by randomly positioning elements in a cubical or rectangular space until a predefined void fraction of 0.40 was achieved. The void fraction was selected to be approximately halfway between the best estimates for the random close pack (RCP) case of 0.36 and the jamming transition of 0.44 where an unbonded assembly will become unstable and readily flow. Element radii were randomly drawn from a uniform distribution with a range $\Delta R = \bar{R}/6$ where $\bar{R}$ is the arithmetic mean element radius.

Mass-scaling was employed to improve calculation speed; in this approach, element sizes are increased by several orders of magnitude to increase the critical time step for numerical stability (see, e.g., (Belheine et al., 2009; Evans and Frost, 2007; Ning et al., 2015; Yun and Evans, 2011; Zhao et al., 2017)). Simulations were performed in the absence of gravity so that the increased element sizes do not generate excessive self-weight within the assembly. Changing the particle size also affects the dimensionless inertial number, I, which is used to define the line of demarcation between quasi-static and dynamic simulations (Roux and CHevoir, 2005): $I = \dot{\gamma} d / \sqrt{P/\rho}$, where $\dot{\gamma}$ is strain rate, d is element diameter, P is pressure, and ρ is particle density. Simulations with an inertial number less than 10^{-3} are quasi-static. In the current work the average inertial number is lower than 5×10^{-4}.

After the model domain was randomly populated with elements the system was relaxed by simulating the evolution of the system with damped dynamics until element accelerations are minimized. After equilibration, all neighboring elements within a chosen cutoff distance (called the gap cutoff parameter, $g_{c,\,max}$) were fused together with parallel bonds to form a contiguous network, and then the bounding walls were removed. Stress equilibration is not necessary as once parallel bonds are installed the elements' contact stiffnesses are removed. At this point the elements cease to be particle-like and are instead a trellis of *bonds*, all initially fully relaxed with no internal forces or moments. The total number of bonds formed is a function of the gap cutoff parameter. If the gap between elements is smaller than the predefined gap parameter, $g_{c,\,max}$, a bond will form between these elements.

2.2.4.3. Isotropic elasticity for materials without elastic tension-compression symmetry

Besides the zero-element stiffness model, we have also implemented strategies for development of models with a non-zero element stiffness which can be useful for continuum materials which response is not the same in tension and compression. The development consisted of two additional preprocessing steps in between first and second generation step described in the previous section:

1) Removal of "floaters"

"Floaters" are elements generated in DEM that have no or too little contacts. They are a numerical artifact and need to be removed to provide reliable models. Implemented was a floater-removal algorithm based on one proposed by (Potyondy and Cundall, 2004). Algorithm changed the size of elements until their number of contacts becomes physically admissible while their average contact force remains within fixed interval around mean contact force of the whole assembly. Figure 42 shows the result of applying our floater removal algorithm. Values of contact forces carried by elements increased by two orders of magnitude compared to newly generated assembly due to increased number of element contacts.

2) Reduction of locked-in stresses

Locked-in stresses are residual stresses present in a DEM assembly due to its discrete nature rather than numerical features. They originate from unhomogeneous stress distribution related to element size distribution as well as varying coordination numbers. After bonding the assembly, large locked-in stresses would put elements in excessive tension or compression introducing bias in the simulations of continuous materials. To reduce locked-in stresses implemented was an algorithm similar to one used for removal of "floaters". Namely, the element size was changed

until the contact force of that element was below an upfront set threshhold - a very low force value, negligible compared to meaningful forces developed in deformation simulations.

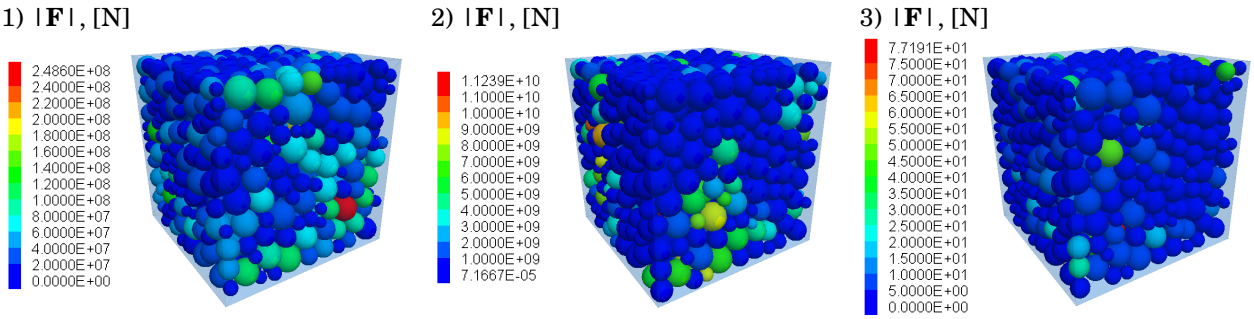

Figure 42. Generation and pre-processing of a DEM assembly with non-zero element stiffness. 1) Generation of a random assembly of polidisperse spherical elements 2) Assembly after removal of floaters 3) Assembly after reduction of locked-in stresses. |F| is the magnitude of the total contact force on each element. Forces after Step 2) are larger due to increased number of contacts. Forces in 3) are intentionally reduced to low values and made more uniform (Figure 39b) and c).

2.2.4.4. Results of implementing isotropic elasticity for metals in DEM

A stress-strain response from a representative model is shown in Figure 43. The deformation was driven by top and bottom walls and the response was linear and tension-compression symmetric. The Young's modulus value was within the range of values for metals and was readily adjustable by modifying the stiffness of parallel bonds allowing it to reach any value. On the other hand, the Poisson's ratio was limited to values around 0.18-0.25. Such restricted Poisson's ratio also arises in other emerging mesoscopic methods for simulating continuum materials such as bond-based peridynamics (Kumar et al., 2016; Madenci and Oterkus, 2016a).

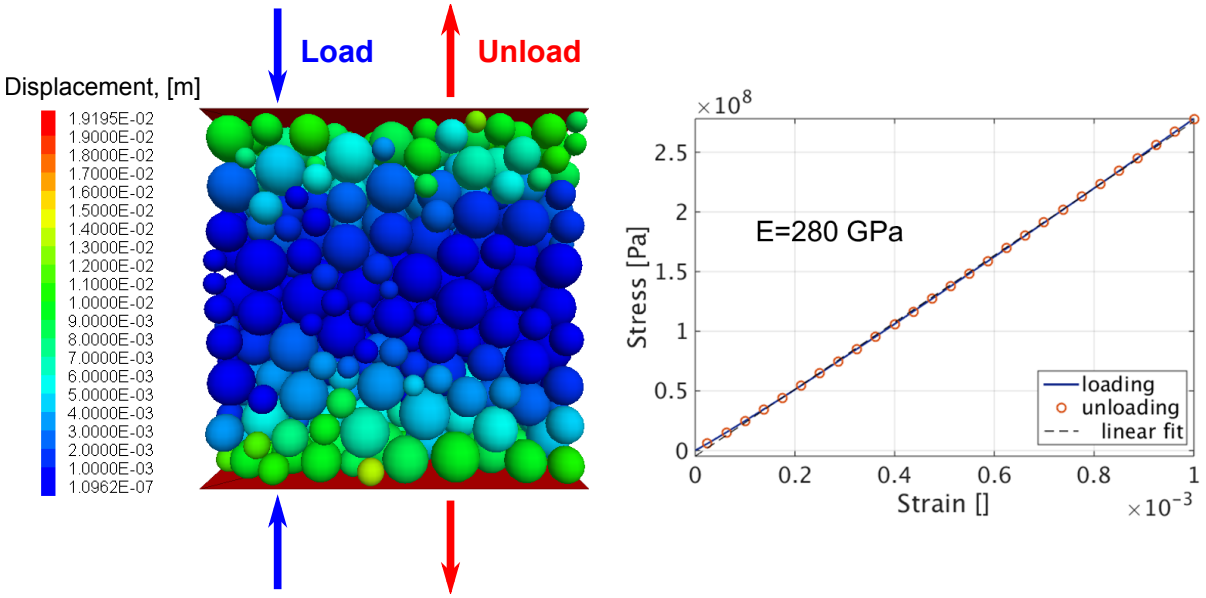

Figure 43. Elastic deformation of an isotropic material modeled with DEM. Assembly is first loaded, then unloaded. Stress-strain curves during both processes overlap and show a linear trend. Elements are colored based on displacement which values are consistent with element position relative to the walls that are initiating the deformation.

2.2.5. *Anisotropic Elasticity in DEM*

There were two approaches developed for DEM model of anisotropic elasticity, emergent and imposed approach. In the imposed approach, each contact was formulated such as to model cubic elasticity while in the emergent approach, cubic elasticity was a consequence of collective behavior of the entire, heterogeneous assembly. The imposed approach was completely developed while due to software limitations was implemented only on small assemblies thus it is in the preliminary result phase. The emergent approach was completed and is currently being considered for publication

2.2.5.1. Introduction of cubic anisotropy in DEM

The elastic response of cubically symmetric crystals is defined by the fourth rank elastic stiffness tensor with three independent moduli C_{11}, C_{12}, and C_{44} to provide the following stress-strain relationship:

$$\begin{pmatrix} \sigma_{xx} \\ \sigma_{yy} \\ \sigma_{zz} \\ \sigma_{yz} \\ \sigma_{xz} \\ \sigma_{xy} \end{pmatrix} = \begin{pmatrix} C_{11} & C_{12} & C_{12} & 0 & 0 & 0 \\ C_{12} & C_{11} & C_{12} & 0 & 0 & 0 \\ C_{12} & C_{12} & C_{11} & 0 & 0 & 0 \\ 0 & 0 & 0 & C_{44} & 0 & 0 \\ 0 & 0 & 0 & 0 & C_{44} & 0 \\ 0 & 0 & 0 & 0 & 0 & C_{44} \end{pmatrix} \begin{pmatrix} \varepsilon_{xx} \\ \varepsilon_{yy} \\ \varepsilon_{zz} \\ \varepsilon_{yz} \\ \varepsilon_{xz} \\ \varepsilon_{xy} \end{pmatrix} \qquad \text{Equation 21}$$

This relatively simple expression belies that cubically symmetric materials have a complex directionally dependent deformational response to a load. To present the rationale behind the approach set forth here for replicating this within DEM, it is necessary to describe the subtleties of cubic anisotropy in more depth. The extra variable needed to describe elastic response of cubic materials over isotropic media is often expressed as the Zener anisotropy ratio, $Z = \frac{2C_{44}}{C_{11}-C_{12}}$. This describes a material's deviation from isotropic behavior with a ratio of one indicating that the material is isotropic. Figure 44 shows the directionally dependent stiffness of three cubic materials with Z ranging from less than one to greater than one. The materials' stiffness in response to a uniaxial normal load varies with crystal loading direction (the left most plot in each sequence in Figure 44). Moreover, on any surface the material will have a hard and soft direction of shear. These soft and firm shear stiffnesses are plotted in the second and third plots in each sequence, respectively. The right-most plots show the soft and stiff shear stiffnesses overlaid, demonstrating that the soft and stiff shear stiffnesses are degenerate on the high symmetry {100} and {111} planes. In these plots, it can be seen that materials with an anisotropy ratio $Z < 1$ have the largest normal stiffness along ⟨100⟩ direction and the highest shear stiffness on {111} planes, while materials with $Z > 1$ have the largest normal stiffness along ⟨111⟩ direction and largest shear stiffness on {100}.

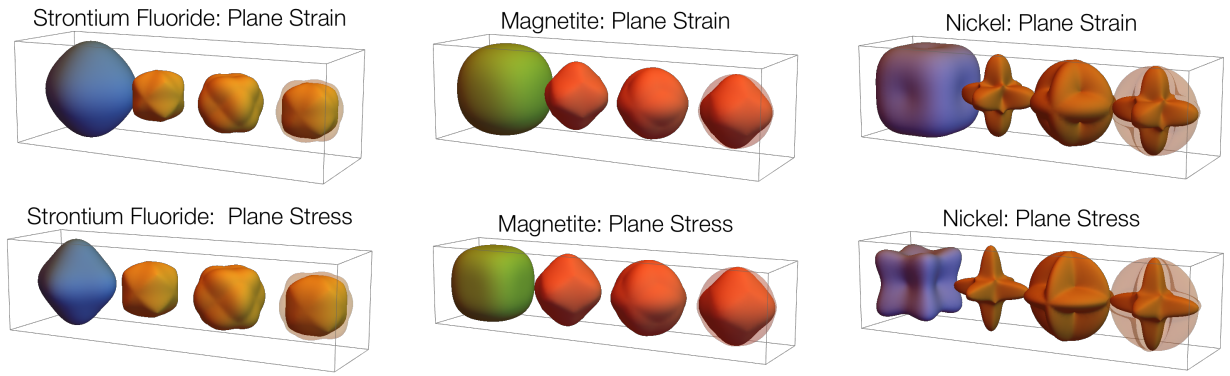

Figure 44. Elastic indicatrix for strontium fluoride, magnetite, and nickel. In each plot, the left most plot is the directionally dependent stiffness of the materials in response to a normal stress. The middle two plots show the shear stiffness along the soft and stiff shear directions on the plane normal to the polar direction, and the right most plot shows these shear stiffnesses overlaid. In the upper plots (labeled "Plane Strain") the stiffness is in response to an imposed uniaxial normal or in-plane shear strain while keeping the other strains values at zero, and the lower plots labeled "Plane Stress" are the stiffnesses in response to an imposed uniaxial normal or in-plane shear stress while keeping the other stress values at zero. In all plots, the values of stiffness are plotted scaled by the materials' C_{11}. The Zener ratios for strontium fluorite, magnetite and nickel are 0.78, 1.22, and 2.64, respectively. As the Zener ratio transitions from less than to greater than one, the materials' stiff axis transitions from ⟨100⟩ to ⟨111⟩.

The goal of this work was to capture cubic elasticity in DEM using the parallel bond formalism that is already implemented in many DEM software packages. In these packages, the user may assign a normal and shear stiffness for individual parallel bonds and thus the task becomes determining a method for assigning these stiffnesses based on bonds' *initial* orientations relative to a set of imagined crystallographic axes such that the emergent collective response of the bonded assembly is described by the stiffness tensor in Equation 21.

2.2.5.2. Imposed approach for modeling of anisotropic, cubic elasticity

The imposed approach attempted to introduce proper cubic anisotropy on each bond in the assembly by formulating the three stiffness parameters (Figure 44) from cubic stress-strain relation. This involved deriving bond stiffness that would satisfy stress-strain relation of a cubic material under plane strain conditions (Figure 44) and would preserve the three stiffness directions outlined in Figure 44. The resulting stiffness was expressed as a 3x3 matrix with components depending on normal direction, $\mathbf{v_n}$, and two shear directions, $\mathbf{v_p}$ and $\mathbf{v_e}$,

$$\begin{aligned}\mathbf{v_n} &= \left[\sin(\theta)\cos(\phi), \sin(\theta)\sin(\phi), \cos(\theta)\right] \\ \mathbf{v_p} &= \left[-\cos(\theta)\cos(\phi), -\cos(\theta)\sin(\phi), \sin(\theta)\right] \\ \mathbf{v_e} &= \left[\sin(\phi), -\cos(\phi), 0\right]\end{aligned} \qquad \text{Equation 22}$$

Where θ and ϕ are angles of initial bond orientation in spherical coordinates. The stiffness matrix and its components were

$$K(\theta,\phi)=\frac{1}{2}\pi R_C C_{11}^{*}\begin{bmatrix} A & F & E \\ F & B & D \\ E & D & C \end{bmatrix} \qquad \text{Equation 23}$$

$$A=\frac{-(\alpha-1)\beta\left(8\sin^4(\theta)\cos(4\phi)+4\cos(2\theta)\right)+11(\alpha-1)\beta+16\alpha}{16\alpha}$$

$$B=\frac{\beta\left(-8(\alpha-1)\sin^2(\theta)\cos^2(\theta)\cos(4\phi)+7(\alpha-1)\cos(4\theta)+9\alpha+7\right)}{16\alpha}$$

$$C=\frac{\beta\left(2(\alpha-1)\sin^2(\theta)\cos(4\phi)+(\alpha-1)\cos(2\theta)+3\alpha+1\right)}{4\alpha} \qquad \text{Equation 24}$$

$$D=\frac{(\alpha-1)\beta\sin^2(\theta)\cos(\theta)\sin(4\phi)}{2\alpha}$$

$$E=-\frac{(\alpha-1)\beta\sin^3(\theta)\sin(4\phi)}{2\alpha}$$

$$F=\frac{(\alpha-1)\beta\left(8\sin^3(\theta)\cos(\theta)\cos(4\phi)-2\sin(2\theta)-7\sin(4\theta)\right)}{16\alpha}$$

With

$$\alpha=\frac{2C_{44}^{*}}{C_{11}^{*}-C_{12}^{*}}$$

$$\beta=\frac{C_{44}^{*}}{C_{11}^{*}} \qquad \text{Equation 25}$$

Where C_{11}^{*}, C_{12}^{*}, and C_{44}^{*} are fitted parameters.

The preliminary results were obtained with a small, not necessarily representative assembly as the implementation of this model was restricted by the software and involved considerable computational performance decrease. The results, shown in Figure 45, indicated that this approach spanned a larger variety of cubic materials then the emergent approach as shown below. Even though the assembly size was not representative, the results still indicate the potential of this approach and justify its possible future development.

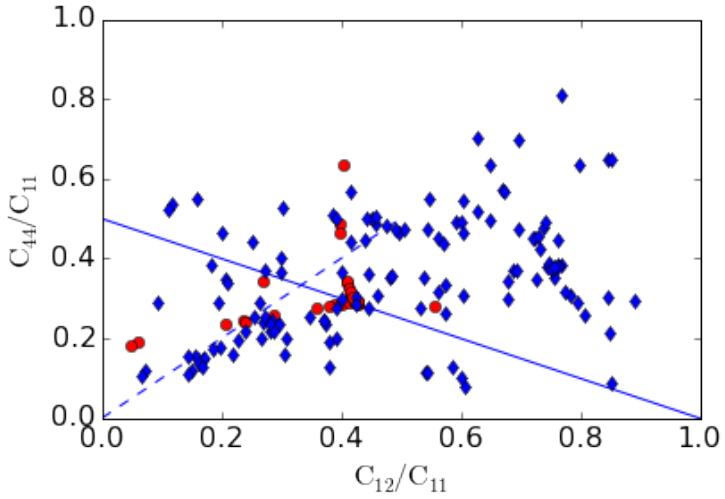

Figure 45. Ratios of elastic constants of real cubic materials (blue diamonds) and several materials modeled with imposed anisotropy approach (red circles).

2.2.5.3. Emergent approach for modeling of anisotropic, cubic elasticity

2.2.5.3.1. Emergent Approach formulation

The goal of this approach was to capture cubic elasticity in DEM using the parallel bond formalism that is already implemented in many DEM software packages. In these packages, the user may assign a normal and shear stiffness for individual parallel bonds and thus the task becomes determining a method for assigning these stiffnesses based on bonds' *initial* orientations relative to a set of imagined crystallographic axes such that the emergent collective response of the bonded assembly is described by the stiffness tensor in Equation 21.

As the packing of elements in DEM is random, and *on average* isotropic, it is presumed that the cubic response must arise from the collective behavior of the assembly rather than being met at each individual element. Within this approach there are three steps of reasoning that can be used guide the selection of a directionally dependent function for assigning bond stiffnesses: From von Neumann's principle, the angular dependence of the stiffness distribution must possess cubic symmetry, that is, four axes of threefold rotational symmetry about the <111> directions of the imagined crystal. Second, the stiffness tensor in Equation 21 possesses only three independent variables, of which only one describes the deviation from isotropic elasticity. With only one degree of anisotropy it is conjectured that *any* angular stiffness function with the proper rotational symmetry could give rise to collective behavior that is cubically anisotropic. Finally, in cubic materials there is a qualitative change in the directionally dependent normal stiffness as the Zener anisotropy ratio, Z, transitions from smaller to greater than one. As can be seen in Figure 7, for Z<1 the normal stiffness is maximal along <100>, while for Z>1 the modulus is stiffest along <111>. It is therefore presumed that changing the angular distribution of parallel bond stiffnesses from being maximal along <111> to maximal along <100> will alter the direction a system's deviation from isotropic elasticity.

To meet these criteria, one could construct angular bond stiffness functions from a sum of suitably symmetrized spherical harmonics functions, and then iterate the shape of the angular distribution to explore the angular function space. However, rather than doing this, the goal of

this article is to present a proof of concept that DEM can be used to model cubically elastic media. To this end, a more pragmatic approach was chosen, with two very simple piecewise functions defined as the external surface of a set of overlapping prolate spheroids (as shown in Figure 46). The shape of the distribution is described by a single parameter *a* that describes the aspect ratio (major to minor axes) of a family of spheroid with constant volume. One function is maximal along <100> and is composed of three spheroids with major axes along the <100> directions, while the second function, maximal along <111>, is composed of 4 co-centered spheroids with principal axes along the four <111> directions. In each case the spheroids the stiffness along a direction is given by the maximum radius of the three or four spheroids in which the radius is given by the equations:

$$k(\mathbf{n},a) = k_0(A/L)\, r_m(\mathbf{n},a) \qquad \text{Equation 26}$$

$$k_0(A/L) = \frac{A_b}{L_b} k_l \qquad \text{Equation 27}$$

and the dimensionless parameter

$$r_m(\mathbf{n},a) = \max\left(\{r_1, r_2, ..., r_N\}\right) \qquad \text{Equation 28}$$

n is the initial contact normal direction, A_b is the bond area, L_b the bond length, and k_l the stiffness magnitude. Bond length is defined as the sum of element radiuses, $L_b = R_1 + R_2$. N indicates the number of spheroids – 3 or 4 in this work. For the case of *N*=3 spheroids aligned along ⟨100⟩:

$$r_{i1} = \frac{a_i^{\frac{2}{3}}}{\sqrt{n_x^2 + \left(n_y^2 + n_z^2\right) a_i^2}} \qquad \text{Equation 29}$$

$$r_{i2} = \frac{a_i^{\frac{2}{3}}}{\sqrt{n_y^2 + \left(n_x^2 + n_z^2\right) a_i^2}} \qquad \text{Equation 30}$$

$$r_{i3} = \frac{a_i^{\frac{2}{3}}}{\sqrt{n_z^2 + \left(n_y^2 + n_x^2\right) a_i^2}} \qquad \text{Equation 31}$$

where n_x, n_y, and n_z are the *x*, *y*, and *z* components of unit vector ***n***. For the case of *N*=4 spheroids aligned along ⟨111⟩ the spheroid radii are given by:

$$r_{j1} = \frac{a_j^{\frac{2}{3}}}{\sqrt{\frac{1}{3}\left[\left(n_x - n_y + n_z\right)^2 + 2\left(n_x^2 + n_x n_y + n_y^2 - n_x n_z + n_y n_z + n_z^2\right)a_j^2\right]}} \quad \text{Equation 32}$$

$$r_{j2} = \frac{a_j^{\frac{2}{3}}}{\sqrt{\frac{1}{3}\left[\left(n_x + n_y - n_z\right)^2 + 2\left(n_x^2 - n_x n_y + n_y^2 + n_x n_z + n_y n_z + n_z^2\right)a_j^2\right]}} \quad \text{Equation 33}$$

$$r_{j3} = \frac{a_j^{\frac{2}{3}}}{\sqrt{\frac{1}{3}\left[\left(-n_x + n_y + n_z\right)^2 + 2\left(n_x^2 + n_x n_y + n_y^2 + n_x n_z - n_y n_z + n_z^2\right)a_j^2\right]}} \quad \text{Equation 34}$$

$$r_{j4} = \frac{a_j^{\frac{2}{3}}}{\sqrt{\frac{1}{3}\left[\left(n_x + n_y + n_z\right)^2 + 2\left(n_x^2 - n_x n_y + n_y^2 - n_x n_z - n_y n_z + n_z^2\right)a_j^2\right]}} \quad \text{Equation 35}$$

In this way, the anisotropic behavior of the DEM model is controlled by three independent tuning parameters: a_n and a_s, the anisotropy in the system of spheroids used to assign the normal and shear stiffnesses, respectively, and $a_k = k_n/k_s$, the ratio of the normal and shear stiffness magnitudes. In Appendix A, a general analytic model is presented for determining the elastic moduli of a material with angularly dependent stiffness functions if the bonds are all deformed uniformly due to a homogeneous deformation of the assembly. In Appendix B, the model is used to prove that that the stiffness functions based on overlapping spheroids (Equation 26- Equation 35) result in cubically anisotropic elasticity.

The expression chosen to represent the spheroids has the property of describing spheroids of constant volume independent of a. In exploring the space of model parameters, it is useful to define log normalized parameters α as the log of a shifted and scaled parameter that varies from 0 to 1 so that generally

$$\alpha = \frac{\log(a) - \log(a_{\min})}{\log(a_{\max}) - \log(a_{\min})} \quad \text{Equation 36}$$

The plots in Figure 46 show the angular dependence of normal stiffness (blue) and shear stiffness (gold) assigned to parallel bonds in the Z<1 and Z>1 models at the vertices of the domain of log-normalized model parameters. In this work, only the space of model parameters was explored with a_n and a_s running from 0.022 to 5 and a_k ranging from 0.005 to 1. Parameters outside this range would lead to unrealistically exaggerated shapes of the spheroid distributions. These extreme limiting shapes are shown on Figure 46 and include cases where the shear stiffness becomes much smaller than the

normal stiffness or the spheroid distribution becomes very narrow and pointy along its major directions.

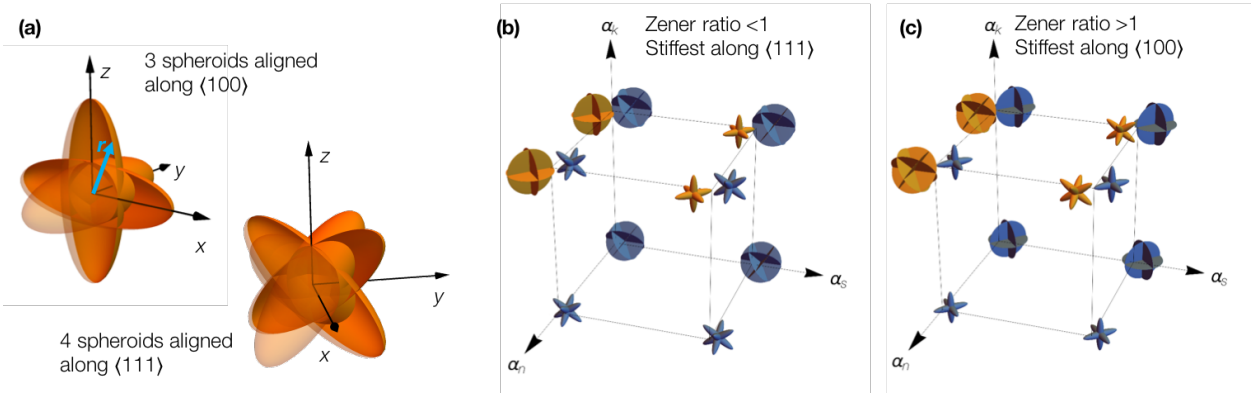

Figure 46. (a) Shows two piecewise angular functions with cubic symmetry defined as the outer surface of overlapping spheroids. The upper left function is constructed from three identical spheroids with major axes along the ⟨100⟩ directions and the function on the lower right is formed by four identical spheroids with major axes along the ⟨111⟩ directions. (b & c) The angular distributions of parallel bond normal stiffness (blue) and shear stiffness (gold) as a function of the model parameters a_n, a_s, and a_k plotted on the normalized log scale (see text and Equation 36 for explanation). In this space the log normalized parameters α_n and α_s span from 0.029 to 3.5 and α_k spans 0.078 to 5.5. Figure (b) is for modeling materials with Z<1 which are stiffest along the ⟨100⟩ directions and so the normal stiffness is represented by three spheroids aligned along these directions. Figure (c) shows stiffness distributions for modeling materials with Z>1 which are stiffest along the ⟨111⟩ directions, and so the normal stiffness is represented by four spheroids aligned along these directions.

2.2.5.3.2. Assembly generation and deformation

Assembly generation followed the steps described in Section 2.2.4.2. The influence of the gap cutoff parameter on the bonded network, the element coordination number, and the resulting elastic response was verified for a number of gap cutoff parameter values from $1.7\text{x}10^{-4}$ $\bar{R}$ to 0.8 $\bar{R}$.

The stiffnesses of individual bonds were assigned based on the bonds' initial orientation according to the spheroid distributions described in Equation 26- Equation 35. Elements that were initially bonded to box walls were used as "grip elements" to apply the elastic deformation, as discussed subsequently. A typical assembly is shown in Figure 47.

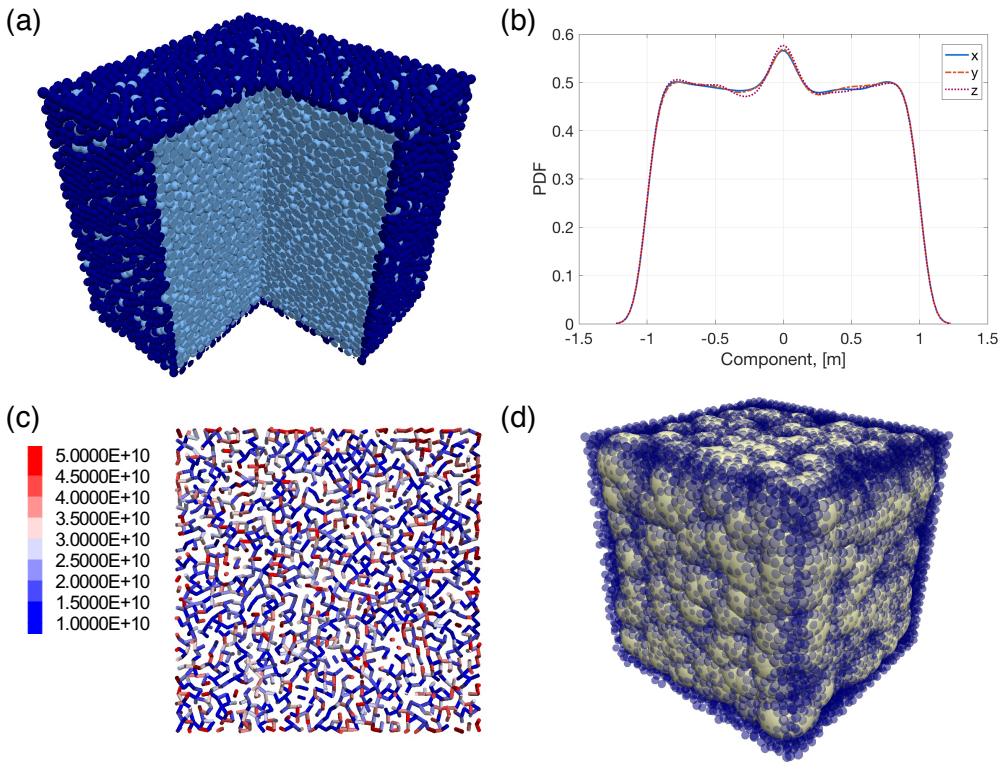

Figure 47. Properties of a typical modeled assembly: a) 3D representation, dark blue elements are the grip elements; b) probability distribution function of bond orientations; c) bonds as seen on a cross-section of the assembly colored by their anisotropic shear stiffnesses, [Pa/m]; d) measurement spheres.

2.2.5.3.3. Measuring Average Stresses and Strains in the Assembly

Stresses and strains in the assembly were computed using spherical measurement volumes (O'Sullivan, 2011; Potyondy and Cundall, 2004). Their radii and placement were random, the former being user-defined and the latter being constrained to exist fully within the assembly. Specifically, stresses and strain rates were measured and strains were computed through time integration of the measured strain rates. Stresses and strain rates were averaged over all measurement spheres. A total of 5,000 measurement spheres were typically used, each with a radius that corresponds to 6 times mean element radius. On average, 165 elements contributed to the stress/strain measurement of each measurement sphere.

2.2.5.3.4. Determining the Size of the Minimum Representative Volume

The minimum representative volume (MRV) is the smallest assembly with a sufficient number of elements to produce an average macroscopic response independent of assembly size. The MRV is typically evaluated by the convergence of effective properties, in this case the averaged C_{11}, C_{12} and C_{44} constants of a cubic material. The MRV was determined as the next-to-smallest assembly size in which variation in properties from one assembly to another originated solely from uncertainty in the randomly placed measurement spheres rather than the variations in assembly packing. The MRV was found for an assembly with model parameters described in Section 2.2.5.3.2. The gap parameter was 0.17 $\bar{R}$ which corresponded to a stable element coordination number of $C_n \approx 8$. Tested assemblies had between 5,000 and 80,000 elements.

2.2.5.3.5. Computing the Stiffness Tensor

MRV assemblies were used for computing the full stiffness tensor. Element assemblies were deformed along the six independent strain paths (three uniaxial strain and three pure shear) up to a maximum strain of 10^{-3}. During each of these simulated deformations the assembly's internal stress and strain state was determined using measurement spheres as described previously.

Uniaxial compression simulations were performed by setting the grip element velocities to

$$\mathbf{u} = -\dot{\gamma}\begin{bmatrix} x_c & 0 & 0 \end{bmatrix} \quad \text{Equation 37}$$

$$\mathbf{u} = -\dot{\gamma}\begin{bmatrix} 0 & y_c & 0 \end{bmatrix} \quad \text{Equation 38}$$

$$\mathbf{u} = -\dot{\gamma}\begin{bmatrix} 0 & 0 & z_c \end{bmatrix} \quad \text{Equation 39}$$

for deformations label as $\boldsymbol{\varepsilon}^{(1)}, \boldsymbol{\varepsilon}^{(2)}, \boldsymbol{\varepsilon}^{(3)}$ deformations respectively. For the cases of pure shear deformation strains $\boldsymbol{\varepsilon}^{(4)}, \boldsymbol{\varepsilon}^{(5)}, \boldsymbol{\varepsilon}^{(6)}$ are imposed by grip element velocities of:

$$\mathbf{u} = \dot{\gamma}\begin{bmatrix} 0 & z_c & y_c \end{bmatrix} \quad \text{Equation 40}$$

$$\mathbf{u} = \dot{\gamma}\begin{bmatrix} z_c & 0 & x_c \end{bmatrix} \quad \text{Equation 41}$$

$$\mathbf{u} = \dot{\gamma}\begin{bmatrix} y_c & x_c & 0 \end{bmatrix} \quad \text{Equation 42}$$

with $\dot{\gamma} = 0.2\ 1/\mathrm{s}$. For each of the six deformations linear fits of stress/strain *vs*. time were performed to each of the six stress/strain components so that the i^{th} and j^{th} components of stress and strain during the k^{th} deformation are described by:

$$\sigma_i^{(k)} = a_i^{(k)} t \quad \text{Equation 43}$$

$$\varepsilon_j^{(k)} = b_i^{(k)} t \quad \text{Equation 44}$$

where the slopes *a* and *b* are fitting parameters. The stress and strain are related via the stiffness tensor giving six sets of six coupled equations:

$$\sigma_i^{(k)} = C_{ij}\varepsilon_j^{(k)} \ , \quad i,j,k = 1\ldots6 \qquad \text{Equation 45}$$

(36 equations in total), which can be written also in terms of the fitted slopes:

$$a_i^{(k)} = C_{ij}b_j^{(k)} \ , \quad i,j,k = 1\ldots6 \qquad \text{Equation 46}$$

The stiffness tensor must be symmetric about its diagonal ($C_{ij} = C_{ji}$) and so contains only 21 independent elements. To reduce the system to 21 independent equations, the equations for stress elements under conjugate deformation paths were added together to obtain equations:

$$a_i^{(k)} + a_k^{(i)} = C_{ij}b_j^{(k)} + C_{kj}b_j^{(i)}, \text{ for } i \leq k \qquad \text{Equation 47}$$

The motivation for this approach is to impose only the conditions on C_{ij} required to satisfy Newton's third law. If the assembly is truly behaving as a cubically anisotropic elastic medium, it should be evident from computing the full stiffness tensor. The systems of 21 coupled equations in (Equation 46–Equation 47) were solved numerically using the generalized minimal residual (GMRES) method in *MATLAB* (Saad and Schultz, 1986). The results were rounded to 0.1 GPa.

Stiffness tensor components obtained with DEM have a certain amount of statistical noise because they are obtained with a randomly distributed bond network. This introduces slight differences in the values of elastic constants that would be otherwise equal, and similarly gives small non-zero values when they must be zero for a continuum. Uncertainties were quantified as the largest deviation of each group of constants from the mean value of a symmetrized tensor. This included the average magnitude of small non-zero terms in the stiffness tensor that should be equal to zero.

By computing the 21 independent elements of the stiffness matrix explicitly, and demonstrating the correct rotational invariance of the properties, it was shown that the assemblies' properties possessed the correct cubic symmetry. Once this was established further calculations of elastic moduli were performed using a single deformation with simultaneous compression along y with shear applied in the xz plane. This deformation was imposed by assigning a velocity $\boldsymbol{u}$ to the external grip elements based on their position relative to the center of the assembly, $\mathbf{x_c}=[x_c, y_c, z_c]$:

$$\mathbf{u} = \gamma\begin{bmatrix} z_c & \frac{y_c}{2} & x_c \end{bmatrix} \qquad \text{Equation 48}$$

where $\dot{\gamma}$ is the strain rate. Simulations were continued until the strains reached values between 1×10^{-5} and 1×10^{-3}.

2.2.5.3.6. Determining the Accessible Anisotropic Space

Parameter sweeps were used to determine the applicability of the proposed approach for modeling cubic materials. Parameter sweeps included changing values and ratios of the a_i and a_j constants (Equation 29 - Equation 35) as well as normal to shear stiffness ratios from Equation 26 - Equation 27. Simulations were performed for materials with Z>1 and Z<1. The limits of the anisotropic behavior were determined and results were compared with known values for common cubic materials (Simmons and Wang, 1971). Table 8 shows ranges of parameters used in the sweeps.

Table 8. Ranges of parameters used in determining the accessible anisotropic space.

Material	a_n	a_s	a_s/a_n	k_n	k_n/k_s
Z>1	0.01-5.0	0.01-100	0.01-500	$1x10^{13}$	1-5,000
Z<1	0.01-10.0	0.01-50	0.01-500	$1x10^{13}$	1-5,000

2.2.5.3.7. Minimum Representative Volume and Gap Cutoff Parameter

The *minimum representative volume* (MRV) was determined using a representative set of spheroid parameters for a material with a Zener ratio larger than one. Normal stiffness followed the 4 spheroid distribution with a_n=4.31 and k_n=1 × 10^{13} (Equation 26 and Equation 32 - Equation 35) and shear stiffness the three spheroid distribution with a_s=10.0 and k_s=3.55 x 10^{12} (Equation 26 and Equation 29-Equation 31). The influence of the gap cutoff parameter on bonding and the elastic response was also quantified. The variation in elastic constants with the number of elements in an assembly is shown in Figure 48a and MRV was chosen to measure 30,700 elements. Also, the coordination number as a function of maximum gap size (Equation 8) is shown in Figure 48b.

(a) (b)

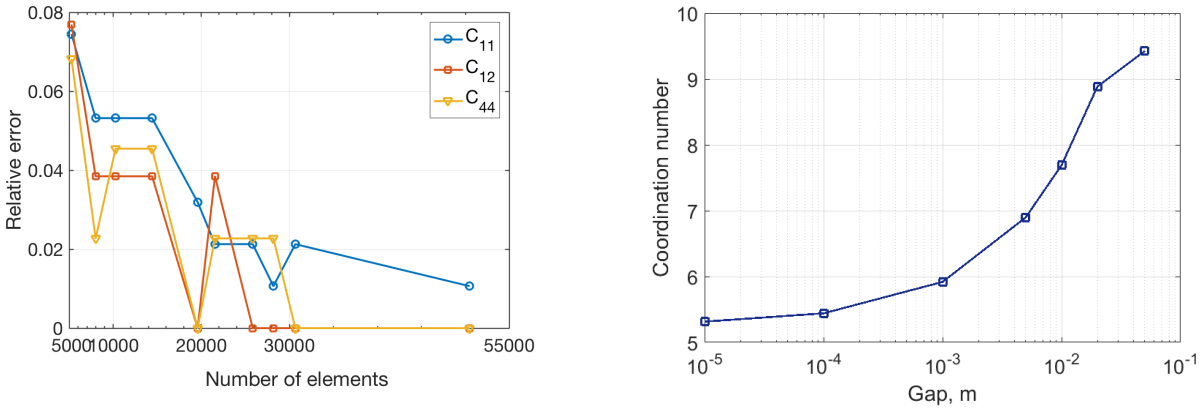

Figure 48. (a) Normalized elastic constants as a function of element number. MRV was chosen to have 30,700 elements. Values were normalized by those obtained with the largest assembly (82,238 elements) (b) Coordination number of a MRV assembly as a function of maximum gap parameter. Gap cutoff parameter was $0.17\bar{R}$ and yields a stable element coordination number of 7.7.

2.2.5.3.8. Description of the Model Assembly

The standard assembly used in subsequent simulations consisted of 30,700 elements held together with 118,008 bonds and an average coordination number of 7.7. This results in a cubic assembly with sides of length 60.0 $\bar{R}$. Figure 49 shows the elastically deformed assembly and Figure 50 shows an example elastic response of the assembly.

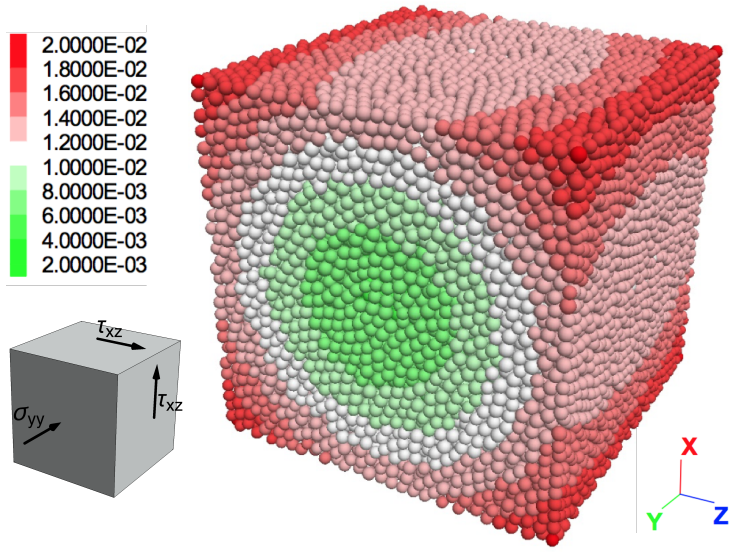

Figure 49. MRV assembly compressed in the y direction and sheared in xz. Elements are color-coded by the magnitude of element displacement in units of the mean element radius $\bar{R}$.

The stress-strain curves in Figure 50 generally follow a linear trend, except for a very small region at the beginning of the simulation. Final strains were at least two orders of magnitude larger in the directions of specified deformations relative to the unstrained directions.

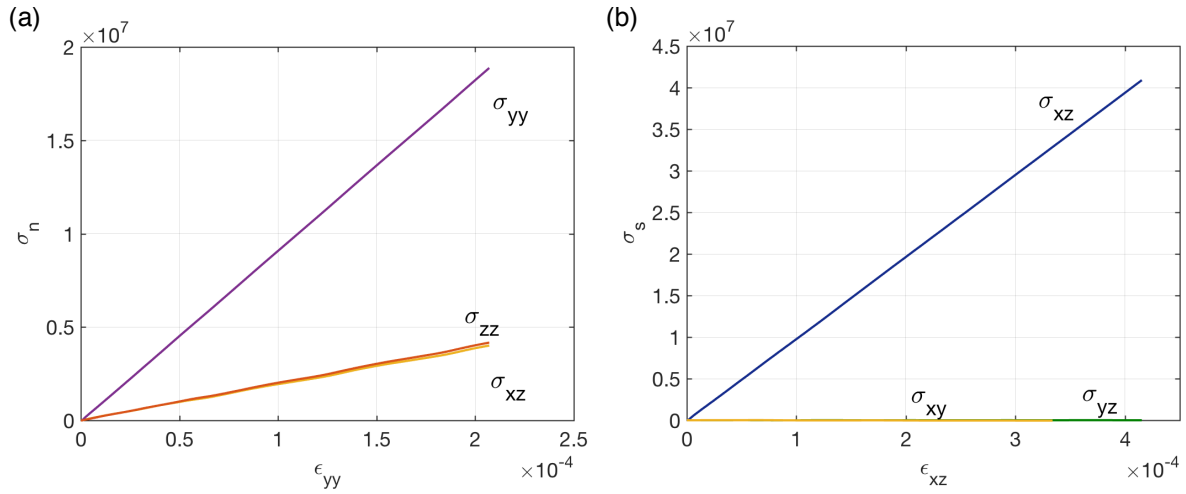

Figure 50. Stresses-strain curves in the deformation directions, (a) normal and (b) shear, and the corresponding elastic constants. Stress-strain curves are linear besides in the initial part of the simulation.

2.2.5.3.9. Full Stiffness Tensor

The full stiffness tensor was obtained for a representative case of anisotropy parameters, the same as the one used for the MRV. The full stiffness tensor the DEM assembly was measured to be:

$$C_{ij} = \begin{pmatrix} 75.5 & 30.4 & 30.4 & 0.05 & -0.3 & 0.4 \\ 30.4 & 76.3 & 30.9 & 0.2 & 0.05 & 0.2 \\ 30.4 & 30.9 & 76.1 & 0.2 & 0.05 & 0 \\ 0.05 & 0.2 & 0.2 & 28.7 & 0 & 0.05 \\ -0.3 & 0.05 & 0.05 & 0 & 28.5 & 0.05 \\ 0.4 & 0.2 & 0 & 0.05 & 0.05 & 28.6 \end{pmatrix} GPa \quad \text{Equation 49}$$

Averaging the cubically equivalent so stiffness element, and setting to zero those that would be zero under cubic symmetry give the tensor:

$$C_{ij} = \begin{pmatrix} 76.0 & 30.6 & 30.6 & 0 & 0 & 0 \\ 30.6 & 76.0 & 30.6 & 0 & 0 & 0 \\ 30.6 & 30.6 & 76.0 & 0 & 0 & 0 \\ 0 & 0 & 0 & 28.6 & 0 & 0 \\ 0 & 0 & 0 & 0 & 28.6 & 0 \\ 0 & 0 & 0 & 0 & 0 & 28.6 \end{pmatrix} GPa \quad \text{Equation 50}$$

Here $\bar{C}_{11} = \frac{(C_{11}+C_{22}+C_{33})}{3}$, $\bar{C}_{12} = \frac{(C_{12}+C_{13}+C_{23})}{3}$, and $\bar{C}_{44} = \frac{(C_{44}+C_{55}+C_{66})}{3}$. The variations in stiffness of the cubically equivalent element, including the ones that would be zero, provides a method for quantifying uncertainty. The largest uncertainty in this set of stiffness elements is in C_{11} and C_{12} values and measures 0.3 GPa. The C_{44} uncertainty is 0.1 GPa whereas the mean magnitude of terms that should otherwise be zero measures 0.15 GPa. These uncertainties are below detection in typical mechanical deformation experiments. The symmetry and cubic nature of the tensor presented in Equation 49 - Equation 50 implies that to use the proposed approach only two deformations are needed to describe a cubic material in the model.

2.2.5.3.10. Rotational Invariance of the Stiffness Tensor

The same model discussed in Section 3.3.8 was used to assess the rotational invariance of the elastic properties. The rotation matrix applied to obtain the rotated stiffness tensor is presented in Equation 51:

$$\mathbf{R} = \begin{pmatrix} -0.3062 & -0.9186 & 0.2500 \\ 0.8839 & -0.1768 & 0.4330 \\ -0.3536 & 0.3536 & 0.8660 \end{pmatrix} \quad \text{Equation 51}$$

which corresponds to angles of 60°, 30°, and 45° about the x, y, and z axes, respectively. Rotating the stiffness tensor Equation 49 with this transformation matrix gives the tensor:

$$C_{ij} = \begin{pmatrix} 80.3 & 29.2 & 27.7 & 0.5 & -3.0 & 1.3 \\ 29.2 & 79.2 & 28.8 & 1.9 & 1.1 & -2.6 \\ 27.7 & 28.8 & 80.7 & -2.4 & 1.9 & 1.2 \\ 0.5 & 1.9 & -2.4 & 26.8 & 1.2 & 1.1 \\ -3.0 & 1.1 & 1.9 & 1.2 & 25.7 & 0.5 \\ 1.3 & -2.6 & 1.2 & 1.1 & 0.5 & 27.2 \end{pmatrix} GPa \qquad \text{Equation 52}$$

This tensor represents the stiffness tensor if the principle axis of the stiffness distributions instead of being aligned with the Cartesian axis were rotated by $\boldsymbol{R}^{-1}$. We can therefore verify that the elastic behavior is rotationally invariant by assigning the stiffnesses to the assembly from the spheroid distributions rotated by $\boldsymbol{R}^{-1}$ and then computing the DEM stiffness tensor. The result is:

$$C_{ij} = \begin{pmatrix} 80.2 & 29.2 & 27.5 & 0.7 & -3.4 & 1.8 \\ 29.2 & 79.4 & 29.1 & 2.3 & 0.7 & -2.4 \\ 27.5 & 29.1 & 81.2 & -2.2 & 2.0 & 1.4 \\ 0.7 & 2.3 & -2.2 & 26.9 & 1.2 & 1.2 \\ -3.4 & 1.0 & 2.0 & 1.2 & 25.7 & 0.5 \\ 1.8 & -2.4 & 1.2 & 1.2 & 0.5 & 27.2 \end{pmatrix} GPa \qquad \text{Equation 53}$$

which is in good agreement with Equation 52 within the uncertainty established from Equation 49 and Equation 50. Rotating Equation 53 back and diagonalizing as in case of full stiffness tensor (Equation 50) yields:

$$C_{ij} = \begin{pmatrix} 75.9 & 30.8 & 30.8 & 0 & 0 & 0 \\ 30.8 & 75.9 & 30.8 & 0 & 0 & 0 \\ 30.8 & 30.8 & 75.9 & 0 & 0 & 0 \\ 0 & 0 & 0 & 28.8 & 0 & 0 \\ 0 & 0 & 0 & 0 & 28.8 & 0 \\ 0 & 0 & 0 & 0 & 0 & 28.8 \end{pmatrix} GPa \qquad \text{Equation 54}$$

with uncertainty in C_{11}, C_{12}, and C_{44} of 0.7, 0.7, and 0.1 GPa, respectively. The average value of the non-zero terms that should otherwise be zero is 0.2 GPa. The tensors in Equation 50 and Equation 54 agree to within 0.1, 0.2, and 0.2 GPa for C_{11}, C_{12}, and C_{44}, implying rotational invariance of the proposed anisotropy approach.

2.2.5.3.11. Reproducibility with Different Assemblies

To establish that the model's elastic behavior is robustly reproducible with different element assemblies the stiffness tensor calculations were repeated for two additional DEM samples

generated with different random seeds. These different element assemblies had the same average packing density and a similar total number of elements, (30,714 and 30,718 compared to original 30,700). For all three assemblies, the elastic response was obtained using two different sets of model parameters that yielded the elastic constants of C_{12}/C_{11}=0.3 and C_{44}/C_{11}=0.43. Results are shown in Table 9. The elastic constants are very close for the three different assemblies in case of both parameter sets indicating that the model is reproducible and can be readily applied to various DEM assemblies.

Table 9. Elastic response of DEM assemblies generated with different random seeds.

Parameter set	Value	Sample 1	Sample 2	Sample 3
Set 1	C_{12}/C_{11}	0.30	0.30	0.31
	C_{44}/C_{11}	0.43	0.44	0.44
Set 2	C_{12}/C_{11}	0.30	0.30	0.31
	C_{44}/C_{11}	0.42	0.42	0.42

2.2.5.3.12. Accessible Anisotropic Space

In order to determine the space of cubic elastic anisotropy that can be accessed by the DEM model, simulations were performed to compute a random cloud of elastic moduli for model parameters selected with a uniform random sampling of the normalized log space. The resulting data cloud showing the anisotropic space accessible by both the Z<1 and Z>1 models is shown in Figure 51. For reference, this accessible space is plotted alongside the literature reported moduli for a wide range of cubic materials (Simmons and Wang, 1971). The domain of the elasticity space that can be accessed here is a property of the granular model and is not expanded by extending the range of the model parameters sampled.

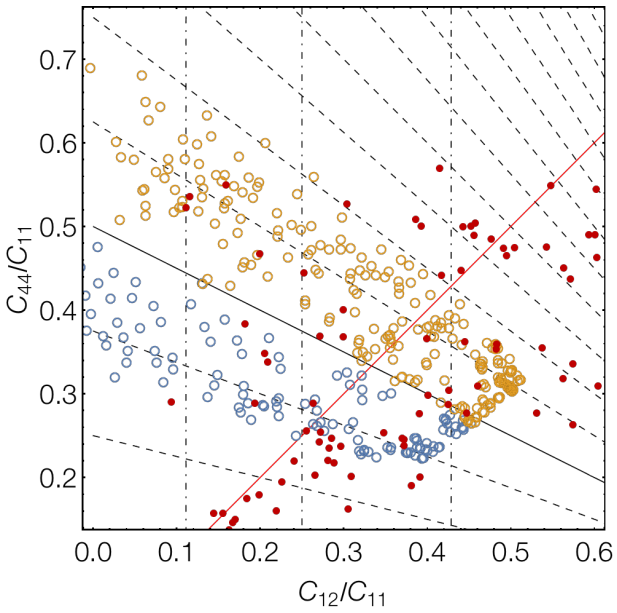

Figure 51. Comparison of elastic behavior with cubic materials. Red dots show literature reported elastic constants for a variety of cubic metals, ceramics, and oxides (Simmons and Wang, 1971). The open circles show the elastic moduli obtained with the DEM model from a random sampling of the α_n, α_s, and α_k normalized log space. In this plot, the vertical dot-dashed grid lines are contours of constant Poisson ratio in the ⟨100⟩ direction, $C_{12}/(C_{11}+C_{12})$ in steps of 0.1. The dashed black lines emanating radially from the bottom right are contours of constant Zener ratio (in steps of 0.25), with the solid line showing the contour for Zener ratio =1, and thus isotropic behavior. The red line cutting from bottom left to top right is the line along which the Cauchy symmetry relation, $C_{12}=C_{44}$, holds true.

2.2.5.3.13. Obtaining Specific Model Parameters

Because the space of model input parameters is three dimensional while the space of the resulting model's normalized elastic moduli is two dimensional, many different model parameters sets can lead to the same anisotropic elastic behavior. To elucidate the mapping from model parameters to emergent elastic moduli (and to enable efficient determination of model parameters for a desired elasticity) interpolation schemes have been developed based on an artificial neural network (ANN). Feed forward ANNs with a two hidden layers of nine neurons

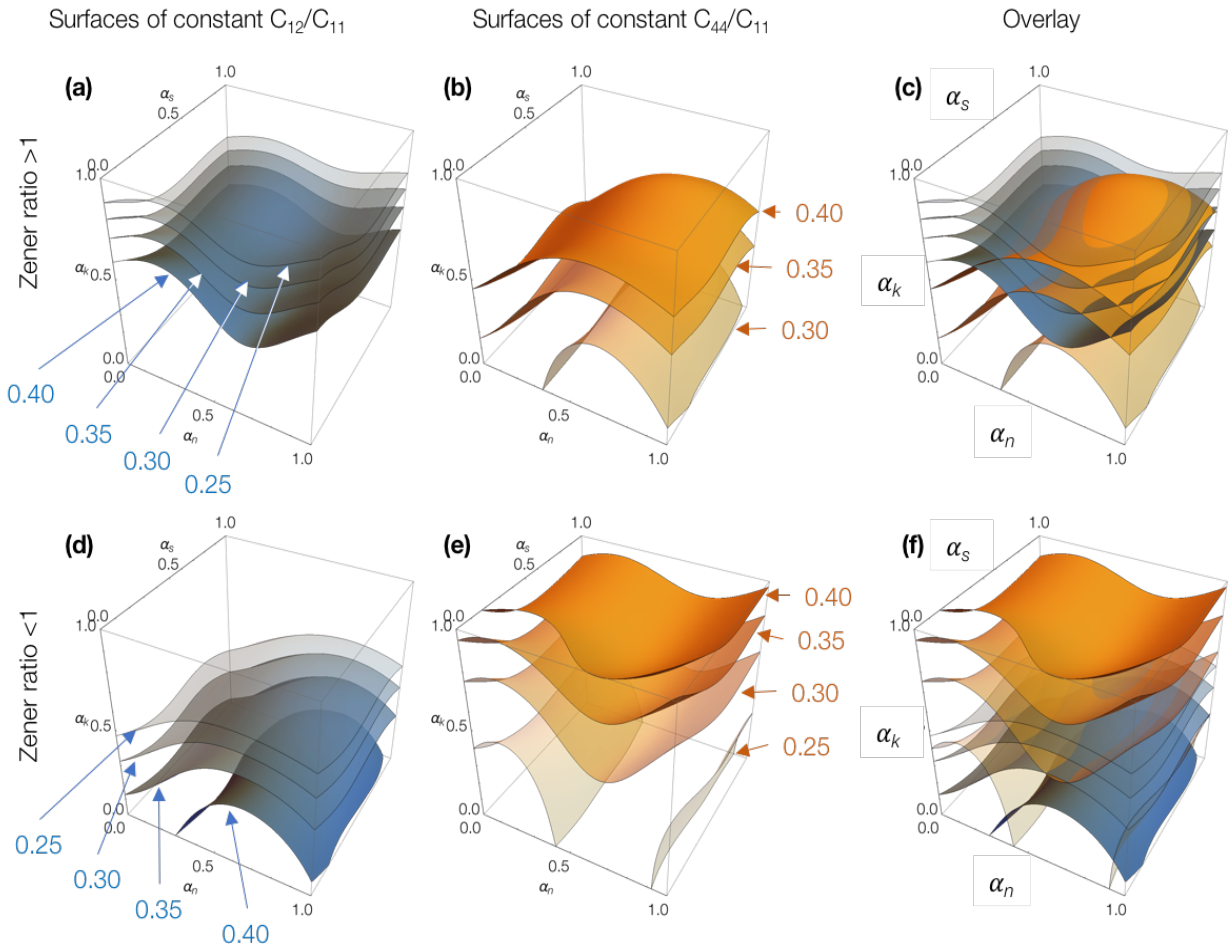

Figure 52. Surfaces of constant elastic moduli plotted in the space of log-normalized model parameters with the x,y, and z axes the normal, shear, and stiffness ratios respectively. Blue surfaces (plots (a) and (d)) are contours of C_{12}/C_{11} ratio. Orange surfaces (plots (b) and (e)) are contours of C_{44}/C_{11}. The top row (plots (a–c)) are for the Zener ratio >1 model, while the bottom row is for the Zener ratio < 1 model. Plots (c) and (f) show the two moduli contours overlaid.

each were trained to a randomly selected set of 70% of the log normalized model parameters used to compute moduli plotted in Figure 52. For both the Z<1 and the Z>1 models twenty ANNs were trained starting from different initial conditions, and the variance between the ANNs used to test the quality of training and uncertainty in the interpolation. The trained ANNs reproduced a validation dataset (half of the remaining data selected at random) with an R-squared value better than 0.997 — as well as should be expected for the uncertainty in the

computed elastic moduli. Using these ANN to explore the model parameter space in Figure 52 & Figure 53 shows contour surfaces in the log-normalized parameter space that have constant elastic moduli — Figure 52 shows isosurfaces of dimensionless C_{12} and C_{44}, while Figure 53 shows isosurfaces of Zener ratio and constant Poisson ratio along ⟨100⟩, defined as $C_{12}/(C_{11}+C_{12})$. These plots show that for any desired elastic response there are a range of possible model parameters that could reproduce it. The question of which alternative a user should choose will be discussed in more detail.

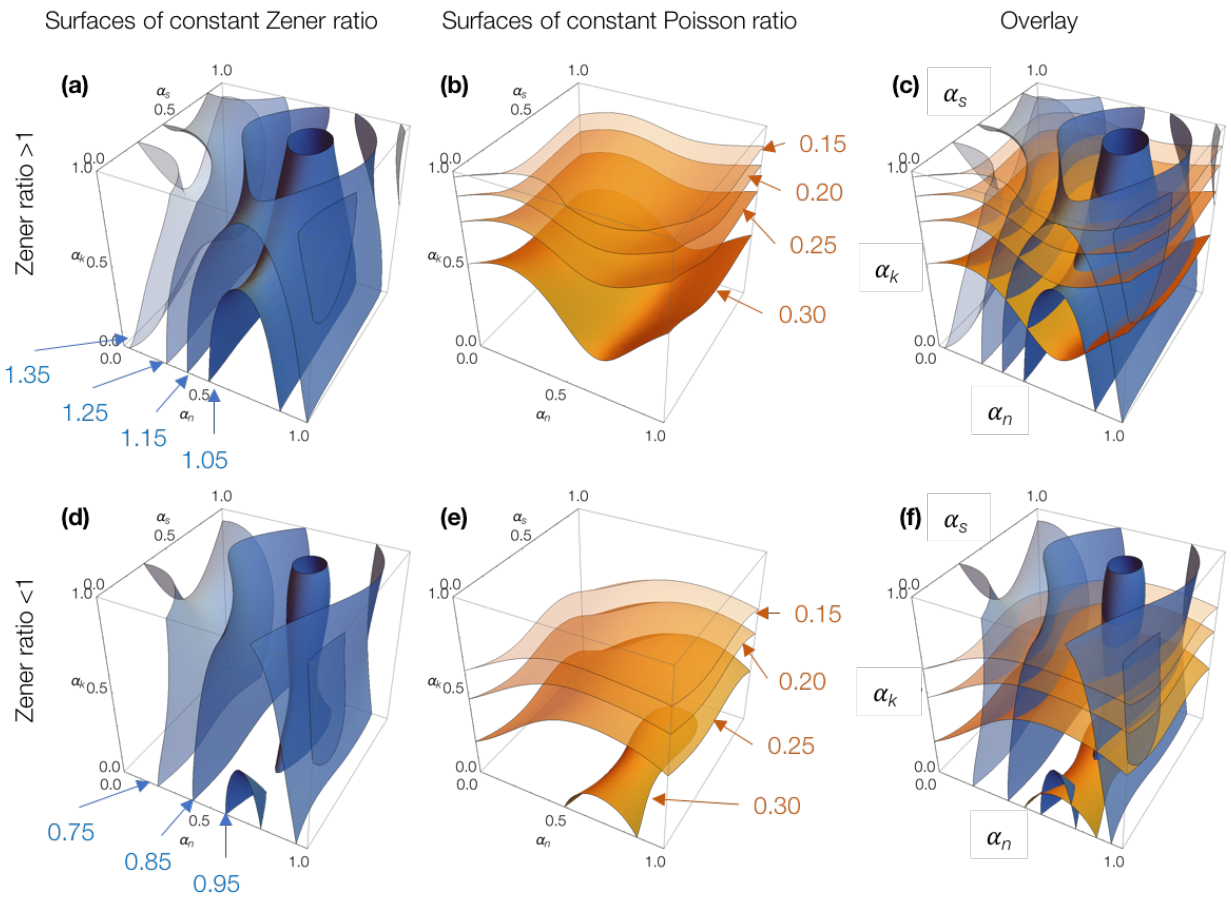

Figure 53. Surfaces of constant Poisson ratio plotted in the space of log-normalized model parameters with the x,y, and z axes the normal, shear, and stiffness ratios respectively. Blue surfaces (plots (a) and (d)) are contours of constant Zener ratio $2C_{44}/(C_{11}-C_{12})$ ratio. Orange surfaces (plots (b) and (e)) are contours of constant ⟨100⟩ Poisson ratio defined as $C_{12}/(C_{11}+C_{12})$. The top row (plots (a–c)) are for the Zener ratio >1 model, while the bottom row is for the Zener ratio < 1 model. Plots (c) and (f) show the two moduli contours overlaid.

2.2.5.3.14. Limits of the Accessible Domain of Elastic Properties

It is clear from the data cloud plotted in Figure 51 that there is only a limited domain of the elasticity space that can be accessed by the DEM models, and there are many known cubic materials possessing elastic constants that fall outside this domain. It is thus worthwhile to consider what sets the fundamental limits of the DEM model, and what this tells us more generally about the nature of atomic bonding. The domain of accessible moduli can be roughly

described as having Zener ratios between 0.65 and 1.5 with $C_{44} > 0.6\ C_{12}$. The surfaces of constant modulus in Figure 52 show that in both the Zener ratio >1 and the Zener ratio < 1 models the strongest influence on elastic properties is the change in the ratio of shear to normal stiffness, a_k, with C_{12} diminishing and C_{44} increasing as a_k is increased. In the Zener ratio <1 model the isosurfaces for C_{12} (C_{44}) are concave up (down) with varying anisotropy of the normal stiffness distribution. These surfaces have a valley in the log normalized parameter space running along $\alpha_n \approx 0.7$. This corresponds to a normal stiffness anisotropy ratio of $a_n = 1$, the condition of no directional dependence in bonds' normal stiffness. In the Zener ratio >1 model the directions of curvature of the C_{12} and C_{44} isosurfaces are reversed. The parameter that has the weakest impact on the models' elastic moduli is α_s, the anisotropy ratio of the shear stiffness, which is perhaps not surprising as the input parameter space was restricted so that shear stiffness amplitudes were always softer that normal stiffnesses.

Rather than considering the normalized C_{12} and C_{44} moduli it is instructive to examine surfaces of constant Zener ratio and ⟨100⟩ Poisson ratio ν (the ratio of lateral contraction due to an elongation along a ⟨100⟩ direction and defined by $C_{12}/(C_{11}+C_{12})$) as is shown in Figure 53. The Poisson ratio is similar in behavior to C_{12} in Figure 52, being strongly dependent on a_k. The Poisson ratio increases quickly with diminishing shear stiffness when the stiffness ratio is just less than 1, but the speed of change slows once the shear stiffness is negligible in comparison to the normal stiffness. When the stiffness ratio is just less than 1 the DEM assemblies exhibit ν close to zero (that is, there is no coupling between deformations in orthogonal directions), and for shear stiffnesses larger than the normal stiffnesses the DEM assemblies become auxetic. This unusual behavior can be understood by considering the deformation of an idealized case of four identical elements connected by parallel bonds at 45° to a loading axis (see Figure 54). It is trivial to show that the Poisson ratio of this idealized element cluster is

$$\nu = \frac{-\Delta_y}{\Delta_x} = \frac{k_n - k_s}{k_n + k_s} \qquad \text{Equation 55}$$

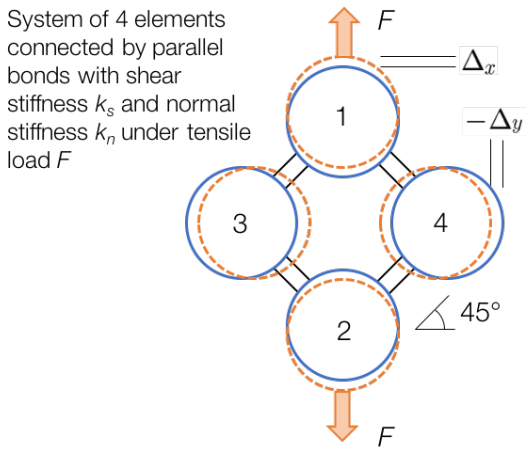

Figure 54. Idealized 4 element model to illustrate the effect of normal to shear stiffness ratio on the Poisson contraction.

Clearly if this simple model were rotated by 45° so that the bonds were parallel or perpendicular to the loading the Poisson contraction of the assembly would be zero, and so with a large random assembly the collective behavior will fall between these extremes.

The simple example in Figure 54 shows that Poisson contraction of the DEM assembly originates from the balance of shear and normal deformations of the bonds. The contraction does not originate from geometric rotation of bonds acting like network of pinned bars in a complex truss — a good thing as the atomic bonding in a material are not simple pair interactions. However, the Poisson contraction is still a collective property and does not stem from Poisson contraction of individual elements. Each element represents a chunk of elastic material seamlessly welded to its neighboring elements, and so each element should experience a Poisson contraction. This is not captured in standard DEM models which treat elements as rigid and represent their elastic behavior with independent contact laws. Correctly capturing Poisson coupling in this formalism would require the equilibrium length of a bond between two elements to alter based on the combined state of all the other bonds those elements participate in. This is a fundamental limitation of the current parallel bond DEM that we will seek to remedy in future work, and unfortunately, may require losing the simplicity of independent local contact laws. It is clear from Figure 51–Figure 53 that the DEM networks simulated in this work have trouble producing a Poisson ratio greater than about 0.3. It was found that this limit could be increased by changing the density of the bonding network to reduce the average element coordination, but a thorough investigation of this is beyond the scope of this report.

Also shown in Figure 53 are surfaces in parameter space with constant Zener ratio. It can be seen that these lie vertically and so are only weakly coupled to the stiffness ratio, a_k. The anisotropy increases as a_n or a_s move away from 1 (α_n or α_s move away from 0.703), and dependence on a_s fades as a_k diminishes. The limit to the elastic anisotropy achievable with the DEM model can be understood by looking at the plots of the directionally dependent stiffness shown in Figure 46 (and also later in Figure 55). As the shear or normal anisotropy parameter becomes large or small the corresponding stiffness distribution becomes very acute, either composed on needle like lobes or pancake like discs. In these extreme cases, the solid angle subtended by the directions of high stiffness is very low and, as the elements have an average coordination of eight, the likelihood of a contact lying exactly along the stiff direction becomes low. This means that although the bond stiffnesses are highly anisotropic, there are a number of very stiff bonds embedded in a network of much softer bonds and thus one would expect to require a large MRV.

Beyond the problem of numerically sampling a stiffness distribution with long tails, a second and more fundamental limit on the accessible elastic properties is set by the integral of the stiffness functions. In Appendix C, the analytic model derived in Appendix A is compared with the DEM simulations. Performing a random sampling of the parameter space, as was performed for DEM in Figure 51, produces a very similar accessible domain of elasticity as that shown in Figure C.1. The analytic model and DEM simulations display elastic anisotropy ranging from 0.6 to 1.5. Where the models differ is in their ability to cross the red $C_{12}=C_{44}$ line.

In Appendix D, the analytic model is used to determine how the limits of the accessible elastic domain are related to the angular stiffness functions. For expanding this domain to reach more extreme anisotropies, it is shown that larger values of Z can be achieved if the stiffness functions are altered to permit independent tuning of shear and normal stiffness along the ⟨110⟩ directions. To test this a set of modified stiffness functions was defined that added or subtracted a stiffness

contribution due to a function defined as the envelope of six spheroids aligned along ⟨110⟩. For the Z>1 model these new stiffness functions were defined with the normal stiffness $k_n(\boldsymbol{n}, a_n) = k_o\left(r_{\langle 111\rangle}(\boldsymbol{n}, a_n) + 0.5r_{\langle 110\rangle}(\boldsymbol{n}, a_n)\right)$, and shear stiffness $k_s(\boldsymbol{n}, a_s) = k_o\left(r_{\langle 100\rangle}(\boldsymbol{n}, a_s) - 0.5r_{\langle 110\rangle}(\boldsymbol{n}, a_s)\right)$, where $r_{\langle 100\rangle}$, $r_{\langle 111\rangle}$, and $r_{\langle 110\rangle}$ are radial functions describing the envelope of three, four, and six overlapping spheroids aligned with the principal axes along the $\langle 100\rangle$, $\langle 111\rangle$, and $\langle 110\rangle$ directions, respectively. For the Z<1 model the stiffness functions were $k_n(\boldsymbol{n}, a_n) = k_o\left(r_{\langle 100\rangle}(\boldsymbol{n}, a_n) + 0.5r_{\langle 110\rangle}(\boldsymbol{n}, a_n)\right)$, and $k_s(\boldsymbol{n}, a_s) = k_o\left(r_{\langle 111\rangle}(\boldsymbol{n}, a_s) - 0.5r_{\langle 110\rangle}(\boldsymbol{n}, a_s)\right)$. The domain of elasticity that can be accessed using these functions is also plotted in Figure C.1(a) and is considerably wider in Z that the simpler model, but is still bounded by the C_{12}=C_{44} line.

To examine the cause of the C_{12}=C_{44} boundary, Appendix D also examines the integral that dictates the quantity $C_{12} - C_{44}$. This was found to be always negative; there is no modification that could make this positive. That is, a system of parallel bonds deformed homogeneously cannot have $C_{12} - C_{44} > 0$. This then raises a question: what is different about the DEM simulations that enables $C_{12} - C_{44}$ to be positive in some circumstances? In the analytic model, it is seen that $C_{12} - C_{44}$ becomes identically zero when the shear stiffness goes to zero in agreement with the Cauchy relationship that $C_{12} = C_{44}$ in materials held together with center to center pair interactions only. That the DEM simulations are able break through this we attribute to non-homogeneous displacement of the elements. In the DEM simulations the orientation and stiffness of bonds is random, and thus the deformation field of the elements will include locally non-affine displacements. The result will be a larger fraction of elastic energy stored in bonds oriented in soft directions and deformation fields that could involve local rotation of clusters of elements. The authors speculate that these could be responsible positive values of $C_{12} - C_{44}$.

A more systematic approach to expanding the accessible elastic domain would be through the use of stiffness functions constructed from a more complete basis set. For example, one could define a stiffness distribution using a correctly symmetrized set of spherical harmonics. For more flexibility still, one could define the shear stiffness to depend on the direction of displacement in addition to the orientation of the bond. The standard parallel bond model used in DEM has only a single shear stiffness; that is, for a given contact normal, the shear stiffness is the same in all directions perpendicular to the contact. This is not the case in a cubically elastic medium where, as can be seen in Figure 44, on any contact plane there will be a soft and stiff direction of shear.

2.2.5.3.15. Selection of Element Packing Density, Coordination, and Polydispersity

The choice of assembly packing fraction, element polydispersity, and coordination number all affect the collective macroscopic elastic behavior but were not fully explored in this work. Rather, a set of reasonable choices for these parameters were found for which the sensitivity of the model to the variation in packing, element size distribution and element coordination was low.

The packing efficiency is quantified here by the assembly porosity, or *void fraction*, as is common in the geotechnical literature for granular materials. A lower limit of an admissible void fraction is 0.36 which corresponds to a closest possible packing of monodispersed spheres. Smaller void fractions can be obtained in highly polydisperse assemblies, but in this work the element size distribution was relatively low — only large enough to prevent regular crystal-like

packing of elements. An upper limit of void fraction occurs at around 0.44 with the jamming transition in a non-bonded assembly, above which the assemblies become so loose that they are mechanically unstable. Although the elements in the assemblies in this work are bonded, the bonding network with a high void fraction would be very loose and thus a poor representation of an elastic continuum. The interaction cutoff for bonding adjacent elements was tuned so that the average element coordination was 8.0. In general, a higher coordination number may give macroscopic response closer to continuum behavior; however, more redundant bonding in and assembly inhibits Poisson contraction and so a compromise was needed reach higher Poisson ratios and C_{12} values relative to C_{11} and C_{44}.

2.2.5.3.16. Choosing Optimal Model Parameters

The most surprising result from Figure 53 is that it does not matter how one chooses to introduce anisotropy into the directional dependence of the bond stiffnesses. One can create a DEM model with the same macroscopic Zener anisotropy ratio using stiffness distributions defined by either oblate ($a < 1$) or prolate ($a > 1$) spheroids, providing one imposes the correct cubic symmetry of these distributions. The concept is particularly noticeable in Figure 55 which shows the locus of parameters that all yield a particular elasticity tensor, along with spherical plots of the stiffness distributions that produced them. The contours show a remarkable mirror symmetry in the $a_s = 1$ plane ($\alpha_s = 0.703$ plane). For both the Zener ratio <1 and >1 models the angular functions for normal stiffness that produce the left-hand contour are built from prolate spheroids. These distributions resemble the angularly dependent normal stiffness in Figure 44, while the right-hand contour is constructed using oblate distributions of normal stiffness that appear to have little in common with the moduli in Figure 44.

At this point, some questions arise. Which of the many choices of parameters for a desired elastic response should one choose? And, how can one discriminate between the choices? and should one switch from angular functions based on spheroids to a basis set that provides more flexibility such as spherical harmonics?

Sticking with spheroid angular functions, a number of arguments can be made to steer the choice of model parameters. One approach is to choose parameters that reflect the underlying behavior of the material of interest. With this rationale, one might choose parameters in which the same anisotropy ratio is used for shear stiffnesses as for normal stiffness — restricting oneself to parameters on the diagonal $a_n = a_s$ plane as plotted in Figure 56. On this equianisotropy plane one still has to decide whether to use oblate ($a < 1$) or prolate ($a > 1$) distributions. Keeping with the philosophy of mimicking the bonding behavior of the material the best choice might be to use parameters with $a > 1$.

An alternative approach to choosing between model parameters that produce equivalent macroscopic elastic response is to ask what is different about the system at the microscopic level, and to choose the system with the least microscopic heterogeneity, and thus, the smallest MRV. With this rationale, one would choose the parameters for a_n and a_s closest to one – and when faced with the choice of prolate or oblate distributions, opting for oblate distributions would be preferable as these have a more equitable distribution of stiffness over a given solid angle. To quantify heterogeneity, we compute the mean normalized standard deviation of the distribution of local strains obtained from the set of measurement spheres. This noise metric for the eight sets of model parameters (labeled i–viii) along the contour in Figure 55(a) are given in Table 10. For this system which, is not strongly anisotropic, the distribution of local strains is narrow with a

width of around 5-6%, for both the normal and shear components of strain. There is no obvious trend in this heterogeneity with the model parameters, other than that the noise in the normal strain is slightly larger than the noise in the shear strain.

An alternative means to quantify this internal state of the DEM assembly can be made indirectly by comparing the elastic moduli of the DEM element assembly to the moduli of the analytic model with the same stiffness functions. This comparison was also performed for parameter sets indicated in Figure 55(a) with the results reported in Table 10. In these cases the mean field analytic model and the DEM simulations are in good agreement and there is no overall trend in the deviation. The comparison was also performed over the entire log normalized parameter domain for the $Z > 1$ model as shown in Figure C.1(b) in Appendix C. Here the assumption is that differences between the mean field analytic model and the DEM model arise because of heterogeneous deformation and therefore, the deviation in moduli between the two is a metric of the heterogeneity in the DEM assembly. In Figure C.1(b) it can be seen that the deviation from mean field behavior depends most strongly on the ratio of the shear to normal stiffness, and that C_{12} matches the mean field model when the normal and shear stiffnesses have similar magnitudes, while C_{44} matches the mean field model when the shear stiffness is low.

As a final comment, the rationale for selecting the parameters for spheroid-based models can be applied to choosing other angular functions and selecting the model parameters for these alternative functions. The advantage to be gained from selecting more flexible angular functions, besides reducing the MRV, is expanding the boundaries of accessible elastic behavior.

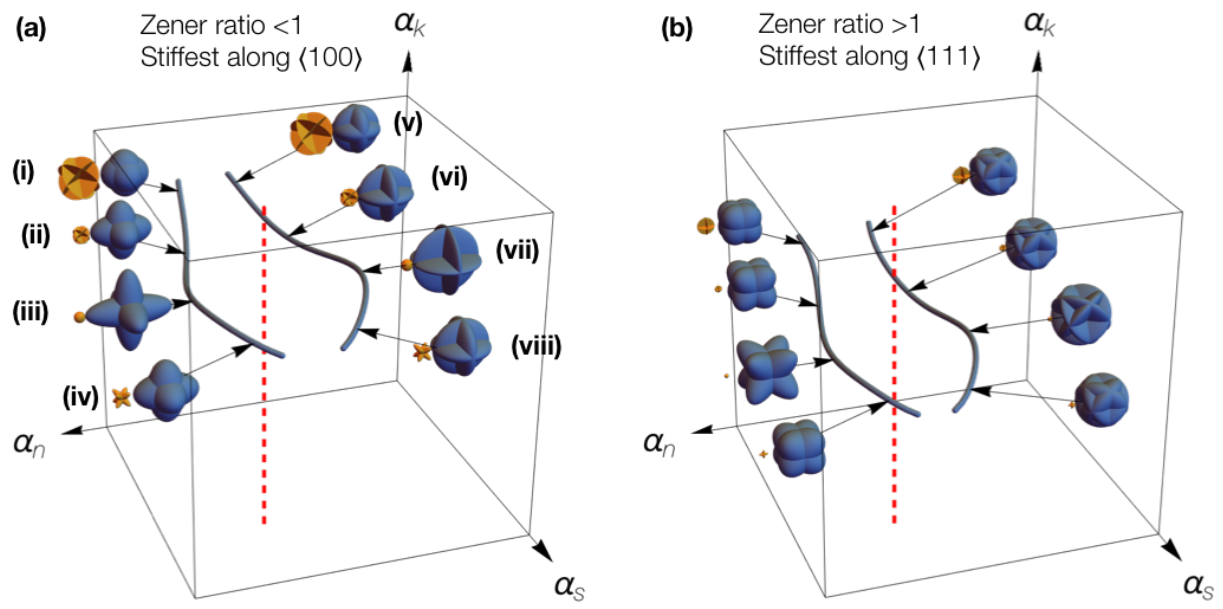

Figure 55. Contours of identical elastic behavior. Plot (a) shows contours of C_{12}/C_{11}= 0.2, and C_{44}/C_{11}= 0.35 for the Zener ratio <1 model. Plot (b) shows contours of C_{12}/C_{11}= 0.35, and C_{44}/C_{11}= 0.35 for the Zener ratio >1 model. The vertical dashed red line indicates the line along which the bond normal and shear stiffnesses are isotropic. The inset polar plots show the shear (gold) and normal (blue) stiffness distributions (all plotted on the same absolute scale).

Table 10. Table quantifying variation in internals state for DEM parameters shown in Figure 55.(a) which all have the same normalized elastic moduli of C_{12}/C_{11} = 0.2 and C_{44}/C_{11} = 0.35. The 2nd and 3rd columns show the mean normalized noise in measurement sphere normal and shear strains, and the last two columns quantify the deviation from the analytic model derived in Appendix A.

Model Parameters				**Normalized measurement sphere noise (%)**		**Deviation from analytic model:** $(C_{ij}/C_{11})_{DEM} - (C_{ij}/C_{11})_{Model}$	
Set	a_n	a_s	a_k	ε_1 (%)	ε_4 (%)	Deviation: Δ_{12}	Deviation: Δ_{44}
i	1.30	0.03	0.33	5.8	5.0	-0.028	0.017
ii	1.82	0.12	0.22	5.7	4.8	-0.013	0.003
iii	2.83	0.88	0.24	6.1	4.3	-0.008	-0.015
iv	1.78	3.61	0.22	5.4	4.3	-0.014	0.006
v	0.50	0.03	0.34	5.8	5.1	-0.025	0.014
vi	0.34	0.12	0.23	5.5	5.0	-0.012	0.006
vii	0.21	0.88	0.27	5.8	4.5	-0.007	-0.002
viii	0.38	3.61	0.22	5.4	4.5	-0.005	0.009

2.2.5.3.17. Summary of Elastic Anisotropy

In this work, the discrete element method (DEM) was adapted to enable a random packing of elements to model materials with cubic anisotropy. The ability to capture cubic elasticity is a prerequisite for extending the discrete element method to model stochastic mechanical processes in monolithic solids which consist of cubically anisotropic elastic constituents (polycrystals, composites, etc.). Additionally, the DEM model presented here provides a roadmap for adapting traditional DEM to model orthotropic rocks and geotechnical materials. This extension to DEM was accomplished using the established parallel bond contact formalism and is capable of modeling a broad range of cubic materials with Zener ratios smaller and larger than one. Anisotropy in the collective elastic response of the DEM assembly comes from assigning the stiffness of element to element bonds depending on the bonds' initial orientation — and crucially, assigning them using an angular dependence function that has the same underlying cubic symmetry as the crystal it mimics. In this first demonstrative work, these angular functions where defined by the envelope of three or four overlaid spheroids with principal axes aligned, respectively, along the ⟨100⟩ or ⟨111⟩ directions of the crystal being represented. The models have three parameters that define the overall elastic behavior (a_n, a_s, and a_k, respectively, the normal and shear stiffness anisotropy, and the ratio of the shear to normal stiffness magnitude). A fourth parameter sets the overall magnitude of the resulting stiffness tensor. Two different models were presented to capture the properties of materials with Zener ratio <1 and Zener ratio >1. It was demonstrated that the models' elastic behaviors have the correct symmetry and rotational invariance.

The research presented here also explored the mapping between the model parameters and the resulting elastic properties and examined the limits on domain of elastic properties that can be accessed with the DEM model. An artificial neural network (ANN) was trained to interpolate between input DEM model parameters and the ensuing elastic moduli of the DEM assembly. The interpolation scheme enabled connections between the model parameters and resulting behavior to be elucidated efficiently and revealed the surprising result that only the scale of the asymmetry aspect ratio in the contact mechanics is important, not its direction of deviation. The ANN analysis further revealed that the input parameters are non-unique and thus a desired set of elastic

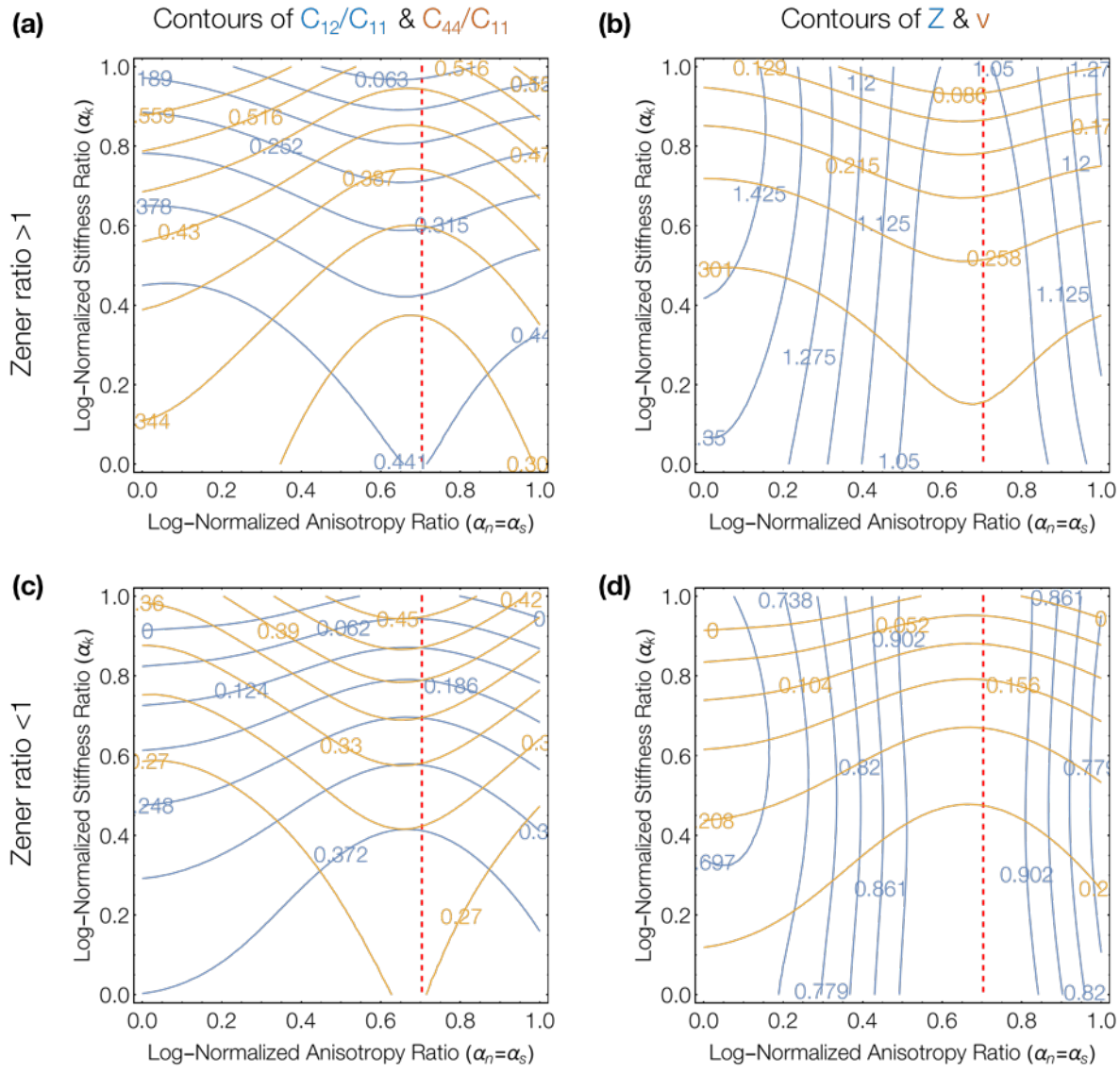

Figure 56. Contours of elastic moduli on the plane of the parameter space on which the normal and shear stiffnesses have identical anisotropy ratio ($\alpha_n=\alpha_s$). The red dashed line marks the parameters at which the normal and shear stiffnesses are isotropic ($a_n=a_s=1$). Plots (a & b) are for the Zener ratio >1 model and (c & d) are for Zener ratio <1. Plots (a & c) show the normalized moduli C_{12}/C_{11} (blue) and C_{44}/C_{11} (gold). Plots (b & d) show the Zener ratio (blue) and Poisson ratio (gold).

stiffness tensor ratios can be achieved with numerous combinations of input parameters. Accompanying the DEM model, an analytic mean field model of the DEM elasticity was presented and used to examine the limit on the accessible domain of elastic properties. This model reveals that the accessible domain can be expanded to larger and smaller Zener anisotropy ratios by changing the functional form of the angular stiffness functions, but that there is a hard limit to increasing the Poisson ratio that is set by the Cauchy C_{12}=C_{44} limit. The combination of the ANN and the mean field model can be used to quickly and efficiently choose an optimal set of DEM model parameters to represent a system with a specific desired stiffness tensor.

2.2.6. *Isotropic plasticity without hardening*

2.2.6.1. Plastic deformation in DEM

The DEM model of isotropic non-hardening plasticity relies on the framework outlined in Section 2.2.1. In traditional DEM simulations of bonded assemblies such as rock, plasticity is modeled through permanent breakage of parallel bonds. The resulting stress-strain response is a brittle failure as shown in Figure 57. The bonds break when their tensile or shear stresses exceed their tensile, σ_C, or shear strength, τ_C. The tensile $\bar{\sigma}$ and shear $\bar{\tau}$ stresses on the bond are expressed as,

$$\bar{\sigma} = \frac{\left\|\bar{\mathbf{F}}_{\mathbf{n}}\right\|}{\bar{A}} + \frac{\left\|\bar{\mathbf{M}}_{\mathbf{b}}\right\|}{I}\bar{R} \qquad \text{Equation 56}$$

$$\bar{\tau} = \frac{\left\|\bar{\mathbf{F}}_{\mathbf{s}}\right\|}{\bar{A}} + \frac{\left\|\bar{\mathbf{M}}_{\mathbf{t}}\right\|}{J} \qquad \text{Equation 57}$$

Here $\boldsymbol{F_n}$ and $\boldsymbol{F_s}$ are the bond normal and shear forces, $\boldsymbol{M_b}$ and $\boldsymbol{M_t}$ are the bending and twisting moments, $\bar{A} = \pi\bar{R}^2$ is the bond area, and $I = \frac{1}{4}\pi\bar{R}^4$ and $J = \frac{1}{2}\pi\bar{R}^4$ are the moment of inertia and the polar moment of inertia. Schematic display of each force and moments contribution to bond deformation is shown in Figure 58.

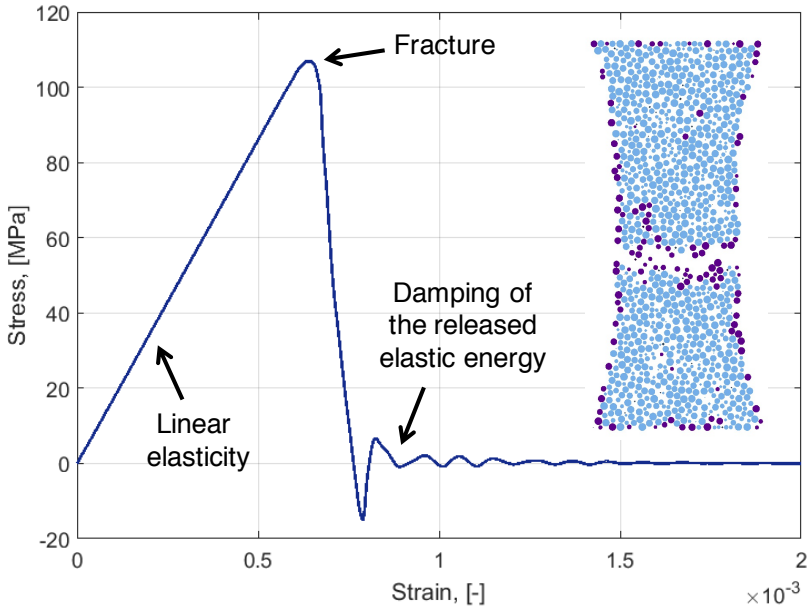

Figure 57. Brittle fracturing in a typical DEM simulation – stress-strain response and assembly cross-section. Dark colors represent elements with coordination number lower than 5.

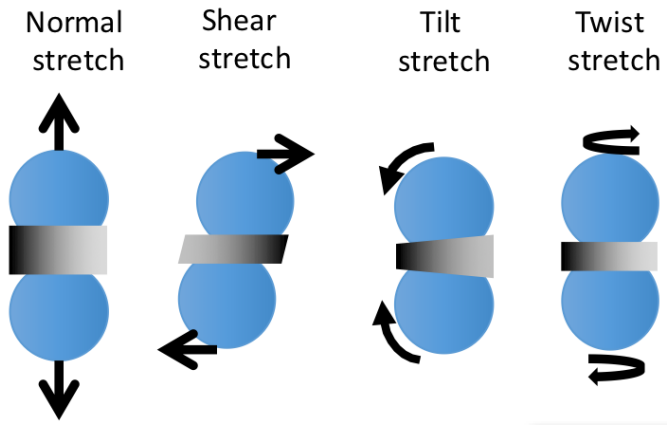

Figure 58. Basic deformation mechanisms contributing to parallel bond failure

To implement plasticity without hardening, the bonds are allowed to reform after breaking until their gap parameter becomes larger than the gap cutoff (Equation 8), at which point the bond will remain broken. Additionally, whenever a bond breaks, the assembly is scanned and new bonds are formed according to the gap cutoff criterion. With these modifications, the model introduces plastic deformation through a combination of two mechanisms: (1) elongation of bonds (i.e., free volume generation); and (2) promoting local sample deformation along high shear stress planes to facilitate shear banding. The contribution of these two mechanisms is influenced by the relative fraction of particular bond breaking modes – tensile and shear failure.

The bond strengths were defined by an expression derived to satisfy two criteria: (1) the bond breaks at least once before it reaches its final length and is excluded from the computation; and (2) the bond does not reach lengths significantly larger than the length determined by the gap cutoff parameter (Equation 8).

Neglecting the bending and twisting moment contributions, the normal and shear stresses, respectively (Equation 56-Equation 57), on the bond are proportional to the product of bond normal and shear stiffness and the displacement of one of the elements at time *i*, $\mathbf{u_i}$:

$$\bar{\sigma}_i = \frac{\left\|\bar{\mathbf{F}}_\mathbf{n}\right\|}{\bar{A}} + \frac{\left\|\bar{\mathbf{M}}_\mathbf{b}\right\|}{J} \approx \frac{\left\|\bar{\mathbf{F}}_\mathbf{n}\right\|}{\bar{A}} \approx \frac{\bar{A}k_n\left\|\mathbf{u}_i\right\|}{\bar{A}} = k_n\left\|\mathbf{u}_i\right\| \quad \text{Equation 58}$$

$$\bar{\tau}_i = \frac{\left\|\bar{\mathbf{F}}_\mathbf{s}\right\|}{\bar{A}} + \frac{\left\|\bar{\mathbf{M}}_\mathbf{t}\right\|}{J} \approx \frac{\left\|\bar{\mathbf{F}}_\mathbf{s}\right\|}{\bar{A}} \approx \frac{\bar{A}k_s\left\|\mathbf{u}_i\right\|}{\bar{A}} = k_s\left\|\mathbf{u}_i\right\| \quad \text{Equation 59}$$

Approximating the displacement as the gap cutoff parameter g_{max} yields

$$\tau_c = k_s g_{\max} \quad \text{Equation 60}$$

$$\sigma_c = k_n g_{\max} \quad \text{Equation 61}$$

The expression in Equation 61 holds exactly for a bond under pure tension with one of the elements being stationary. For other failure modes using Equation 60-Equation 61 leads to multiple bond failures before the final failure which is the desired behavior, for example, to simulate slip under shear. In practice, the strengths are corrected with additional factors, $\beta_n, \beta_s < 1.0$ that tune the macroscopic stress to target values:

$$\sigma_c = \beta_n k_n g_{\max}$$
$$\tau_c = \beta_s k_s g_{\max} \quad \text{Equation 62}$$

2.2.6.2. Assembly generation

Assembly was generated using the same steps as outlined in Section 2.2.4.2 except that the after removal of walls it was carved down to create a dog-bone shaped tensile sample (Figure 59). The sample was deformed by imposing the displacement of the elements on the outer circular faces of the sample, hereafter referred to as grip elements. Similar to physical tensile experiments, the dog-bone sample shape was used to prevent stress concentrations causing premature failure adjacent to the grip region of the sample. The dog-bone assembly shape was created by removing all elements with centers of mass that lie outside a volume defined as a cylindrical region and two hyperboloid shoulder regions.

Starting with a rectangular box with the origin at its corner, the sample shape was defined according the following conditions,

$$z = z_c - H_i, x = x_c - \frac{W}{2}, y = y_c - \frac{W}{2}$$
$$f_h = x^2 + y^2 - \left(\frac{z}{c}\right)^2 - 1$$

Equation 63

Element with a height $H_1 \leq z_c < H_2$ is included in the assembly if $f_s \leq 0$

$$z = z_c, x = x_c - \frac{W}{2}, y = y_c - \frac{W}{2}$$
$$f_h = x^2 + y^2 - \left(\frac{R_{cyl}}{2}\right)^2$$

Equation 64

H_i is either H_1 or H_2, x, y, z are transformed coordinates of the element centroid, x_c, y_c, z_c such that the assembly center coincides with the coordinate system origin, W is the width/side of the original box, R_{cyl} is the radius of the cylindrical section and $c = 2R_{cyl}$, a parameter that determines the size of the hyperbolic regions ($c = 2$ herein).

2.2.6.3. Model properties and implementation

The described model was used to simulate tensile testing of a DEM assembly. The grip elements (Figure 59a) were defined to have a fixed axial velocity (i.e., a constant displacement rate, $\dot{u}_z$) to stretch the assembly until failure. Lateral motion of the grip elements was unconstrained. The velocity of the grip elements was selected to give a dimensionless inertial number, defined as $I = \dot{\gamma}\overline{d}/\sqrt{P/\rho}$ where $\dot{\gamma}$ is the shear strain rate, $\overline{d}$ is mean element diameter, P is bulk stress, and ρ is assembly density, of approximately 10^{-4}. This value is an order of magnitude less than the threshold needed to maintain quasi-static conditions (da Cruz et al., 2005). During the simulations, the volume-averaged macroscopic stresses and strain rates in the sample were calculated using 500 spherical measurement volumes randomly located within the assembly. Each measurement volume encompassed approximately 130 elements. Average strains were obtained by integration of average strain rates.

The assembly used in this work is shown in Figure 59a while its properties are summarized in Table 11. The solid fraction of the assembly was $\Phi = 0.60$ while for comparison, $\Phi_{RCP} \cong 0.64$ for a random close packing of monodispersed spheres. Bond modulus and normal-to-shear stiffness ratio were calibrated to reproduce specimen-scale response consistent with a generic metallic material. This resulted in a material with an average Young's modulus of 169 GPa and Poisson's ratio of 0.23. Bond strength scaling factors β_n and β_s were set to produce yield stresses of approximately 200 MPa. Figure 59b shows distribution of normal bond stresses during the elastic part of the simulation. All of the mentioned parameters can be calibrated to give a desired yield stress and elastic modulus value, while Poisson's ratio is more restricted in this formulation. Such restricted Poisson's ratio also arises in other emerging mesoscopic methods for simulating continuum materials such as bond-based peridynamics (Kumar et al., 2016; Madenci and Oterkus, 2016a).

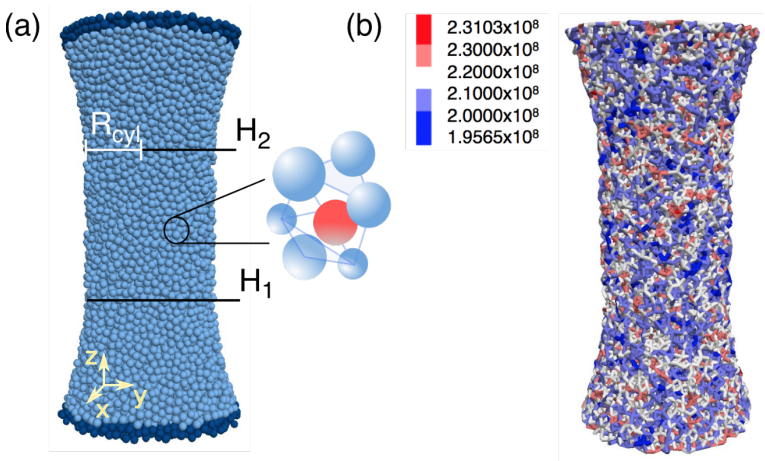

Figure 59. The DEM assembly: (a) showing grip elements (dark blue), components of sample generation, and local cage with blue elements being the neighbors (nodes) (b) bonds colored by their normal stress (units in Pa) at a point in the region of elastic deformation.

Table 11. Model properties

	Parameters	Value
Elements	Maximum relative element diameter $d_{max}/\bar{d}$	1.0833
	Minimum relative element diameter $d_{min}/\bar{d}$	0.9167
Bonds	Bond modulus, [Pa]	1.0595×10^{12}
	Normal-to-shear stiffness ratio, []	5.0
	β_n	0.02 - 0.06
	β_s	0.012 - 0.026
	Gap parameter, [m]	$0.08\bar{d}$
Assembly	Number of elements	15,512
	Number of parallel bonds	58,962
	Average coordination number	7.6
	Solid fraction Φ	0.6
	Relative height $H/\bar{d}$	50
	Relative radius of the cylindrical section $R_{cyl}/\bar{d}$	12.5
	Displacement rate, $\dot{u}_z$	$0.83\ \bar{d}/s$
	Young's modulus, [GPa]	169
	Poisson's ratio	0.23
	Yield stress, [MPa]	200

2.2.6.4.Deformation analysis

Two different metrics, called d_{2min} and local cage deformation herein, were used to assess the mechanisms of plastic deformation in the model. These metrics quantify local plasticity, thus enabling visualization of shear bands and other deformation localizations that deviate from the affine deformation of the sample.

The d_{2min} analysis compares the displacement of each element $\boldsymbol{u}$ with the expected continuum displacement at that point. The analysis does not rely on absolute values of the differences, but rather, on their relative deviations at a given time and any deviations from the mean. The continuum displacement was computed for a cylindrical sample of equivalent height and radius of the gauge length portion of the assembly. The continuum displacement field for a deformation along z can be defined as:

$$\mathbf{u}_{cn} = \begin{bmatrix} 0 & 0 & 1 \end{bmatrix} \frac{\left(z_c - \frac{L_0}{2} \right)}{\left(L_0 / 2 \right)} \delta \qquad \text{Equation 65}$$

where z_c is the z-component of the element position, L_0 is the initial height of the assembly, and δ is the total displacement, defined as $\delta = (L_{new} - L_0)/2$. The new height L_{new} is computed from the positions of the top and bottom grip elements as $L_{new}=z_{max} - z_{min}$ with $z_{max} = \max(z_{ci} + R_{bi})$ and $z_{min} = \min(z_{cj} + R_{bj})$. Here i and j correspond to the top and bottom grip elements, respectively. Computation of z_{min} assumes that since the assembly starts with its base at z=0.0, any tensile deformation will result in a negative z location. Finally, the d_{2min} metric is defined as $d_{2min} = \|\boldsymbol{u} - \boldsymbol{u}_{cn}\|_2$.

The local cage deformation metric uses a notional polyhedral "cage" around an element with nodes as the neighboring elements (Figure 59a). The cage deformation, d_c, is defined as the maximum difference between displacements $\mathbf{u}$ of any two nodes, i.e. neighboring elements, $d_c = \max(\|\boldsymbol{u}_i - \boldsymbol{u}_k\|)$. This metric was found to work well for shear band visualization.

2.2.6.5. Volume conservation analysis

Volume conservation was tracked in the central, uniform diameter cylindrical section of the assembly, i.e. in the uniform gauge section spanning from H_1 to H_2 (Figure 59). Volume conservation was analyzed using three different metrics: comparison of ideal (i.e., where plastic deformation is volume conserving) and current cross-sectional areas of the cylinder, computation of plastic volume change, and computation of the α coefficient, which relates the elastic and plastic volume change, as defined below.

The volumetric strain during plastic deformation $\Delta V_{pl} / V_0$ was computed by subtracting the calculated elastic volumetric strain $\Delta V_{el} / V_0$ from the total volumetric strain $\Delta V / V_0$ at a given stress σ_i:

$$\frac{\Delta V_{pl,i}}{V_0} = \frac{\Delta V_i}{V_0} - \frac{\Delta V_{el,i}}{V_0} = \frac{\Delta V_i}{V_0} - \sigma_i \frac{(1-2\nu)}{E} \qquad \text{Equation 66}$$

where $\Delta V = V - V_0$, E is the Young's modulus of the assembly, and ν is its Poisson's ratio. When plastic deformation is volume conserving, the total volume change would be equal to the elastic volume change leading to a zero plastic volume change.

The α coefficient represents the relation of elastic and plastic volume change at any time i of the simulation:

$$\alpha_i = \frac{\frac{\Delta V_i}{V_0} - \sigma_i \frac{(1-2\nu)}{E}}{\varepsilon_i - \frac{\sigma_i}{E}} \qquad \text{Equation 67}$$

Here ε_i is the instantaneous strain and $\Delta V_i / V_0 = (V_i - V_0)/V_0$ is the difference between current volume V_i and the initial volume V_0, thus referring to the total volume. When α is 0.0, plastic deformation of the system is volume conservative. Positive α values indicate the volume is increasing with plastic extension. Below the yield stress, α is not well defined and thus it should be considered only in the plastic region of the deformation.

Ideal cross-sectional area $A_{ID,i}$ at time *i* was calculated using the definition of α coefficient (Equation 67) and represents the cross-sectional area of the cylindrical portion of the assembly if the plastic deformation of model was perfectly volume conserving. Assuming the gauge height $H_i = H_2 - H_1$ gives:

$$A_{ID,i} = \left(1 + \sigma_i \frac{(1-2\nu)}{E}\right) \frac{V_0}{H_i} \qquad \text{Equation 68}$$

The volume of the cylindrical section at any given strain was computed as the volume of a tight envelope built around the cylinder from positions of element centers. The only elements included in the construction of the envelope were elements originally present in the cylindrical region between vertical positions H_1 to H_2 (Figure 59).

2.2.6.6.Non-hardening Plasticity Results

To gain insight into the element-scale formation of fractures, plastic deformation was performed with the bond strengths adjusted to give three different bond breakage modes: (1) bonds break only in tension; (2) bonds break approximately evenly in tension and in shear; and (3) bonds break only in shear. This was achieved by: (1) setting the shear strength value relatively high; (2) setting both shear and tensile strengths to similar values; and (3) setting the tensile strength relatively high.

Figure 60 shows the stress-strain curves for all three cases. The strain at which the sample fails increases with an increasing number of bonds that fail in shear. This originates in the interchange of the two deformation mechanisms – elongation and slip. When bonds break in tension, the material deforms by bond elongation in the axial direction, which promotes cracks to open. On the other hand, when bonds break in shear, the assembly is able to deform somewhat along shear band planes and thus introduce slip-like behavior that increases the ductility.

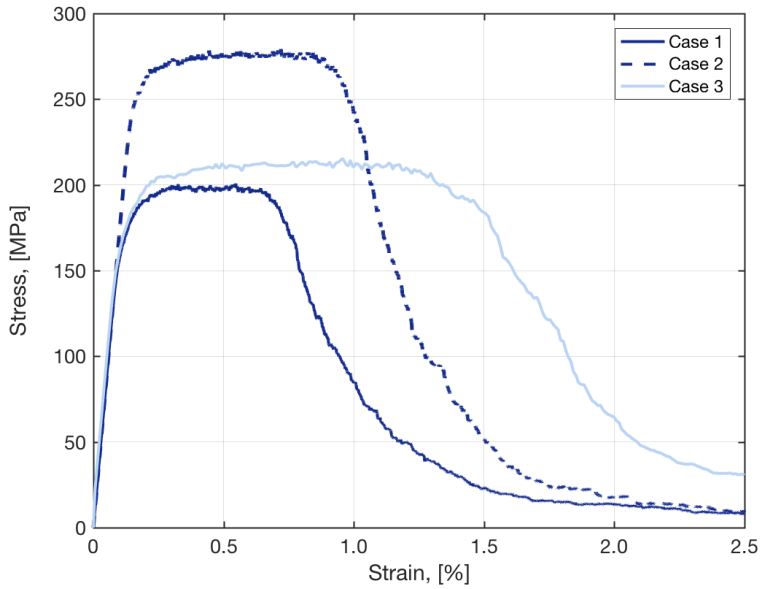

Figure 60. Stress-true strain curves for Case 1 (all bond failures are in tension), Case 2 (bond failure mode is approximately equal between tension and shear), and Case 3 (all bond failures are in shear).

Results of the d_{2min} deformation analysis are presented in Figure 61. The angle of high and low d_{2min} patterns are closer to the 45-55º characteristic angles for shear bands in Case 3 where all bond failures are in shear. This is also true for the final fracture angle. For Case 1 the fracture angle is much closer to horizontal, while for bonds only failing in shear, the fracture forms along a characteristic angle that is similar to shear bands (e.g., 45-55º). However, while the d_{2min} analysis reasonably predicts the future crack location and inclination in Cases 1 and 2, it fails to do so in Case 3.

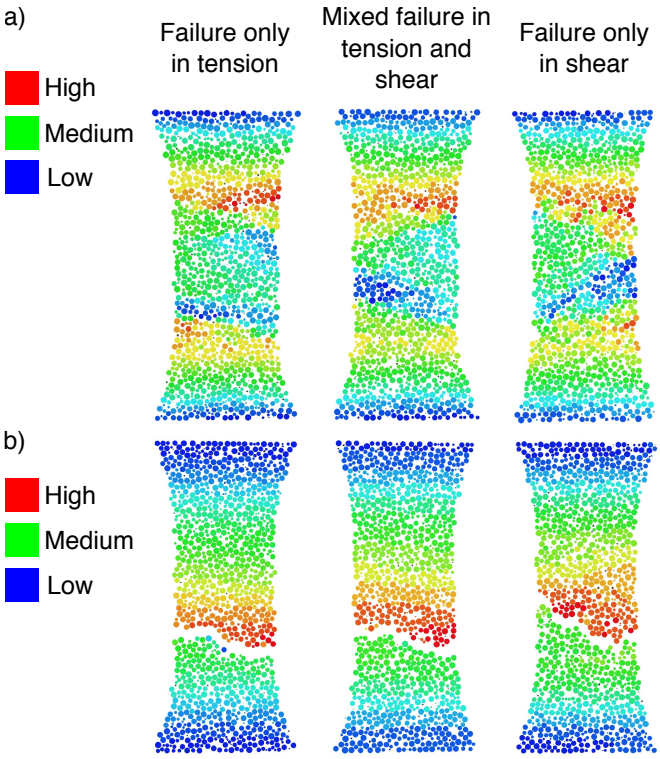

Figure 61. Results of the d_{2min} analysis in the central cross-sections of the assembly for cases where (1) bonds break only in tension; (2) approximately half of the bond failures are in tension; and (3) bonds break only in shear. (a) at a strain of approximately 0.005 and (b) at fracture.

The localization of deformation on shear bands is even more visible through the local cage deformation analysis (Figure 62). The shear bands were visualized by plotting elements with local cage values 2-3 times larger than the assembly mean. The angles in Figure 62a were obtained from fitting the shear band areas in three dimensions with a plane. The angles in Figure 62b were computed from fitting of the actual fracture planes. Note that due to the 3D nature of these planes, they do not always look to match the depicted 2D representation. When the bonds fail predominantly in tension, we get a behavior similar to mode I fracture with a fracture plane almost 90° from the loading axis. In contrast, as the fraction of bonds breaking in shear increases, the localization patterns become less horizontal and into the range of 48 – 60° seen for bulk metallic glasses (BMGs) in tension (Lund and Schuh, 2003; Schuh et al., 2007; Zhang et al., 2003). As opposed to the d_{2min} patterns, the shear bands in the cage analysis align with the final fracture angle and position in the assembly for all cases.

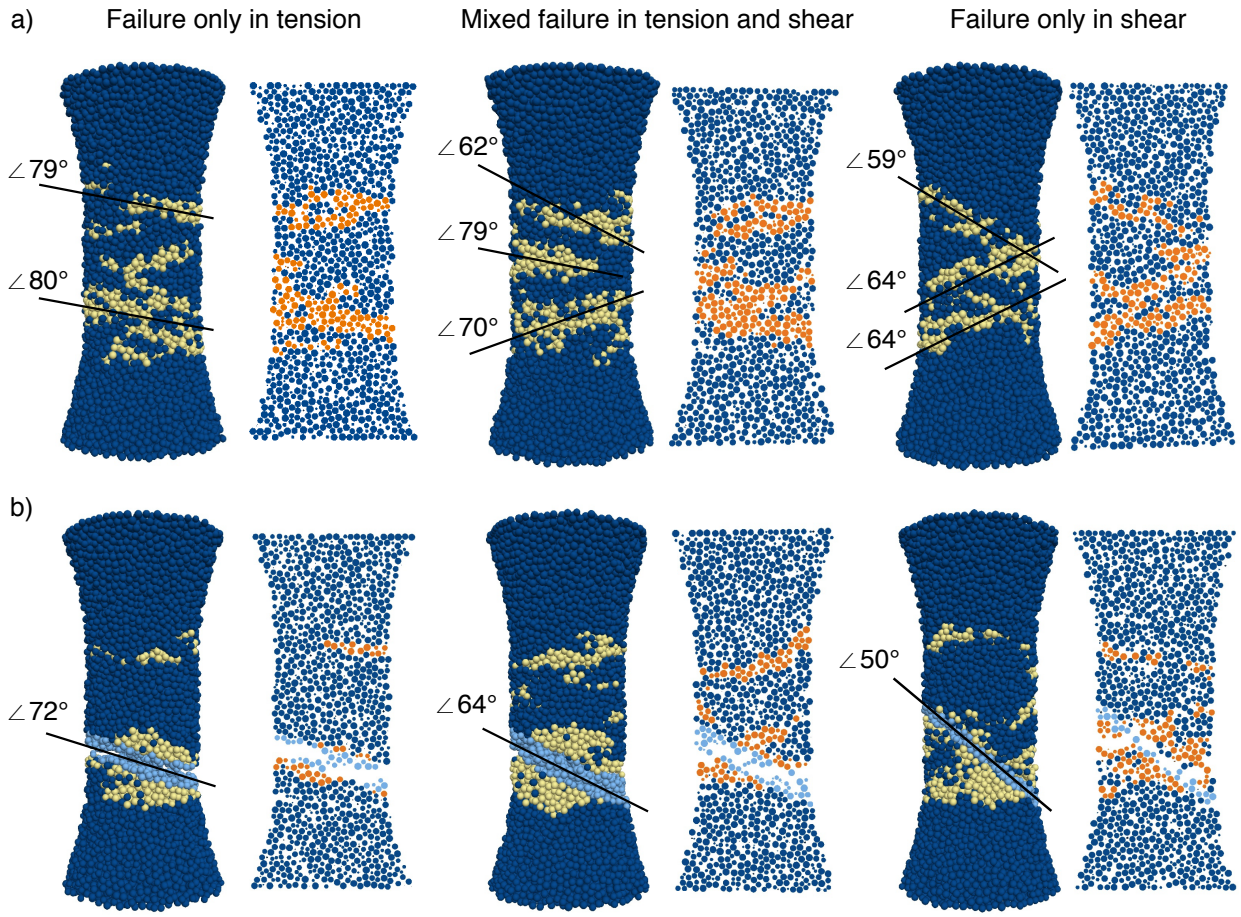

Figure 62. Results of the local cage deformation analysis in the assembly and its central cross-sections (a) at a strain of approximately 0.5% and (b) at fracture (b). Gold/orange indicates cage deformation values 2-3 times larger than the mean. Light blue (b) indicates the elements surrounding the fracture.

Figure 63 shows the results of volume conservation analysis. The results indicate that the volume during plastic deformation is not conserved. While the assembly contracts laterally as shown in Figure 63a, the reduction in cross-sectional area and the rate of contraction is not sufficient to maintain a constant volume. The results are similar for all three cases, though plastic volume change and α coefficients are lower for the mixed failure and shear-only failure cases.

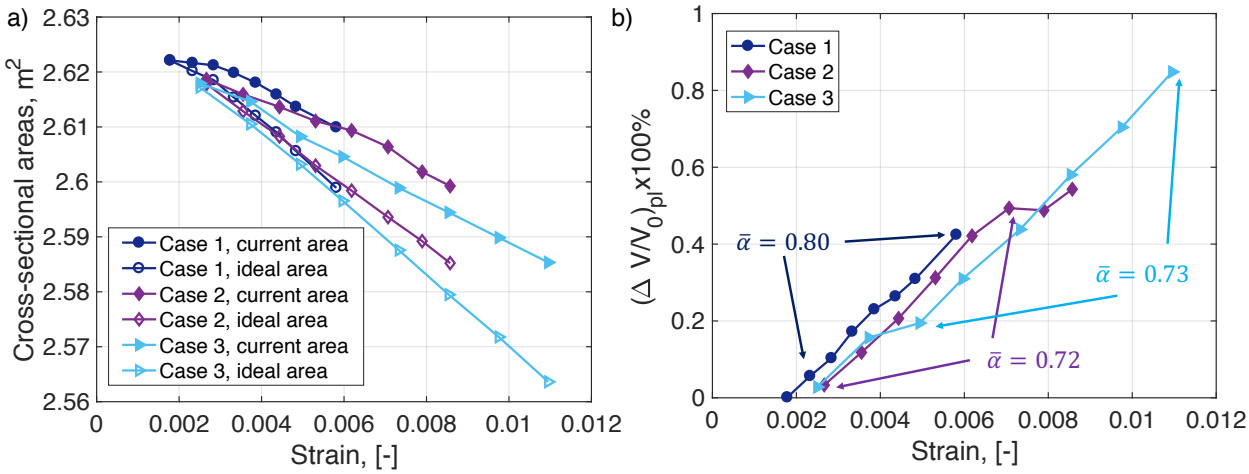

Figure 63. Results of the volume conservation analysis: a) Current and ideal cross-sectional areas of the assembly b) Plastic volume change as a function of strain with average α coefficient values during main plastic deformation parts of the simulations. In Case 1 all bond failures are in tension, in Case 2 the bonds failure mode is approximately equal between tension and shear, and in Case 3 all bond failures are in shear.

2.2.6.7. Comparison with plastic deformation of non-hardening solids and other methods used for plasticity simulations of continuum materials

The isotropic, non-hardening DEM model developed here for solid materials can be viewed as an initial framework for the modeling of many amorphous materials, for instance glassy polymers and bulk metallic glasses (BMGs). Indeed, the limited plastic deformation (~1%, Figure 60) and localization of deformation onto shear bands (Figure 62, cases 2-3) is reminiscent of the observed tensile behavior for ductile BMGs (Dmowski et al., 2010; Scudino et al., 2011).

On the micro- and nanoscales, amorphous materials like BMGs are inherently heterogeneous, both in structure and mechanical properties (Ding et al., 2014; Dmowski et al., 2010; Ketov et al., 2015; Li et al., 2015; Liu et al., 2011; Wang et al., 2016). This gives rise to a number of unique mechanical phenomena like non-affine deformation (Hufnagel et al., 2016), local, irreversible plasticity occurring during elastic deformation (Hufnagel et al., 2016), and length-scale dependence of stress-strain response (Furukawa and Tanaka, 2009; Murali et al., 2011; Rycroft and Bouchbinder, 2012). Due to the complexity of these phenomena and limitations of experimental measurements, computational models are often needed to help understand the structure and properties of amorphous materials (Anand and Su, 2005). This is because the atomistic details of the fracturing process and related shear banding are quite difficult to capture experimentally (Sun and Wang, 2015). However, the atomistic models commonly used to provide insight (e.g., molecular dynamics) are generally limited to two atomic component systems and very short time scales. Because of these limitations, there is motivation to develop mesoscale modeling methods that can inherently capture the stochastic nature of shear band formation and fracture and provide a practical way to predict mechanical performance in engineering applications.

DEM models inherently begin with an assembly structure that introduces heterogeneity to the local mechanical properties through the random structure variability, i.e., locally dense versus relatively loosely bonded regions, akin to the real variability of amorphous materials. Moreover,

the additional inclusion of random heterogeneity into the element interaction laws (e.g., stiffness, strengths, etc.) is straightforward. In either case, the intrinsic heterogeneity of the DEM model captures non-affine deformation on a local level as well as the emergence of shear band localization (Figure 62, Cases 2-3). Fracturing in the model is spontaneous and when shear bond failure controls the deformation, the fracture angle falls in the observed range of angles (48 – 60°) for BMGs in tension (Lund and Schuh, 2003; Schuh et al., 2007; Zhang et al., 2003) (Figure 62, Case 3). The nature of the fracture – brittle mode I or shear band instability – can be controlled by adjusting relative contributions from two bond breakage modes – tensile and shear. This is consistent with molecular dynamics findings of (Murali et al., 2011) where the brittle BMG fracture was found to originate from void nucleation whereas ductile BMG fracture developed through shear banding. In the DEM-based model presented here, tensile breakage of element bonds favors void nucleation by separating the elements and expanding the volume more rapidly (Figure 63b) while the shear breakage introduces more lateral, shearing deformation of the assembly.

For some examples of non-hardening solids, such as bulk metallic glasses, large quantities of heat can be generated during local plasticity and thus the evolution and propagation of shear bands is intimately related to how locally generated heat enables thermally activated deformation processes, or even localized melting (Greer et al., 2013; Hufnagel et al., 2016; Schuh et al., 2007). These processes are dictated by a balance of the rate of heat production and heat dissipation through thermal conduction. Accordingly, predictive models of plasticity in BMGs, such as those developed by Li (Zhao and Li, 2011), often solve for the deformation field and the temperature distribution simultaneously. The DEM model as presented in this manuscript only models the displacement fields of the materials undergoing plasticity as an important first step; however, there is no fundamental impediment to extending it to simultaneously model thermal evolution and including temperature dependent plasticity laws. Indeed, computing the thermal conductivity for granular materials is routinely performed with DEM simulations and is used as a well-established diagnostic of granular packing (Evans et al., 2011; Yun and Evans, 2010).

Table 12. Summary of numerical methods currently used for modeling plastic deformation of non-hardening solids and their comparison with DEM.

Method	Advantages	Disadvantages	Differences with DEM
Coarse-grain models Continuum representation (Furukawa and Tanaka, 2009; Rycroft and Bouchbinder, 2012)	Captures well certain deformation phenomena	Cannot model stress-strain distribution near crack tip Cannot model complex, multiaxial loads	DEM can model complex loads and resolve stress-strain distribution during interactions with objects such as a crack tip
FEM Continuum representation (Dolbow et al., 2001; Gao et al., 2016; Tandaiya et al., 2009; Zheng and Shen, 2011)	Modeled deformation is quantitatively and qualitatively accurate	Difficulties handling discontinuities and crack propagation. Increased complexity to do so	DEM readily handles discontinuities and models crack propagation
Phase field Continuum representation (Zhang and Zheng, 2014; Zheng and Shen, 2011)	Modeled deformation is quantitatively and qualitatively accurate	Fracturing based on density distribution not real detachment of material.	DEM treats fractures and cracks explicitly.
RFM, DRFM Discrete representation (Picallo et al., 2009, 2010)	Can handle discontinuities Can model both ductile and brittle plastic deformation	Unclear if possible for expansion to model anisotropy, creep, fatigue etc.	Regular lattice model as opposed to heterogeneous DEM
Peridynamics Discrete representation (Fu et al., 2001; Madenci and Oterkus, 2016a; Madenci and Oterkus, 2016b; Silling, 2000; Sun and Sundararaghavan, 2014)	Can handle discontinuities Good agreement with experimental data for various types of materials	Thus far applied only on regular lattice mesh, no geometric heterogeneity Needs detailed constitutive laws Limitation on Poisson's ratios achieved	Integral, not differential formulation

MD and other atomistic Atomistic representation (Lund and Schuh, 2003; Murali et al., 2011)	Most microscopically accurate and least relying on constitutive laws. Source of a lot of credible information on the physics of BMG deformation and fracturing.	Limited to small dimensions, short times, and binary atomic systems	DEM can model larger systems during longer, representative times. DEM formulation is very similar, mathematically, so it can more readily incorporate MD findings, like the LJ potential.

Results of this study reveal that DEM has distinctions compared to other discrete methods and the modeling methods currently used for amorphous materials such as coarse-grain models, finite element models, and phase field and atomistic simulations (Hufnagel et al., 2016; Sun and Wang, 2015). The characteristics of these methods compared to DEM are outlined in Table 2. As opposed to coarse-grain models (Furukawa and Tanaka, 2009; Rycroft and Bouchbinder, 2012; Sun and Wang, 2015), DEM is capable of modeling multiaxial, complex deformation including stress and strain distributions near the crack in the material (Jebahi et al., 2013). Although these tasks can be readily accomplished by continuum methods, such as the finite element method (FEM) or the phase field method, both of which require constitutive laws (Dolbow et al., 2001; Gao et al., 2016; Tandaiya et al., 2009; Zheng and Shen, 2011), DEM provides a more straightforward treatment of the actual material separation at fracture. FEM differential, continuum formulation requires complex treatment of discontinuities such as fracture (Zheng and Shen, 2011), while phase field models do not resolve the fracture explicitly, rather as a zero density in the density field (Zhang and Zheng, 2014). In inherently discontinuous DEM, fracturing occurs spontaneously (i.e., it is an emergent behavior) and fracture propagation is modeled explicitly by removal of bonds between elements followed by their relative rearrangements. Handling of discontinuities and fracturing is a strength of other discrete methods – including peridynamics (Fu et al., 2001; Madenci and Oterkus, 2016a; Madenci and Oterkus, 2016b; Silling, 2000; Sun and Sundararaghavan, 2014), and lattice-based random fuse and ductile random fuse models (Picallo et al., 2009, 2010). Both of these methods were successful in reproducing brittle (Ha and Bobaru, 2011; Picallo et al., 2009) and ductile behavior (Madenci and Oterkus, 2016b; Picallo et al., 2010; Sun and Sundararaghavan, 2014) of solid materials. A limitation of the present work, and similar to bond-based peridynamics, that that our current DEM formulation limits the Poisson's ratio to about 0.2 and does not properly conserve volume during plastic deformation (Madenci and Oterkus, 2016a). Regarding the elastic properties, it has been demonstrated that a modified DEM formulation can be used to give anisotropic elastic constants matching many realistic cubic single crystals and accurate modelling of the elastic properties is an ongoing area of research (Truszkowska et al., 2017).

The major differences when comparing other discrete methods, such as peridynamics and random fuse models, to DEM are that DEM is naturally heterogeneous, its grid is not regular, and its elements are truly distinct entities. This makes DEM compelling framework with the potential to model phenomena that other discrete and mesoscale methods do not capture. Finally, atomistic simulations like molecular dynamics (MD) are widely used to study the microscale behavior of amorphous materials (Lund and Schuh, 2003; Murali et al., 2011) and DEM and MD are very similar in their mathematical formulations. Accordingly, DEM can incorporate elements

and findings of MD results in forms closer to the original atomistic ones while enabling simulations at representative spatial and temporal scales, currently unattainable by MD.

In future work, DEM may be further modified to include more complex, physically justified element interaction laws to more accurately simulate the material response on the local scale. This may be accomplished by considering constitutive laws like that proposed by (Anand and Su, 2005) and those used in MD simulations. With further development, the DEM framework for continuum modeling may provide a powerful predictive tool for plasticity and damage evolution in solids.

2.2.6.8. Summary of Non-Hardening Plasticity

This work successfully adapted the discrete element method, originally developed for the modeling of unbound granular assemblies and later, brittle solids, to model isotropic non-hardening plasticity in solids. Additionally, two deformation analysis tools, d_{2min} and local cage deformation, were explored to visualize non-affine deformation and shear band formation leading up to fracture. While both tools indicate degrees of local deformation of the assembly, the local cage deformation highlighted the presence of shear bands and better showed how they evolved to cause final fracture.

The DEM model successfully simulated tensile plastic deformation by shear band formation until failure up to strains of about 1%, which is a behavior characteristic for some non-hardening materials of practical importance such as bulk metallic glasses. The model behavior was governed by two competing mechanisms, bond elongation and slip, which have relative contributions that are set by the bond failure mode, tensile or shear. As the shear/slip mechanism becomes more pronounced, deformation becomes localized on shear bands, one of which eventually fractures, which is behavior akin to metallic glasses in tension.

2.2.7. *Isotropic plasticity with strain hardening*

There were two DEM models developed for simulation of plastic deformation with hardening. The first one relied exclusively on parallel bond formalism described in the previous sections while in the second an additional, non-linear pairwise potential was introduced on top of the linear parallel bond deformation. Both models followed the same basic DEM framework and assembly generation described earlier with any additional steps indicated.

2.2.7.1. Hardening with parallel bond formalism only

2.2.7.1.1. Local and nearest-neighbor hardening

Figure 64 shows the results of implementing two strain hardening methodologies – one that acts locally at a single element and another that hardens the neighborhood including the next nearest neighbors. To match the experimental behavior, the percent hardening value was a free variable. In the local hardening scheme, only the broken and subsequently reformed bond would be hardened, whereas in the nearest neighbor scheme all the surrounding bonds would be hardened as well. Models were found to fracture at about 5-8% strain regardless of what hardening scheme was used.

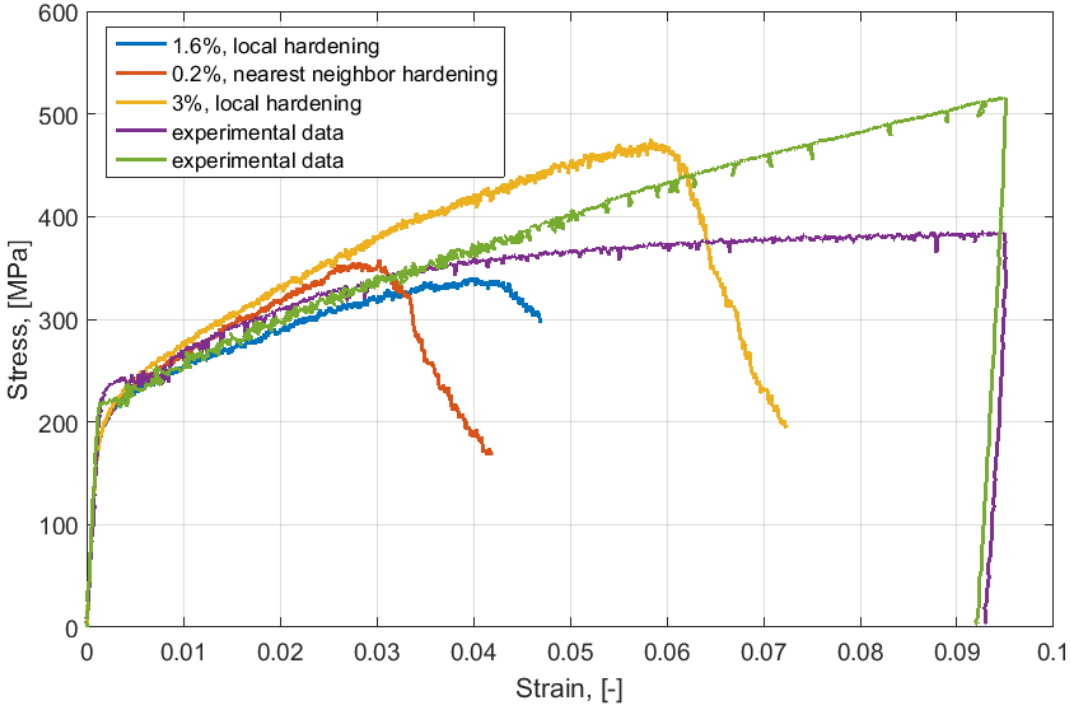

Figure 64. Simulations of tensile testing with various degrees and types of hardening compared to the experimental data. Note that the experimental samples fail at around 20% strain and the displayed data is from experiment that were stopped before failure occurred.

2.2.7.1.2. Investigation of plasticity mechanisms

To understand what triggers the onset of fracture in our simulations, we selected regions around the crack to compare with regions far away to identify local structural signatures that control fracture (Figure 65). We have also performed identical simulations and analysis with using geometrically identical assemblies with statistically different element arrangements to confirm

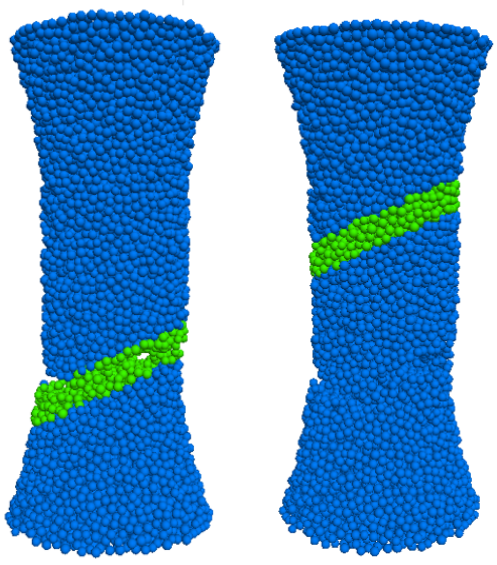

Figure 65. Investigated cross-sections around and away from crack. Green particles are the ones included in the analysis.

that our conclusions are a general feature of our DEM method rather than an artifact of one assembly (Figure 66).

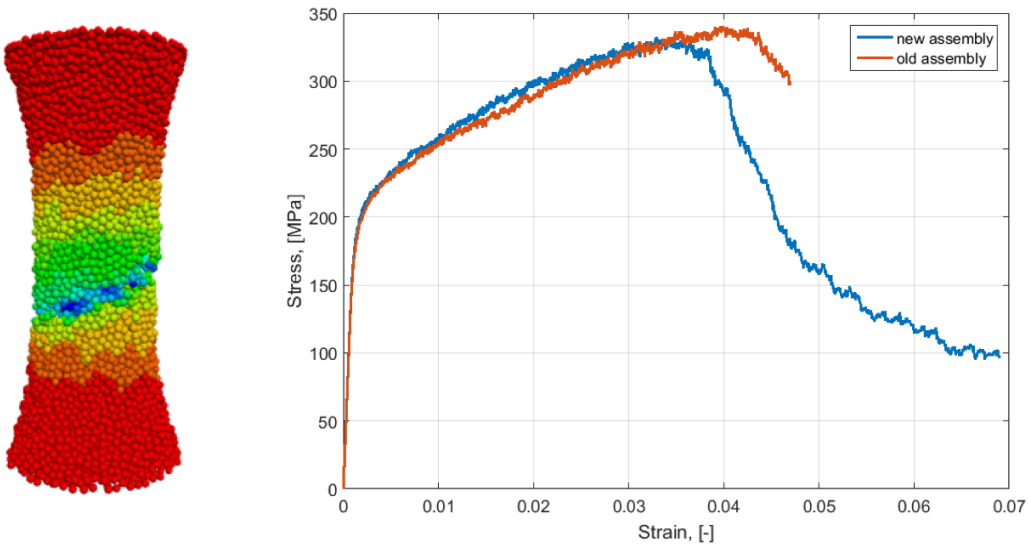

Figure 66. Statistically different assembly were used to give similar stress-strain response (at right); however, the onset of failure is different due to structural differences between the assemblies. The second assembly (at left) fractured at a different location from the first one (Figure 65).

Our analysis has involved looking for structural defects (e.g., elements with low coordination number) prone to initiating fracture along with other potential fracture indicators like inhomogeneous stress or force distributions. Figure 67 shows some of the structural analysis tools we developed for probing the local element coordination number. Figure 67a shows the average element coordination values in measurement volumes used to compute stresses and strains in the assemblies. Blue colored volumes indicate coordination numbers slightly lower than average and the red colored, slightly higher. Although the differences are small, this analysis indicates certain structural patterns exist including regions of relatively low coordination number that may be structurally weaker than other parts of the assembly. Figure 67b shows coordination numbers of every element in a center slice of the assembly in Figure 65. Even though coordination values look evenly distributed, when only low values are plotted (Figure 67c) patterns consistent with Figure 67a emerge, indicating spots of lower coordination in the bottom part of the assembly. Figure 68 compares the two different assemblies, their front and center cross-sections with only low coordination values plotted. Comparing these low coordination maps to Figure 65 and Figure 66, it can be seen that predicting the failure location solely based on structural patterns is not straightforward; however, we believe it provides useful information that should be considered in any future work.

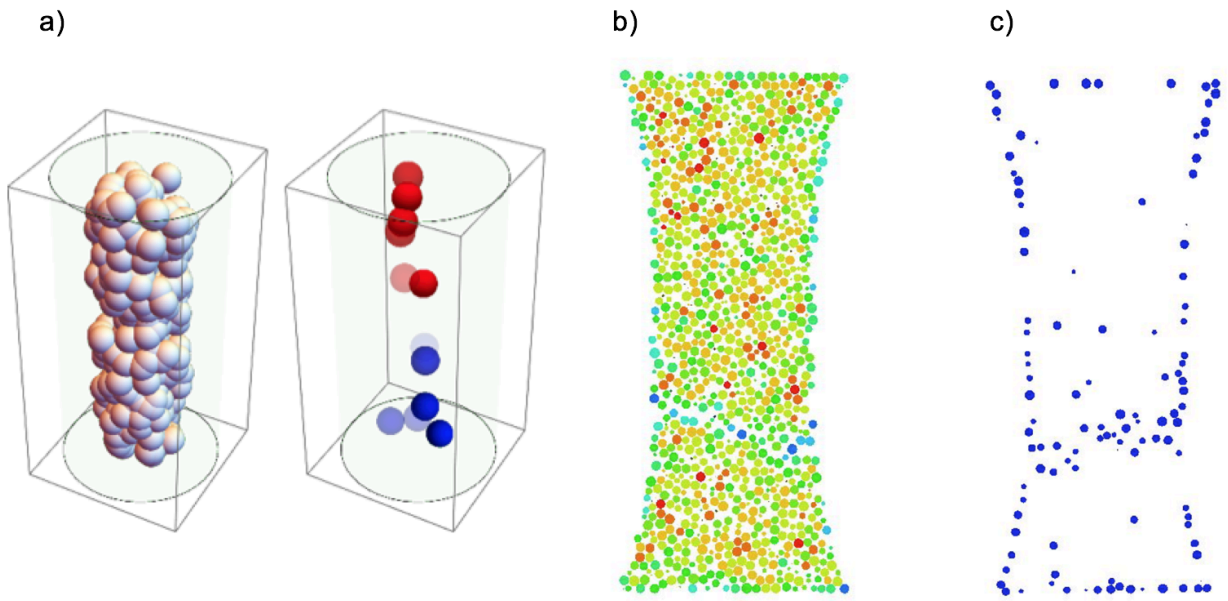

Figure 67. Results of coordination number analysis of the assembly in Figure 65: a) Measurement spheres and spheres with high (red) or low (blue) average coordination b) Element coordination number in the assembly during fracturing c) Elements with number of contacts less than 6 during fracturing as seen from the opposite side to b).

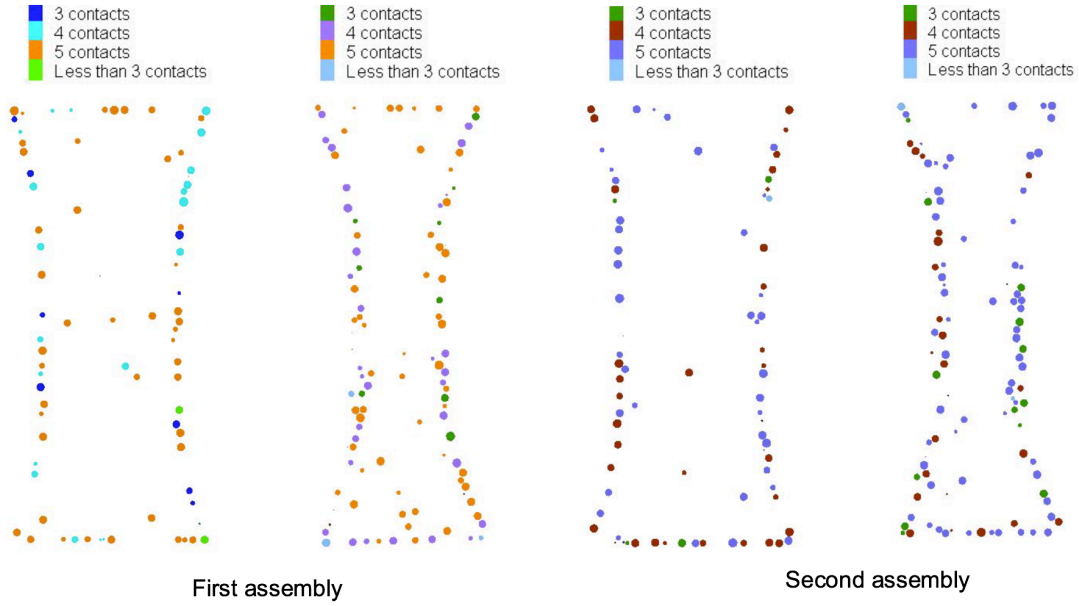

Figure 68. Elements with low coordination number during initial stages of the simulation in the first (Figure 65) and statistically different second (Figure 66) assembly. Two cross-sections were analyzed, one in the center and another offset from the center.

Figure 69 shows the element coordination number during the simulation in the vicinity of the crack as failure progresses. Figure 70 shows the two assemblies split into 20 layers, with each layer colored by its average coordination number. 10, 20, and 50 layer segmentations were tested

and the results confirm that structural inhomogeneous likely affect the location of specimen failure in the DEM simulations.

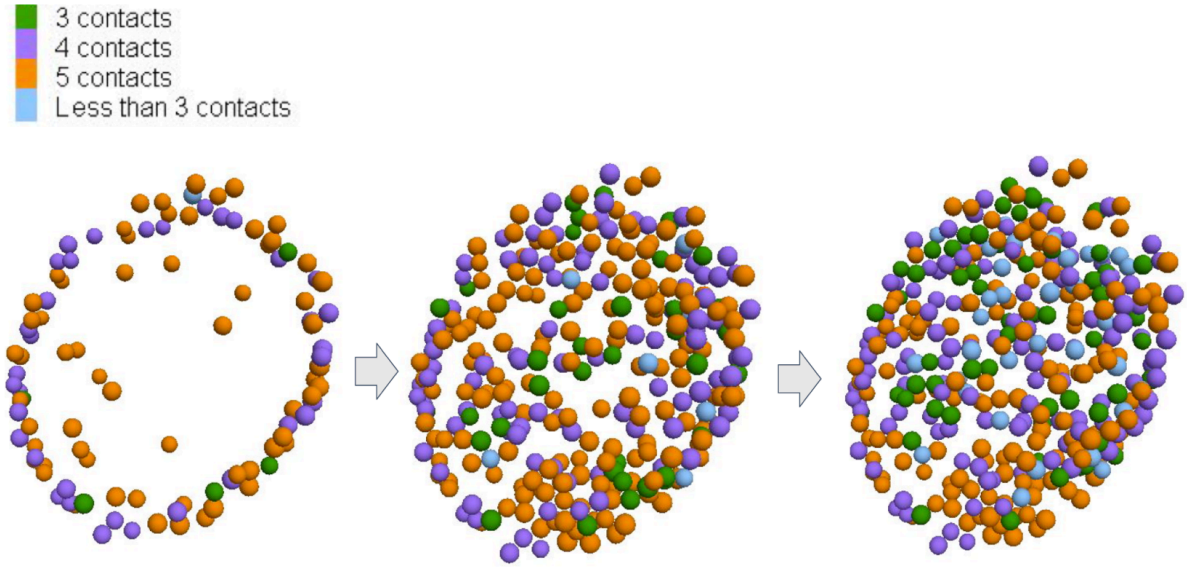

Figure 69. Elements with a low coordination in the area around the crack as the simulation progresses in the first assembly.

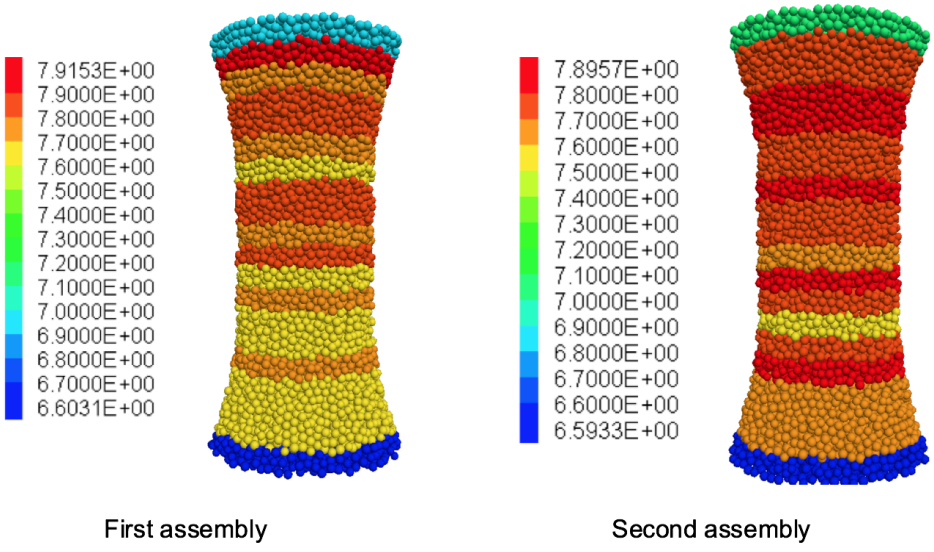

Figure 70. Both assemblies split into 20 layers, with each layer colored by its average coordination number. Besides the grip elements on top and bottom the coordination number does not vary greatly in each layer but a pattern emerges indicating slightly lower coordination in the assembly's bottom halves where failure initiated.

Besides analyzing the structure of the assemblies, we have also analyzed the deformation using the metrics presented in Section 2.2.6.4. Results of the d2min analysis, shown in Figure 71, indicated locally large deformations at a few locations but did not identify shear band formation.

The results of local cage deformation analysis shown in Figure 72 clearly indicate deformation occurs by shear bands that crisscross though the sample gauge length at ~45° to the loading axis as expected. However, these presence of shear bands does not seem to be related to the location of final fracture.

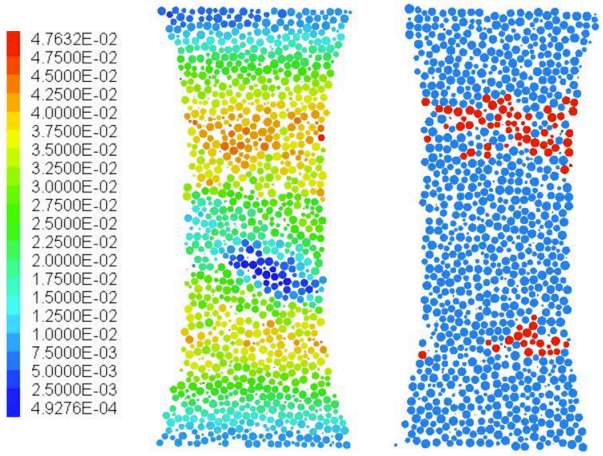

Figure 71. d2min analysis of the second assembly. Left – all the d2min values in a central cross-section; Right – red values indicate particles with d2min values about 2 or more times larger than the assembly mean.

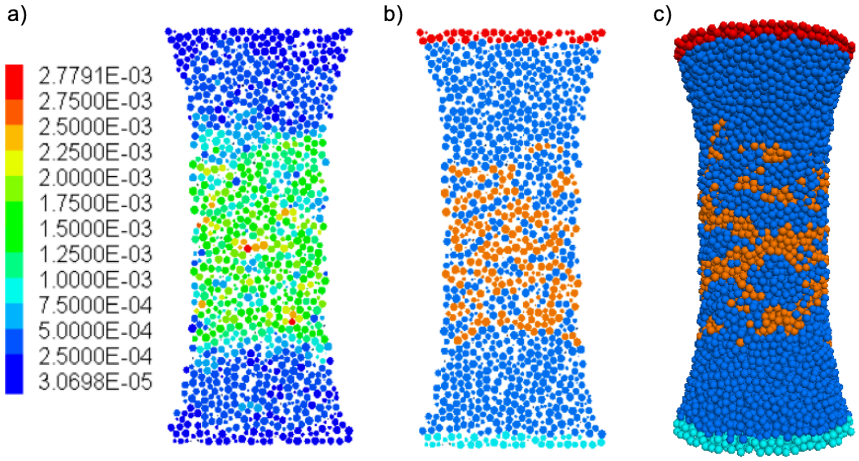

Figure 72. Shear band formation captured by the cage deformation analysis: a) Cage deformation values in the assembly's cross-section. b) Particles with cage deformation values 1.97 or more times larger (orange) than the average in the assembly's cross-section c) 3D view of the particles with large cage deformation. In b) and c) the blue particles are the sample interior, the red and cyan are top and bottom grip particles that drive the deformation.

2.2.7.1.3. Force restoration

When a bond breaks it reaches a maximum shear stress, after which, if its length is smaller than a fixed threshold the bond is reformed slowing slip-like plastic deformation behavior. The bond reforming for the models discussed above did not restore any force on the bond; hence, each reformed bond has ~0.0 initial stress but a longer length. This can cause elements to extensively stretch apart in the normal direction, potentially opening into a crack. On the assembly scale, such crack formation may cause premature brittle fracture rather than plastic slip.

In a plastically deforming metal, normal force is generally sustained across slip planes while shear deformation occurs. To better represent the physics of metal deformation and suppress crack formation, we have investigated reforming bonds with the normal force restored to the same value prior to shear failure. To investigate the influence of force restoration we have simulated the first assembly in this section (Figure 65) with the normal force being fully or partially restored every time a bond breaks in shear. Figure 73 shows the stress-strain responses of an assembly with only 10% of the normal force being restored such that the resulting macroscopic stress values become comparable with the experimental data. Restoring the full normal force to that same model causes a very large increase in macroscopic strain hardening response of the assembly, possibly due to bond reorientation and geometric hardening. Thus, it is concluded there is a strong interaction between force restoration and hardening that needs to be understood.

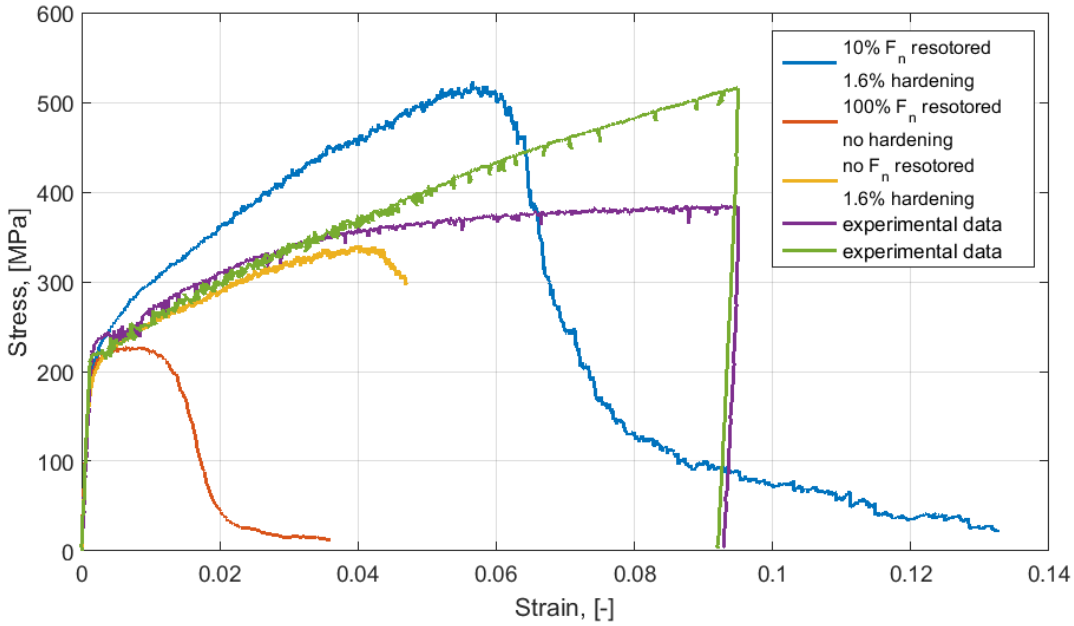

Figure 73. Simulations of tensile testing with normal force restoration compared to simulations without force restoration and our experimental data.

2.2.7.1.4. Small assemblies with hardening distribution

To further investigate the insensitivity to the details of the hardening law, we have developed a hardening distribution law and tested it with small and fast 3D models. The small models were first simulated using our usual hardening schemes and compared to the large models as plotted in Figure 74. The agreement in the macroscopic stress-strain response was sufficiently close to consider the small models as a good first approximation in allow further testing.

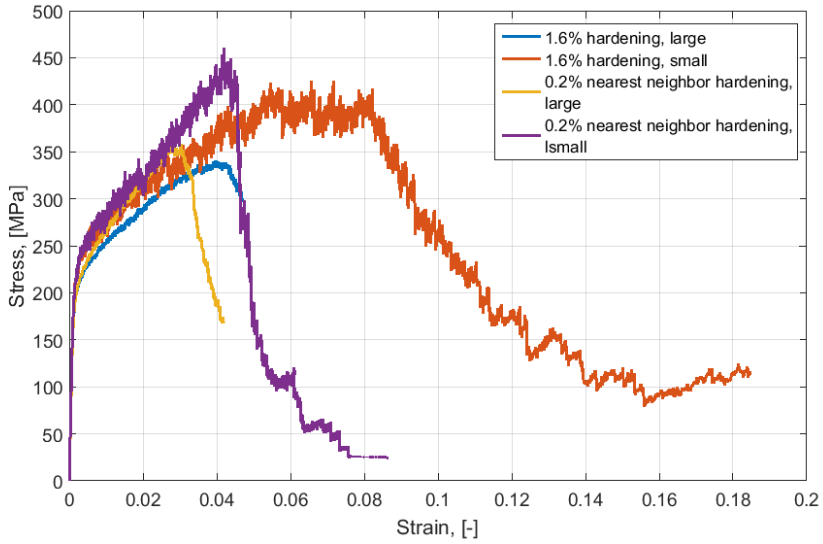

Figure 74. Comparison of stress-strain response in large and small models.

We used an exponential distribution function to introduce non-local hardening. When a bond broke, hardening is applied to all bonds that fall into the hardening region determined by the distribution. The amount of hardening followed an exponential decay curve as shown in Figure 75 and would equally affect axial and lateral bonds. The hardening of the broken bond was determined by:

$$\tau_C = (1 + C_2)\tau'_C \qquad \text{Equation 69}$$

Where C_2 is the hardening factor and τ are the shear strengths before and after hardening. The hardening of any other bond in the assembly was determined as

$$\tau_{CN} = \left(1 + C_1 e^{-\alpha |d_{Aj}|} C_2\right)\tau'_{CN} \qquad \text{Equation 70}$$

Here $\mathbf{d_{Aj}}$ is the distance between the broken bond and the other bond. C_1 is a scale parameter that determines the maximum amount of original hardening that will be applied to the other bonds. α is the parameter that controls speed of exponential decay – the lower the α, the more non-local the hardening will be. As seen in Figure 75, α value of 2 causes hardening of the entire assembly whereas $\alpha = 20$ limits the hardening to the next nearest neighbor.

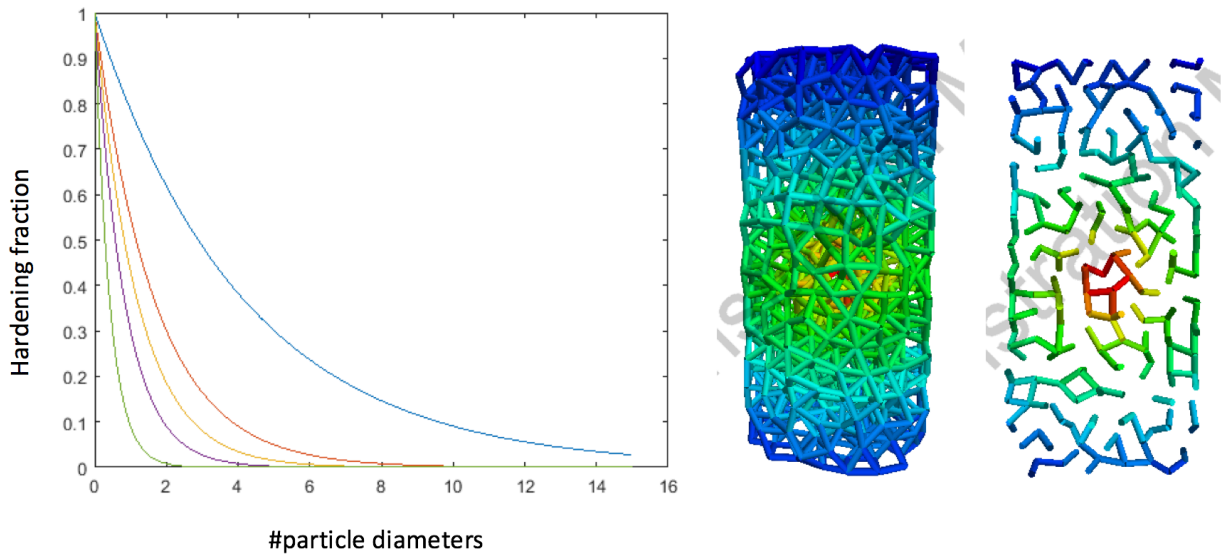

Figure 75. Hardening distribution scheme. Graph shows the influence of various values of the α parameter on the non-locality of hardening. Small α values will cause hardening of the entire assembly (blue line = 2) while large will limit it to as little as next nearest neighbors (green line = 20). Pictures on the right show exaggerated hardening that follows this distribution in a case of central bond breaking.

The simulations were performed with various values of the α coefficient and thus variable localization of the hardening. The scale parameter C_1 was tuned so that the stress-strain response of each set compared reasonably to our experiments. Results, shown in Figure 76, indicated that once the stress-strain response is tuned to become similar to experimental data, regardless of the non-locality of hardening used, all assemblies fail at similar strains. Overall, it was concluded that the model response is relatively insensitive to the details of the hardening function. As explained in the next section, the actual permanent bond failure and related failure of the sample are mostly a function of the maximum gap parameter. Furthermore, while the failure mechanism is a combination of void formation and shear banding, the desired element slip mechanism is generally not achieved by any of the proposed models. The models deform by elongation with insufficient lateral contraction, which also causes low volume conservation shown in Section 4. Nevertheless, proposed model may be capable of simulating proper metal deformation with further changes to its force-displacement laws. Thus, the various hardening schemes proposed in this sections may still be of use depending on the simulated material.

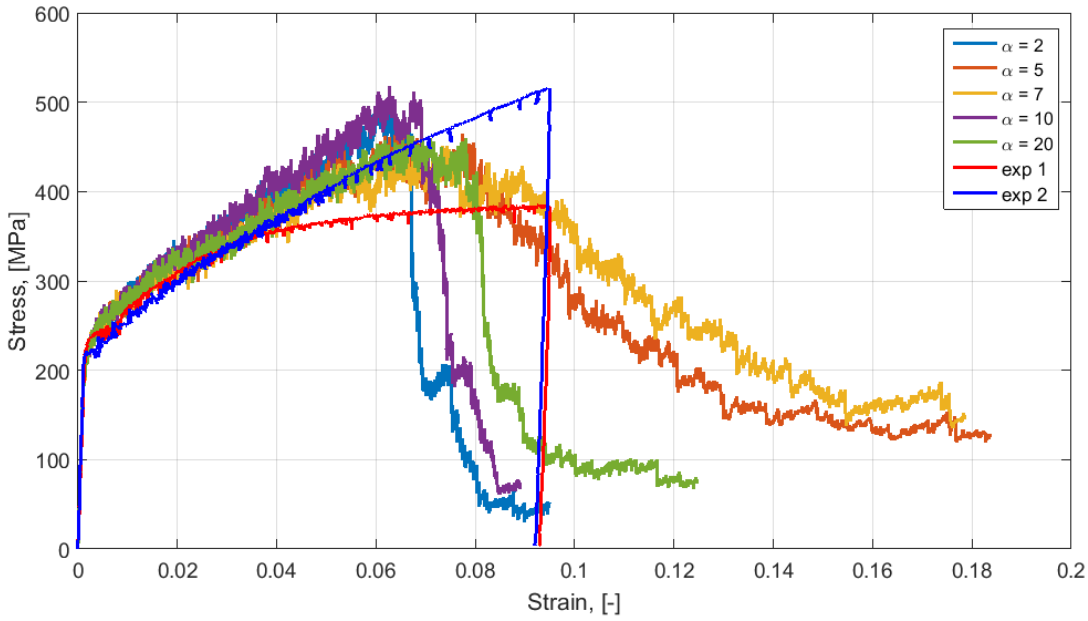

Figure 76. Macroscopic stress-strain response of assemblies with varying amount of non-local hardening as compared to experimental data. All the assemblies fail roughly at the same strains regardless the amount of non-local hardening introduced. The small differences in strain to failure were attributed to failure occurring near the grip or in the interior of the assembly.

2.2.7.2. Introduction of a non-linear pair-wise potential

2.2.7.2.1. Pair-wise potential formulation

This part of our work achieves a stress-strain response of a metallic material through addition of a Lennard-Jones-like pair-wise potential to the bonded DEM framework introduced in Section 2.2.4.2 and 2.2.6.1. The pair-wise potential had the form of the classical Lennard-Jones potential as shown in Figure 77,

$$\mathbf{F}_{ij} = f_{ij}\mathbf{n}_{\mathbf{c}} \qquad \text{Equation 71}$$

where f_{ij} is the force between two elements i and j that depends on the distance between element centroids, r_{ij},

$$f_{ij} = \begin{cases} 24\varepsilon\left(\dfrac{2\sigma^{12}}{r_{ij}^{13}} - \dfrac{\sigma^{6}}{r_{ij}^{7}}\right) & , \quad r_{ij} < R_c \\ 0 & , \quad r_{ij} \geq R_c \end{cases} \qquad \text{Equation 72}$$

With

$$r_{ij} = \left\| \mathbf{x}_j - \mathbf{x}_i \right\| \qquad \text{Equation 73}$$

$\mathbf{x_i}$ and $\mathbf{x_j}$ are element centroids, ε is a fitted parameter that determines the magnitude of the pair-wise force, σ is a parameter that sets the proximity of elements below which pair-wise force becomes repulsive, and r_c is a user-defined cut-off radius, above which the pair-wise potential value is set to 0.0. Here σ was set to twice the minimum element radius, which introduces the possibility of elements not repelling one another while still slightly overlapping due to the presence of a small attractive force at very small separation distances. However, we selected this approach as the best compromise relative to using twice the maximum element radius or twice the mean element radius as these approaches would result in elements exhibiting repulsion when still at a distance.

As shown in Figure 77, the pair-wise potential would reach a maximum value after which it would decrease, eventually asymptotically approaching 0.0. As opposed to parallel bond force, the pair-wise force was not incremental and did not, in general, start with a 0.0 value. It was not explicitly dependent on relative velocities of interacting elements.

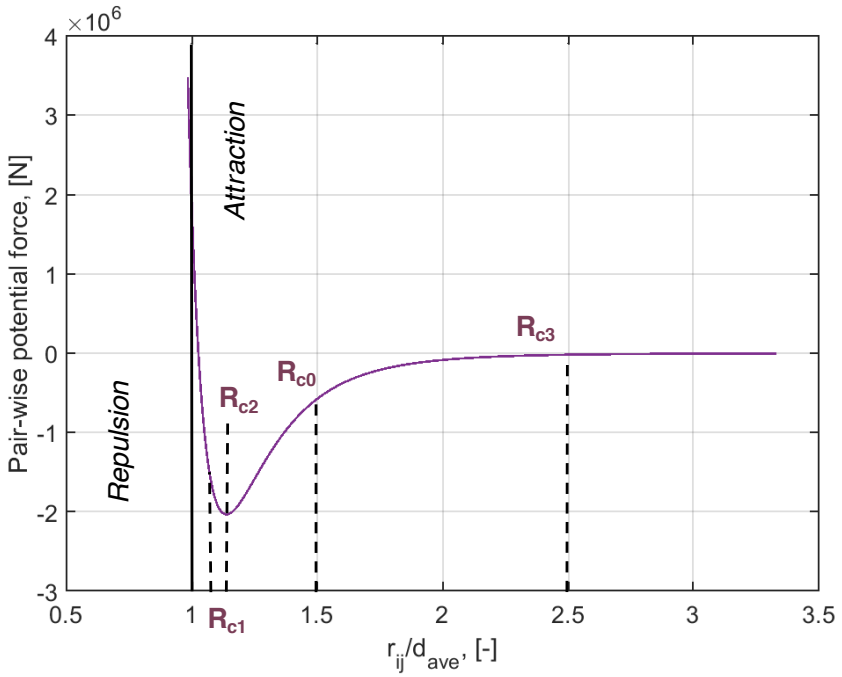

Figure 77. Pair-wise potential force as a function of element distance normalized by mean element diameter. R_{c0} indicates the cut-off distance used in the main part of this work and R_{c1} through R_{c3} are cut-offs used in the later calibration studies.

The total force on each contact between elements, $\mathbf{F_c}$, consists of the parallel bond, $\mathbf{F_b}$, and pair-wise potential contributions, $\mathbf{F}_{ij}$,

$$\mathbf{F_c} = \mathbf{F_b} + \mathbf{F}_{ij} \qquad \text{Equation 74}$$

2.2.7.2.2. Assembly preprocessing

The assembly was generated in the same way as for other plasticity models. The difference was a presence of additional preprocessing step introduced due to the pair-wise potential. As opposed to parallel bonds whose forces always start from 0.0 and evolve incrementally, the pair-wise potential initially starts with a value that is dependent on element distance and not necessarily 0.0 (Section 2.2.4.1). In order to ensure low stress values in the assembly before any deformation simulation was performed, the assembly was preprocessed following the generation procedure described in Section 2.2.4.2.

Before preprocessing the pair-wise potential was introduced to the assembly in the form that was to be used in the later simulations. The parallel bond stiffnesses were set to 0.0 in the preprocessing step as it was shown to reduce the processing time and improve achieved initial stress. At any time of the preprocessing if the average stress in the assembly reached a value in the interval between 0.0 and 0.1 MPa, the preprocessing was stopped and the assembly was ready to be used in any deformation simulations.

Preprocessing consisted of two steps: I. Simulating damped dynamics without any deformation and II. Simulation of tension or compression. In part I. similarly to first part of the assembly generation step the elements were allowed to reconfigure to equilibrium with no applied deformation or constraints. The newly installed pair-wise potential would either cause large negative stresses due to remaining overlap or large positive stresses due to long-distance forces prevailing the overlap contribution. During the first preprocessing step the elements would find their equilibrium configurations by decreasing the overlaps and/or their separation distances. After this step the assembly would reach either slightly negative or slightly positive average axial stress that would remain unchanged with further cycling. If the final axial stress was still too large for the sample to be ready for further simulations, compressive or tensile deformation would be applied in the second step of preprocessing. Both deformations were performed using the grip particles defined in Section 2.2.6.3 and Figure 59 and would usually not last long as the target axial stress would be reached rapidly. Once the sample was ready, it was used in the actual deformation simulations with parallel bonds properties restored. A typical preprocessing axial stress evolution with time is shown in Figure 78. Single preprocessed sample can be used with varying parallel bond properties while changing any of the pair-wise potential parameters requires new preprocessing.

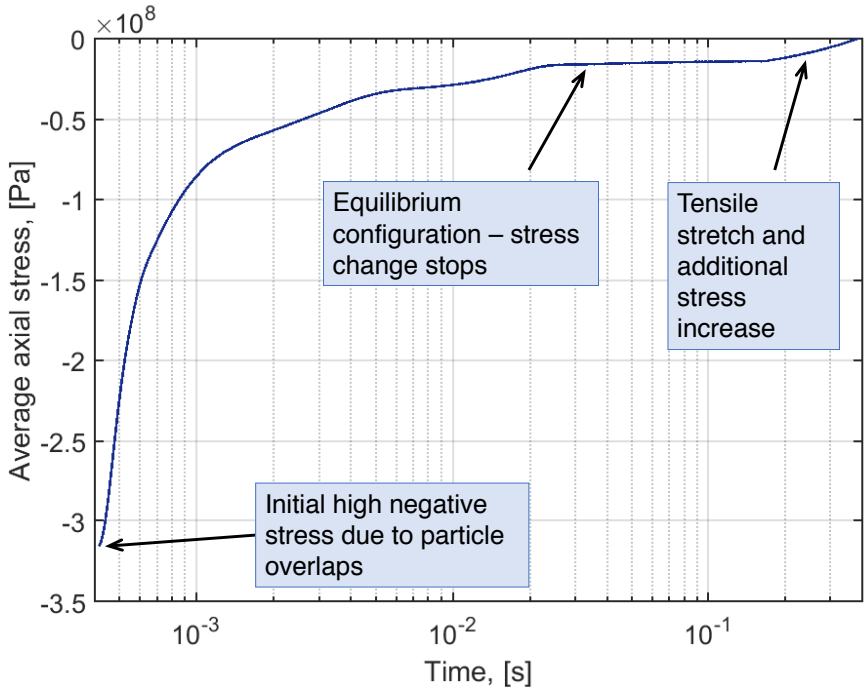

Figure 78. Time evolution of average axial stress during a typical preprocessing simulation.

2.2.7.2.3. Model properties and implementation

Figure 59 shows the assembly used in this work and Table 13 summarizes its properties. The solid fraction of the assembly was $\Phi = 0.60$ which is slightly lower than $\Phi = 0.64$ for a random close packing of monodisperse spheres.

The tensile testing simulation was calibrated to reproduce strain-controlled experimental stress-strain response of tensile testing of a NIMONIC 75 nickel-chromium alloy at high temperature of 600°.

Table 13. Model properties

	Parameters	Value
Elements	Maximum relative element diameter $d_{max}/\bar{d}$	1.0833
	Minimum relative element diameter $d_{min}/\bar{d}$	0.9167
	Element density, kg/m^3	8908.0
Parallel Bonds	Bond modulus, [Pa]	5.926e11
	Normal-to-shear stiffness ratio, []	5.0
	β_n	1e25
	β_s	1.2032e-3
	Gap parameter, [m]	$\bar{d}$
Pair-Wise Potential	Repulsion distance, σ [write over d]	$\frac{12}{13}\bar{d}$
	Potential magnitude parameter, ε [J]	9.3176e4
	Cut-off radius, R_c [over d]	$1.48\bar{d}$
Assembly	Number of elements	15,512
	Initial number of bonds	74,531
	Average coordination number	9.6
	Solid fraction	0.6
	Relative height $H/\bar{d}$	50
	Relative radius of the cylindrical section $R_{cyl}/\bar{d}$	12.5

2.2.7.2.4. Volume change computation

Volume conservation was investigated on three different levels: globally for the cylindrical part of the dog-bone shape assembly, locally for horizontal segments of the whole assembly, and locally for each of the local cages.

Volume change of the cylindrical part was computed from the volume of a three-dimensional tight envelope created from element centroids. The tight envelope yielded slightly better fit than its alternative – convex hull. Volume for later times of the simulation was computed only from the elements originally present in the cylindrical region thus effectively tracking cylinder deformation. In computing the α coefficient (Equation 67), σ_i and ε_i were the global, average, instantaneous axial stress and strain.

Local cage volume change was computed from three-dimensional convex hulls created from vertices of each cage. The vertices were fixed – initial neighbors of the central cage element were used throughout the computation. The strain ε_i in the computation of α coefficient was not changed. This approach provided means for element-wise study of the volume conservation and identification of any patterns of high and low conservation regions.

2.2.7.2.5. Stress-strain response

The rate of DEM deformation was $0.083\bar{d}/s$ and the simulations where repeated with two higher rates, $0.42\bar{d}/s$ and $0.83\bar{d}/s$. Results with all three rates were almost identical and within the experimental uncertainty. Figure 79 shows the stress-strain response compared to three sets of experimental data. Table 14 summarizes elastic and plastic properties from experimental work and numerical simulation. The plastic deformation follows closely the experimental values for all three sets, including the 0.02% offset value and the failure stress and strain (Table 14). On the other hand, the elastic properties display some more discrepancy, particularly with Poisson's ratio being 0.21. While the Young's modulus can be adjusted to a value closer to the experimental one, the Poisson's ratio modifications would likely need improvements to the model itself and its limitations are a common feature of other emerging mesoscopic methods such as peridynamics (Kumar et al., 2016).

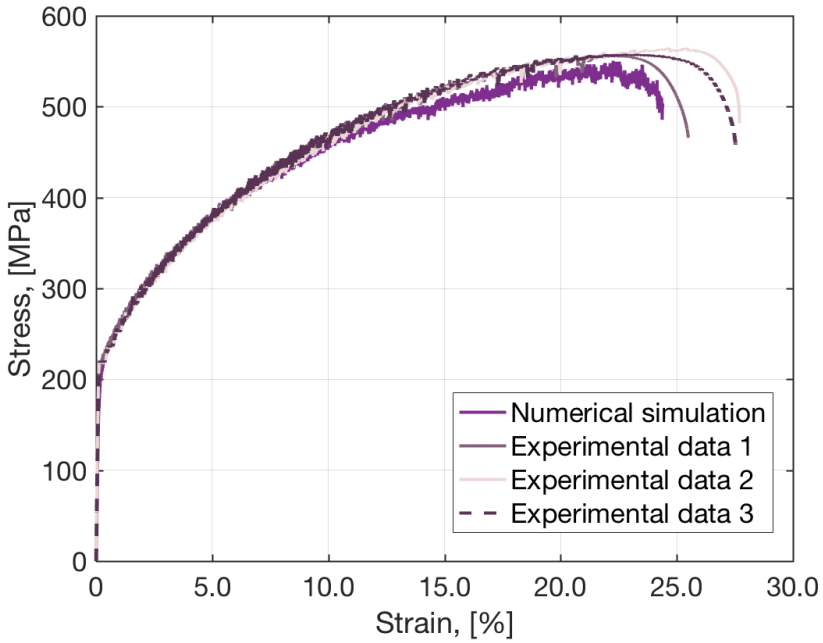

Figure 79. Comparison of experimental and numerical stress-strain responses for tensile testing of NIMONIC 75 at 600°C.

Besides the tensile testing simulations, performed were also the unloading simulations in which the sample was deformed in tension until the desired strain and then subsequently compressed. The unloading modulus (Fig. 80) for each case was computed from a reduced dataset due to the curves non-linearity. The reduction consisted of symmetric trimming of the data points with respect to beginning and end of unloading. The percent of data removed from the dataset for interpolation on each end was fixed for all cases. The unloading stress-strain response shown in Figure 80 had a consistent pattern and the Young's modulus closely matched the one obtained with tensile simulations.

Table 14. Elastic and plastic properties of numerical models compared with experimental data.

Model	Young's modulus, GPa	Yield strength, MPa (0.2%)	Ultimate tensile strength, MPa	Strain to failure, %
Numerical	136.2	222.2	544.2	22.47
Exp 1	194.8	227.9	554.9	23.11
Exp 2	198.8	218.5	562.8	25.79
Exp 3	200.2	218.3	554.6	24.38

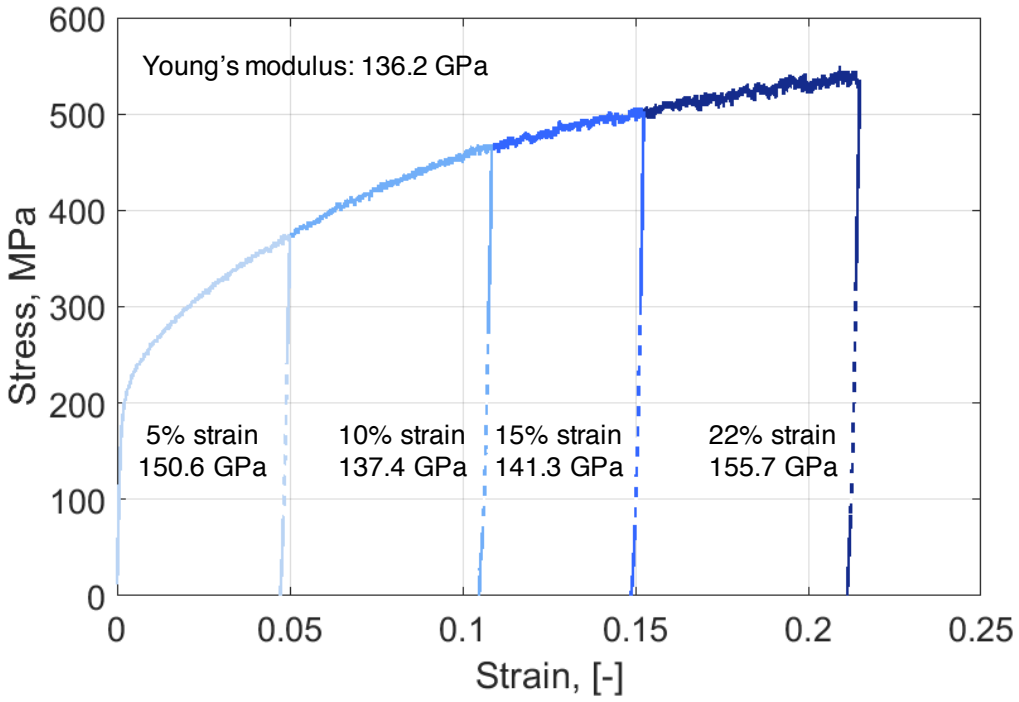

Figure 80. Stress-strain curves for the unloading simulations and the corresponding moduli. The sample was first stretched in tension until the indicated strain and then compressed to zero average stress. The dashed lines represent the interval over which the unloading moduli were obtained with a linear fit.

2.2.7.2.6. Deformation analysis

Figure 81 shows the results of the d_{2min} analysis. During the earlier stages of plastic deformation, the central region of the sample has low d_{2min} values thus the deformation is closer to continuum. In the near-failure stages the d_{2min} analysis indicates the position of the fracture with better agreement with continuum below the fracture.

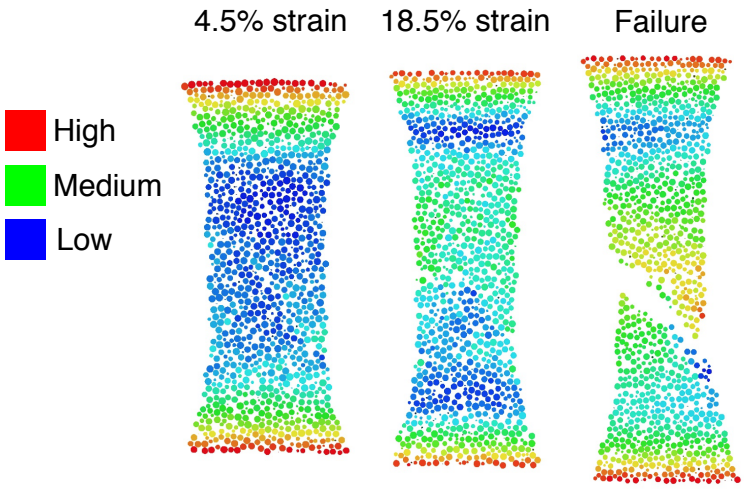

Figure 81. Results of the d_{2min} analysis in the central cross-sections of the assembly at different strains and at failure.

Results of local cage deformation analysis are shown in Figure 82 revealing localization of deformation on shear bands. The shear bands were visualized by highlighting the elements with local cage deformation values higher than 2.0-2.3 times the assembly mean. The angles of shear bands and the fracture were obtained through three-dimensional fitting of a plane and are also indicated. The fracture angle of 40° is within the range of fracture angles of NIMONIC 75.

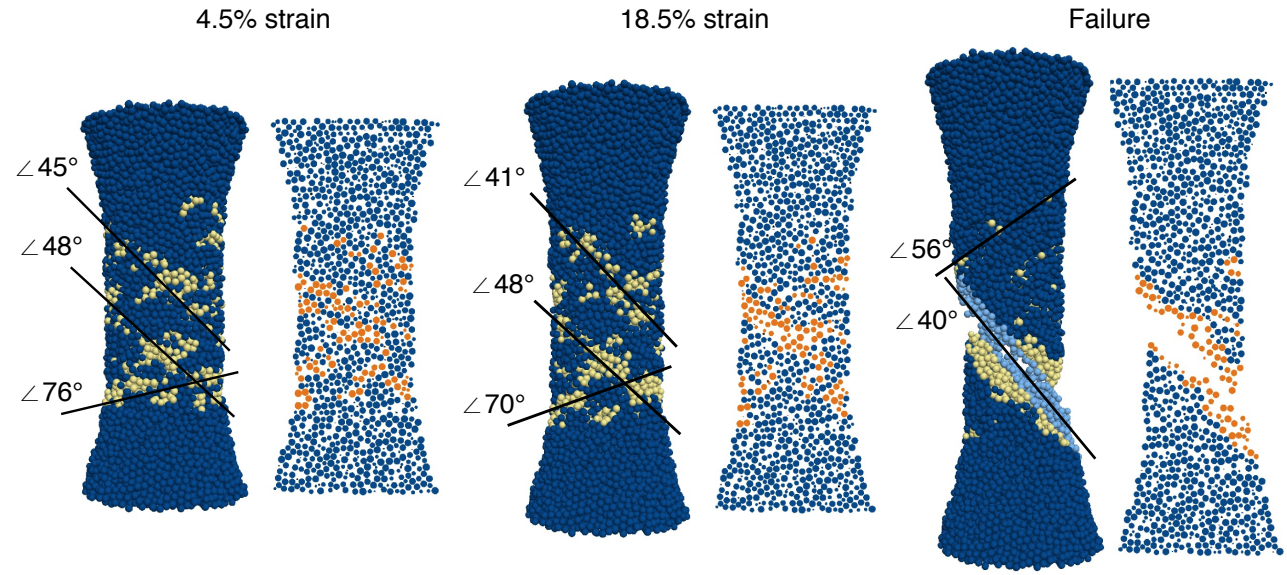

Figure 82. Results of the local cage deformation analysis in the assembly and its central cross-sections at different strains and at failure. Gold/orange indicates cage deformation values more than two times larger than the mean. Light blue indicates the particles surrounding the fracture.

2.2.7.2.7. Volume conservation

The results of volume conservation analysis are shown in Figure 83. Even though the cylindrical region visibly contracts (Figure 83a), reduction in cross-sectional area does not compensate for assembly elongation and the volume is not conserved (Figure 83b).

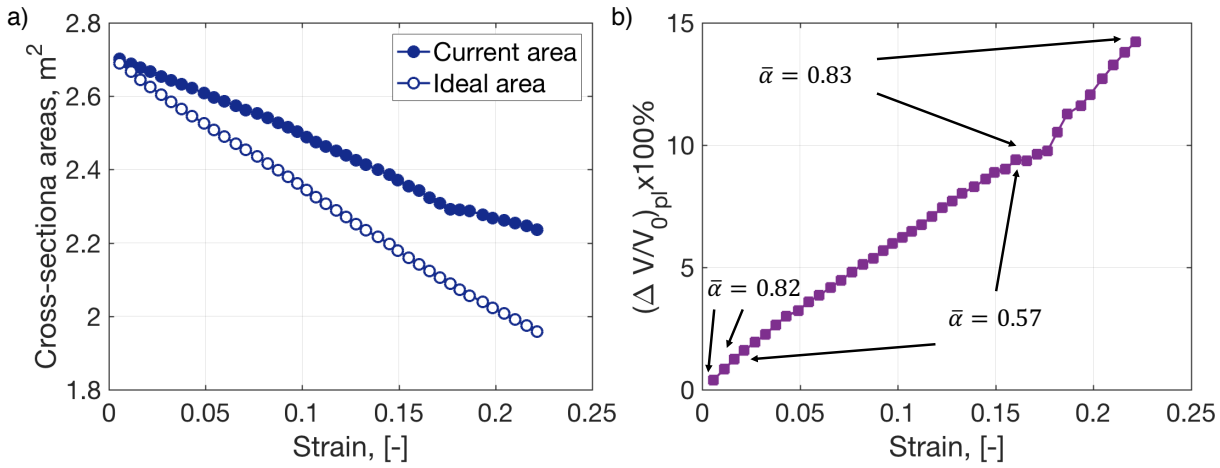

Figure 83. a) Ideal vs. current cross-sectional area of the cylindrical region in Figure 59. b) Plastic volume conservation as a function of axial strain with α coefficients obtained through linear interpolation of indicated intervals.

Figure 84 shows elements with volume change that is twice higher than the assembly mean. As expected, volume change is higher towards the interior of the assembly and lowest in the grip region. At the same time, high volume change seems to be only partially aligned with the shear bands shown in Figure 82.

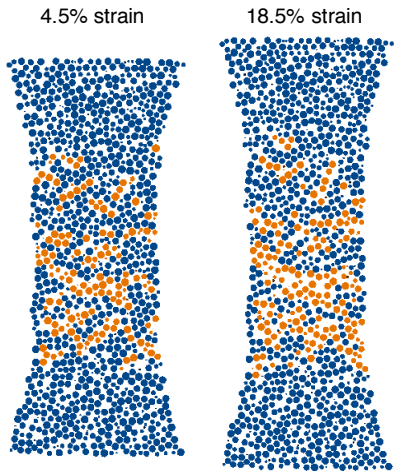

Figure 84. Orange elements have their local cage volume change twice larger than the assembly mean.

2.2.7.2.8. Interaction between parallel bond force and the pair-wise potential

Figure 85 shows schematic interaction between two bonded elements A and B in tension and compression with deformation parallel to the contact normal and with no pair-wise potential. By convention, the contact force results from element A acting on element B (Potyondy and Cundall, 2004). Similarly, the parallel bond force is the action of the parallel bond on element B (Potyondy and Cundall, 2004). This implies that if the bond is in tension, the force on element B is negative and the two elements attract each other. On the other hand, in compression, the force on element B is positive and there is repulsion between elements A and B. The consequence of this is that elements slipping past each other experiencing local compression will be accompanied by element repulsion and a tendency to form cracks or voids quickly on slip bands.

The presence of a supplementary pair-wise potential significantly changes this scenario. Following the convention outlined in section 2.2.7.2.1, for elements in close proximity the pair-wise potential on element B in both tension and compression will result in a negative force thus introducing attraction between the two elements. This not only provides additional tensile deformation resistance, but also promotes slip without easy crack or void formation since it hinders the repulsion introduced by the parallel bond during compressive phases of local deformation.

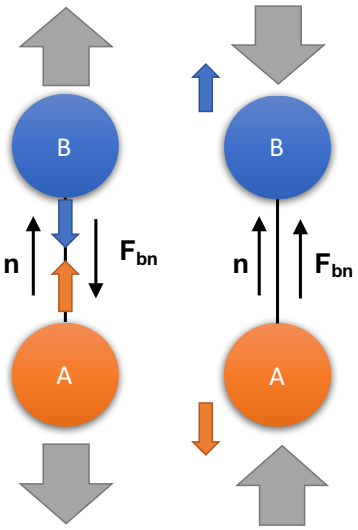

Figure 85. Parallel bond forces in tension (left) and compression (right). Parallel bond introduces attraction in tension and repulsion in compression.

2.2.7.2.9. Hardening mechanism

There are three major sources of hardening in this work - unbounded normal parallel bond force, contact reorientation, and the pair-wise potential.

The unbounded normal force on parallel bonds is a consequence of constraining the bond failure exclusively to failure in shear. The constraint, imposed by setting the normal strength of the bond to unphysically large values, causes the bonds force to develop continuously until the shear stress exceeds that bonds shear strength (Equation 56 - Equation 57). Only when the bond breaks in shear and is being reformed is the normal force on it reset to 0.0. Both normal and shear forces are reset to 0.0 and the bond is excluded from the computations if bonds gap exceeds the gap cutoff parameter (Equation 8). If the bond orientation is such that the shear force does not develop very rapidly or almost at all, the normal force will be able grow considerably until its reset to 0.0 following bond breakage in shear or the bond becomes longer than the threshold and becomes inactive. This process of load transfer to bonds aligned in strong directions is the major source of hardening in this work, by far exceeding the latter two. Furthermore, it is even more supported due to the deformation direction being aligned with bonds which shear force is underdeveloped – in this case the vertical bonds. Figure 86 shows the stress-strain response of assemblies with no pair-wise potential and three different maximum gap parameters. Except the response for the smallest parameter, the stress-strain responses undergo hardening and the responses are very linear which originates from linear nature of the force-displacement law. The maximum strains are much higher in the later cases than for the shortest bond case and allow

bonds to elongate in the vertical, deformation direction while developing a high normal force due to negligible shear force increase.

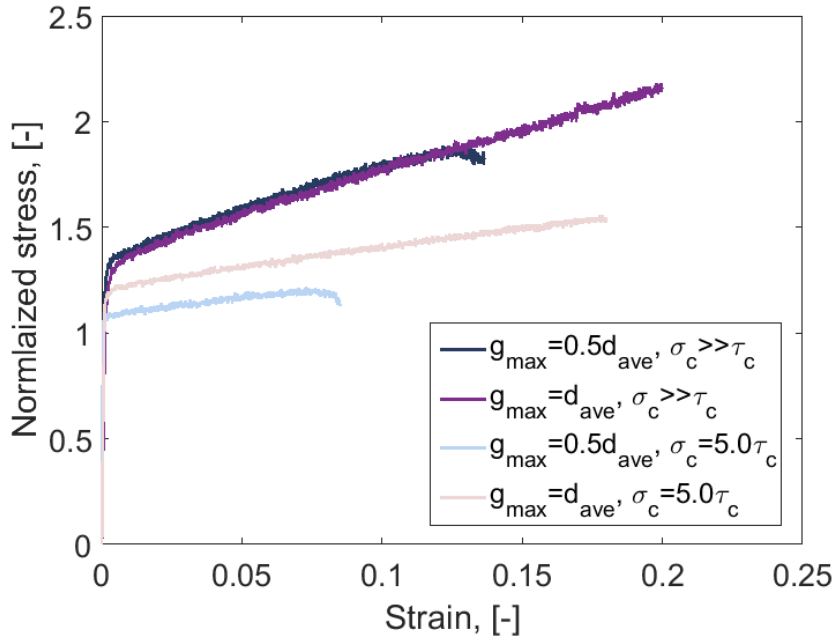

Figure 86. Stress-strain response for two different gap cutoff parameters in simulations without the pair-wise potential for cases with high bond normal strength and a normal strength five times larger than the shear strength. Stress was normalized by the stress value at the yield point.

Defining hardening per bond as positive normal force time derivative, 50.6% of total bonds harden at the end of the tensile testing simulation, just before failure. Out of these 50.6%, 68.5% have bond breakage frequency lower than the assembly mean in the last third of the plastic deformation and 47.6% have breakage frequency lower than a quarter of the mean. This indicates a direct correlation between the increasing normal force that induces macroscopic hardening response and the lower bond breakage. Looking at the whole assembly, 68% of all bonds have the breakage frequency lower than the mean signifying that not all the bonds with less frequent breakage develop high normal force and contribute to hardening. This is a consequence of heterogeneous nature of the assembly and bond orientation as different bonds carry varying amounts of force. Similarly, not all the hardening bonds are oriented in the deformation direction, meaning that their normal forces do not directly contribute to the axial stress.

Figure 86 shows the results of setting the normal strength of the bonds to values comparable to shear strength using a bond stiffness dependent expression (Equation 62). The resulting hardening rates are considerably lower than in the cases with high normal strength. This confirms that the main source of hardening in the model was the high normal force originating from practically unconstrained normal strength.

The second, though less impactful source of hardening is contact reorientation. Figure 87 shows best-fit spherical harmonics to the 3D histograms of contact orientation, contact normal force, and contact shear force. During the simulation, contact orientation changes from near isotropic to anisotropic and vertically oriented. This is not surprising, given that contacts align themselves with deformation direction. Figure 88 shows the normalized time evolution of anisotropy of

contact orientation, which again confirms the transition to vertical alignment. On the other hand, based on the 3D histograms, the normal and shear forces do not change their dominant direction and anisotropy greatly, although based on the values in Figure 88 the changes are still considerable.

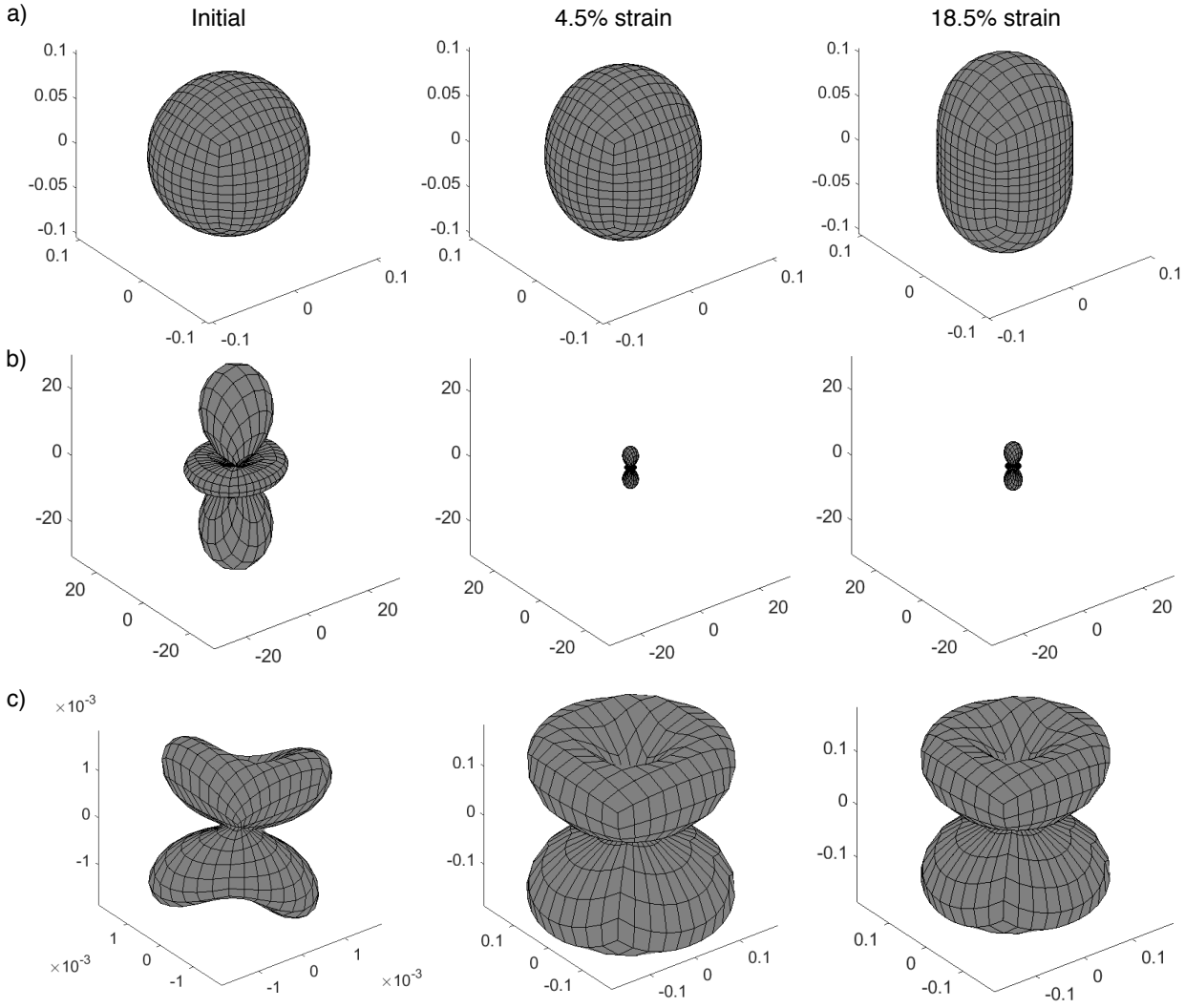

Figure 87. Fits of the 3D histograms of a) contact orientation, b) normal and c) shear forces at the beginning of the simulation and at two different strains. Note scale change from left to right in (c).

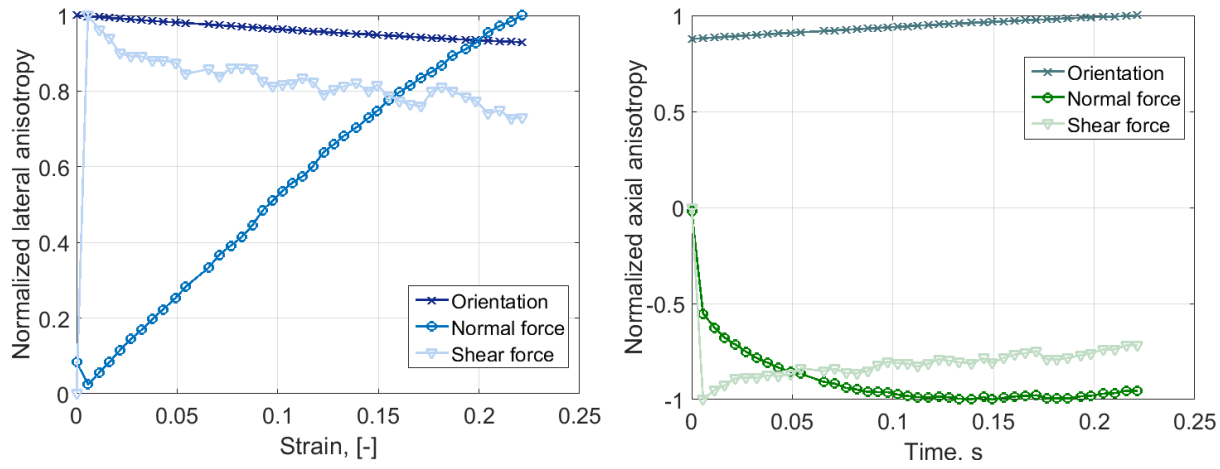

Figure 88. Evolution of lateral (left) and axial (right) normalized anisotropy in fitted 3D histograms for contact orientation, normal force, and shear force.

Finally, a minor hardening contribution comes also from the shape of the pair-wise potential (Figure 77) which induces non-linear element interaction but also slight well-shaped increase of force after the initial linear region. This is the same mechanism as described in section 2.2.7.2.8.

2.2.7.2.10. Calibration

The proposed model has a number of calibration parameters that must be considered collectively for any given material. Meanwhile, there exist certain trends in the calibration process as well as in the model itself that should considerably reduce the parameter fitting procedure.

The primary feature of the model relevant to calibration is that the parallel bonds and pair-wise potential are treated as independent entities. The amount of each may range from none to any value by setting their relative magnitudes, bond stiffnesses and pair-wise potential magnitude factor ε (Equation 72). In this work the influence of this relative contribution was measured with the average ratio of average pair-wise potential and bond force.

When no pair-wise potential was present, the stress-strain response was purely linear as in Figure 86 and Figure 89. Hardening occurs for larger maximum gap parameters (Equation 8) and normal bond strength higher than shear strength (Equation 62).

The pair-wise potential introduced non-linearity to the stress-strain response. As shown in Table 15, even a small amount of the pair-wise potential considerably affected the maximum strain. Larger contribution of the pair-wise potential lead to higher Poisson's ratios while the maximum strain reached would decrease. The yield strain tended to remain constant though the yield stress decreased with increasing pair-wise potential influence.

The pure pair-wise potential case displayed a bell-shape stress-strain response as shown in Figure 89. The large contributions of pair-wise potential in the model shift the stress-strain response from the linear parallel bond-dominated to a bell-shaped, potential-dominated one. Large contribution of the pair-wise potential caused deviations from linear elastic behavior and significant shifts in yield strain towards higher, unphysical values. At the same time with increasing potential influence the Poisson's ratio values become higher and closer to values consistent with those observed in physical tests of metals.

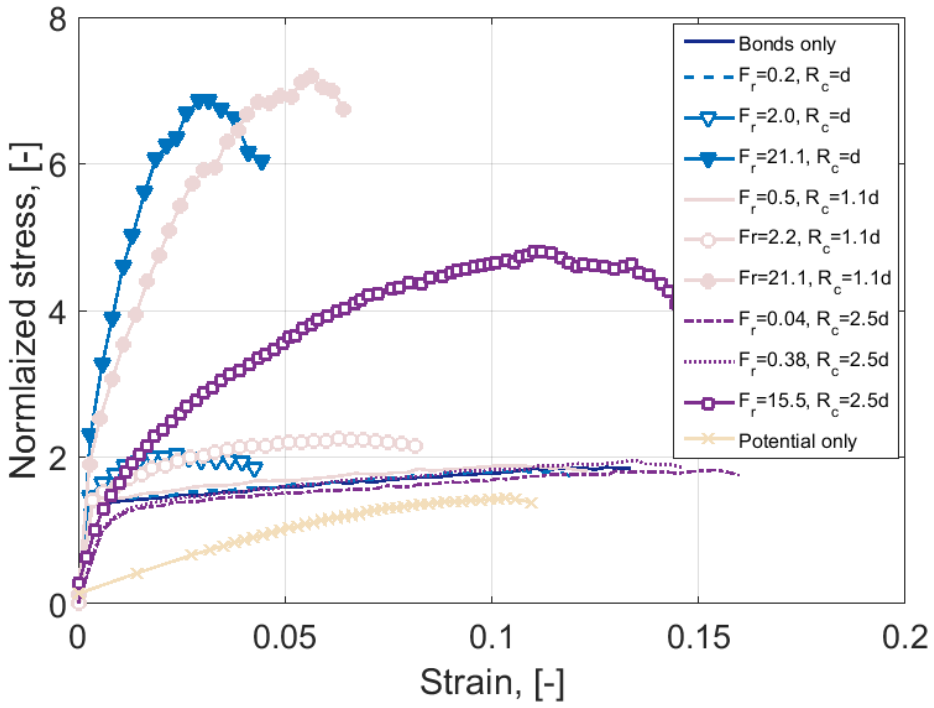

Figure 89. Normalized stress-responses for models with different contribution of pair-wise potential, F_p, to parallel bond, F_b, force ($F_r=F_p/F_b$) and pair-wise potential cut-off radius R_c (in terms of mean element diameter d). The gap cut-off parameter in the calibration models equaled $0.5\bar{d}_{ave}$.

Table 15. Elastic and plastic properties of models with different model parameters. Stress-strain curves for all models are shown in Figure 50. The gap cut-off parameter in the calibration models equaled $0.5\bar{d}_{ave}$.

ID	F_p/F_b	$R_c, \bar{d}_{ave}$	E, GPa	υ	ε_Y, %	σ_Y, MPa	ε_{max}, %	σ_{max}, MPa
1	0.0	0.0	130.9	0.23	0.06	72.6	12.7	136.7
2	0.2	1.0	130.2	0.15	0.05	74.6	11.4	135.2
3	2.0	1.0	144.9	0.16	0.05	74.9	3.8	147.1
4	21.1	1.0	140.8	0.17	0.05	68.6	3.5	450.5
5	0.5	1.1	124.4	0.17	0.06	76.2	11.6	143.9
6	2.2	1.1	144.9	0.22	0.05	75.9	8.0	164.6
7	21.1	1.1	120.5	0.17	0.05	67.8	6.0	479.5
8	0.04	2.5	137.0	0.18	0.60	801.2	15.1	1430
9	0.38	2.5	145.3	0.18	0.50	772.6	13.6	1549
10	15.5	2.5	192.7	0.29	0.40	964.6	13.3	4503
11	1.0	2.5	0.8	0.31	5.0	45.9	11.0	61.1

As shown in Figure 89 and Table 15, the most viable potential to bond force ratios fall in the range of 0.1 to less than 10.0. These ratios introduce desired non-linearity while maintaining

linearity of the elastic region. In practice, the case with no potential can serve as the first calibration guideline as tuning the bond properties approximately determines the maximum stress and strain reached as well as elastic properties of the sample. Further addition of the potential will influence the plastic response depending on potential magnitude and maximum interaction distance, R_c (Equation 72-Equation 73). Selecting different R_c values allows for variable influence of the potential during the later stages of plastic deformation. Smaller R_c values will cause the potential to become negligible in the earlier stages of plasticity while larger will maintain its influence until failure. This has a clear influence on the stress-strain response, leaving the later part of plastic response more linear in cases with lower R_c values as shown in Figure 90. For any amount of potential influence, care must be taken that the bond strengths are high enough to not fail in the elastic region. Once calibrated, the stress-strain response can be scaled by proportionally changing the parallel bond stiffnesses and potential magnitude. If the bond strengths are independent of bond stiffnesses, these also need to be scaled accordingly.

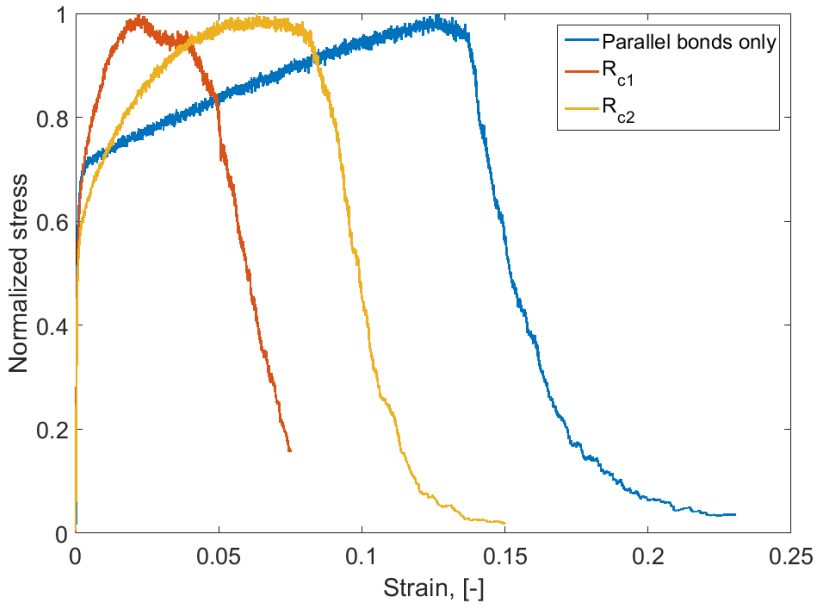

Figure 90. Normalized stress-responses for models with different R_c cutoff values compared to the model with parallel bonds only.

2.2.7.2.11. Choice of assembly size

An important component of discrete element modeling is establishing the number of elements needed for the *minimum representative volume* (MRV). MRV represents the smallest number of elements that collectively act as a continuum. Determination of MRV commonly proceeds by increasing the number of elements until some chosen volume-averaged metric does not change significantly with further size increase. The MRV is then chosen as the smallest set of elements with such response.

Figure 91 shows the stress-strain response of assemblies with four different sizes, including the one used in this work and Table 16 shows their properties. The overall response is somewhat similar for all four assemblies while the oscillations decrease with increasing assembly size. The final strain reached before failure increases considerably for the smallest assembly. The largest assembly has almost identical stress-strain response as the smaller one used here. Even though

the response is smoother in the larger assembly, given the matching of the stress-strain curves and doubled computational load, it is justifiable to use the smaller assembly except if higher accuracy is needed.

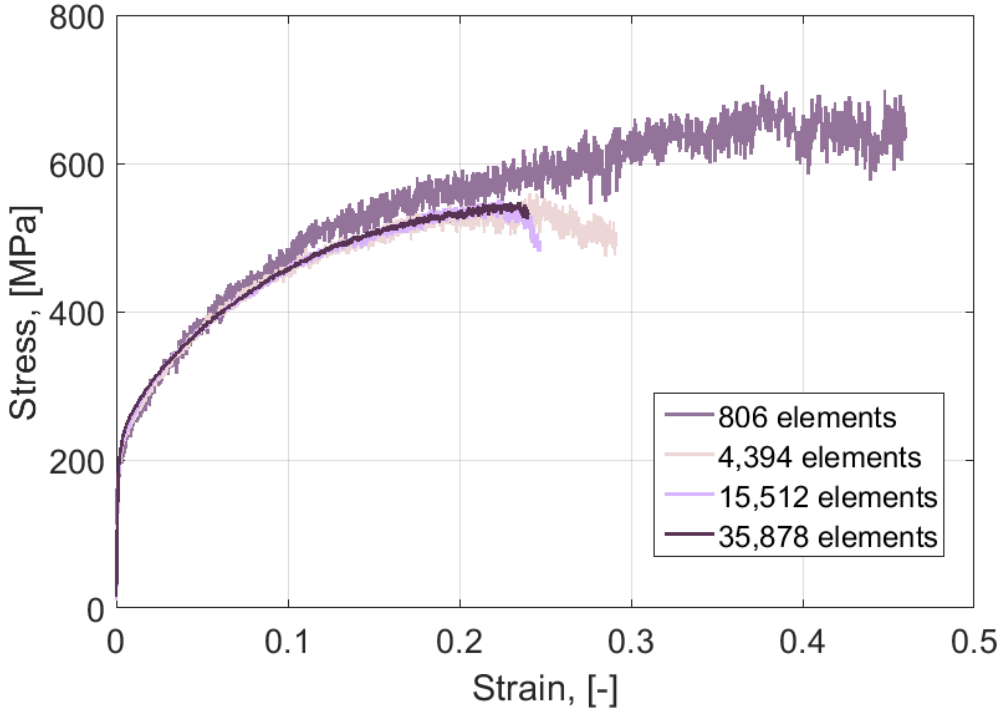

Figure 91. Stress-strain response of assemblies with different number of elements.

Based on the elastic properties of the four assemblies summarized in Table 16, the properties in the 806 and 4,394 elements assemblies vary considerably from the larger assemblies and their Poisson's ratios are not reliable. The match in for the current and the larger assembly is not as close as in the case of the plastic stress-strain response. As shown in Section 5.2.10 the deviation in the elastic properties, especially the Poisson's ratio is a property of this model. As it is, the model is suited for plastic deformation with elasticity being regarded only in an approximate sense.

Table 16. Elastic and plastic properties of models with different number of elements compared to the original model.

Number of elements	E, GPa	υ_{xx}	υ_{yy}	υ	ε_Y, %	σ_Y, MPa	ε_{max}, %	σ_{max}, MPa
806	117.4	-0.04	0.08	0.02	0.06	160.7	46.0	639.2
4,394	172.8	0.32	0.48	0.40	0.07	133.3	29.1	510.3
15,512	136.2	0.23	0.18	0.21	0.1	162.1	22.5	544.2
35,878	151.5	0.18	0.18	0.18	0.08	131.1	23.6	539.5

2.2.7.2.12. Reproducibility with different assemblies

The reproducibility of the model was verified with three additional models generated with different random seeds. The plastic stress-strain response of the models compared to the original model are shown in Figure 92 and the elastic properties in Table 17. While the plastic stress-strain response in all the cases is almost identical, the elastic properties vary considerably.

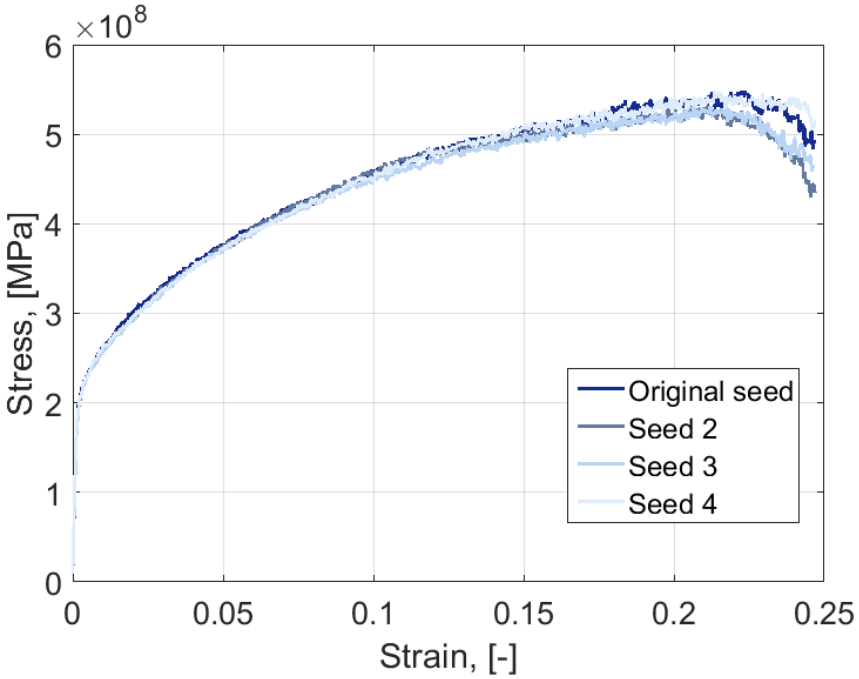

Figure 92. Stress strain response of the assemblies generated with different random seeds compared to the original assembly.

Table 17. Elastic properties of the original model and the models formed with three different random seeds. The "large" refers to largest model used as described in Section 2.2.7.2.11. These are all interpolated over a fixed interval.

	Young's modulus [GPa]	**Poisson's ratio in xx direction [-]**	**Poisson's ratio in yy direction [-]**	**Mean Poisson's ratio [-]**
Original seed	136.2	0.23	0.18	0.21
Seed 2	129.9	0.1	0.1	0.1
Seed 3	121.1	0.13	0.27	0.20
Seed 4	142.6	0.11	0.14	0.12
Original seed, large	151.5	0.18	0.17	0.18
Seed 2, large	142.1	0.18	0.19	0.19
Seed 3, large	139.0	0.22	0.19	0.21
Seed 4, large	135.5	0.17	0.13	0.15

A characteristic feature of these models is occasional higher anisotropy between the Poisson's ratio in the two lateral directions, here xx and yy. This size-dependent discrepancy diminishes in the larger assemblies, also shown in Table 17, but the value does not necessary become similar for all tested seeds. Both the Young's modulus and the Poisson's ratio seem to fall into a range of values with a deviation that lessens with the assembly size.

Figure 94 shows some of the data and linear fits used to obtain the elastic properties. While the data is linear for the Young's modulus, Poisson's ratio is often obtained from a considerably more oscillatory dataset. This is likely a consequence of both the discrete nature of the assembly and the presence of a pair-wise potential that varies with absolute distance rather than incrementally reaching higher force values initially starting from zero for all the elements. Again, the proposed model is suitable for simulation of materials plastic response and its elastic properties should be used in an approximate sense, considering that they are represented by intervals rather than single values. As shown in Figure 94, the datasets used for obtaining the elastic properties are considerably more linear in case of larger assemblies. The properties for larger assemblies shown in Table 17 also display smaller deviation. This indicates that elastic behavior of our DEM model needs a larger minimum representative volume than the plasticity simulations. This finding is expected since elasticity is characterized by smaller displacement and thus needs larger resolution for quantification of these changes.

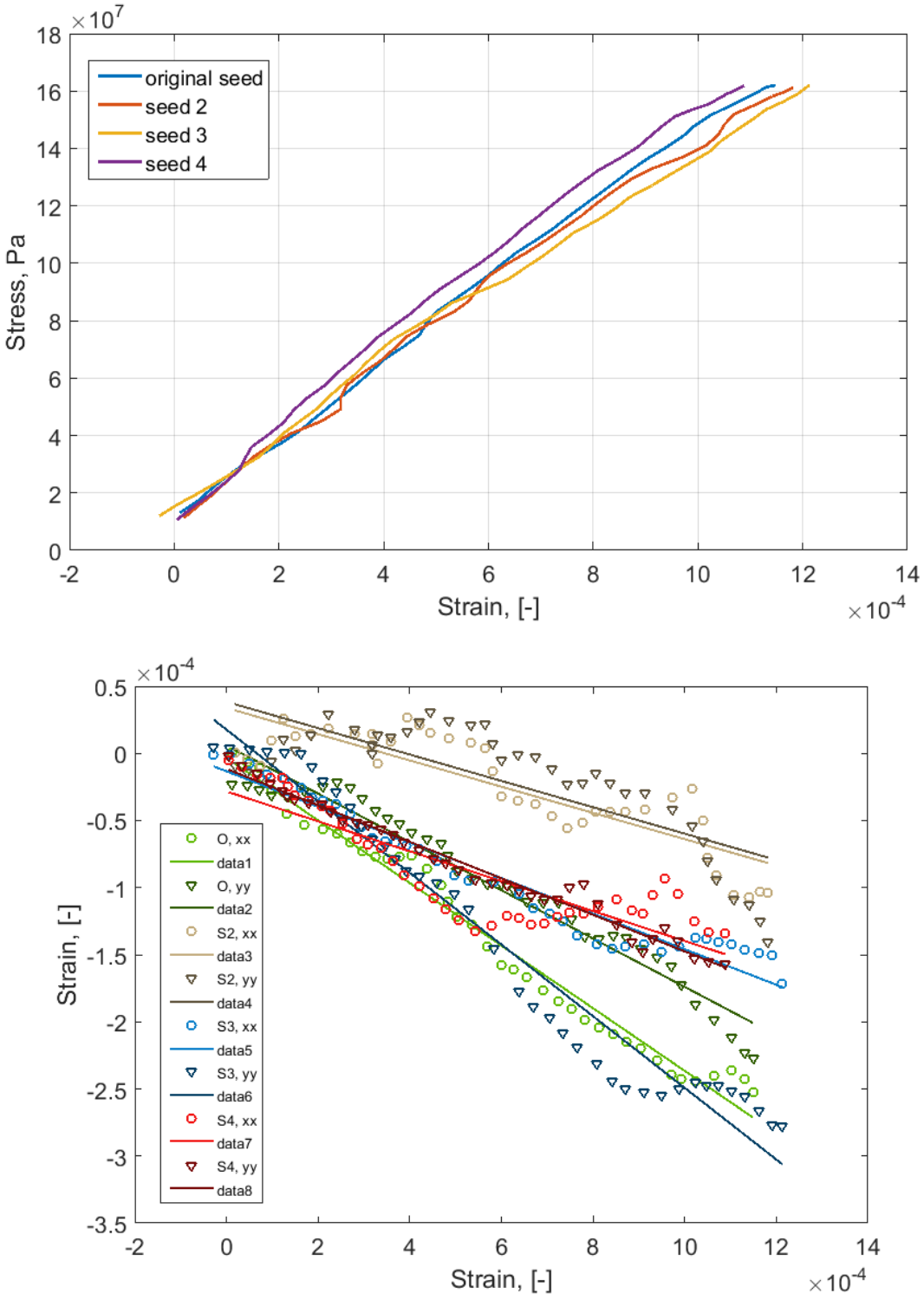

Figure 93. Elastic property fits for all four seeds in regular size models. The Poisson ratio plots show datapoints as markers and fits as lines. O is the original seed and S with number indicates the random seed. Fitting was performed in both lateral directions – xx and yy as indicated.

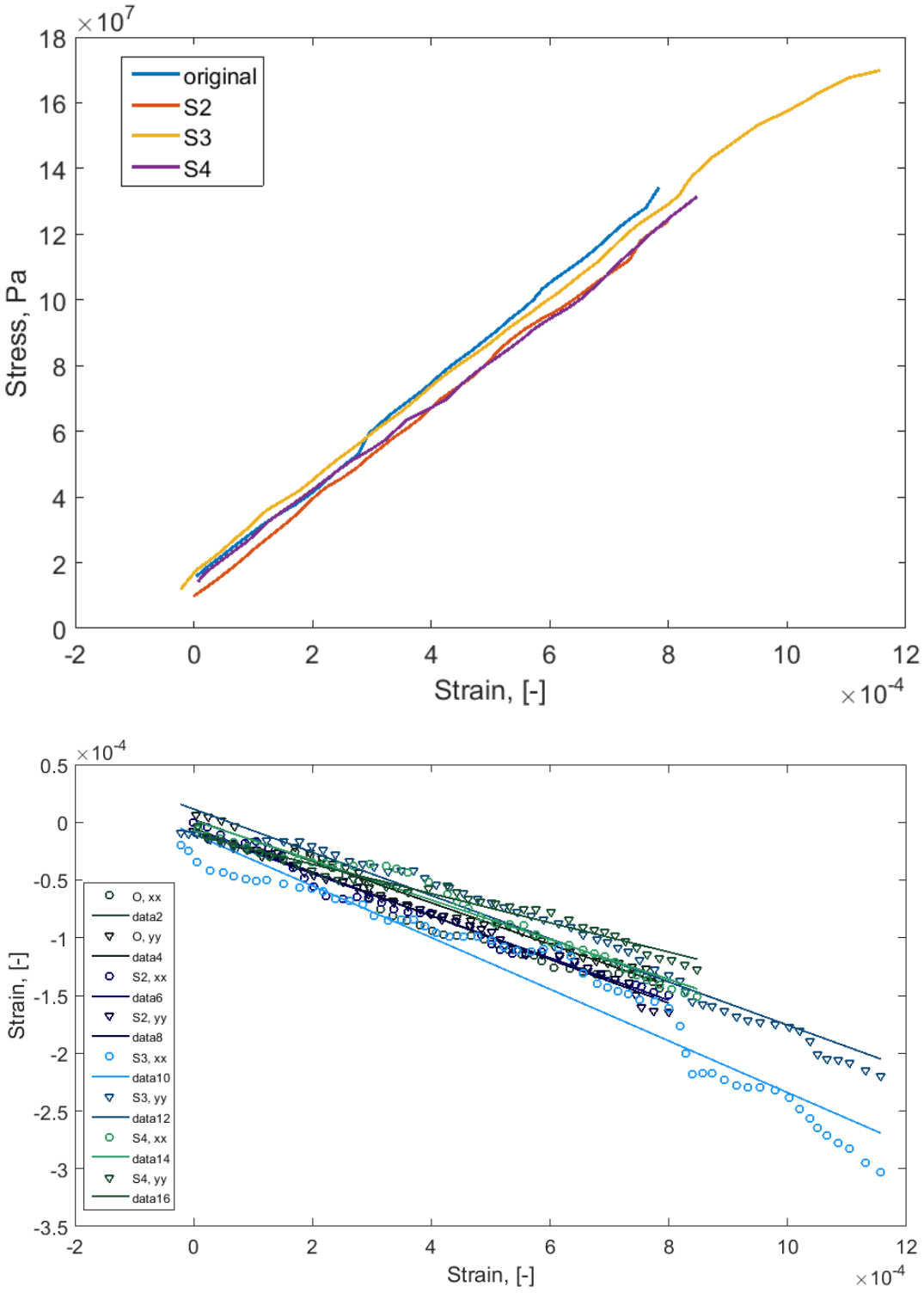

Figure 94. Elastic property fits for all four seeds in large models. The Poisson ratio plots show datapoints as markers and fits as lines. O is the original seed and S with number indicates the random seed. Fitting was performed in both lateral directions – xx and yy as indicated.

3. Products

Submitted Manuscripts (Several more are in preparation):

1. A. Truszkowska, P. A. Greaney, T. M. Evans, J. J. Kruzic, "Simulating Isotropic Non-Hardening Plasticity using the Discrete Element Method," in review.

Published Manuscripts:

1. A. Truszkowska, Q. Yu, P. A. Greaney, T. M. Evans, J. Kruzic, "Developing a Crystal Plasticity Model for Metallic Materials Based on the Discrete Element Method," *MRS Advances*, 2017, , **2** (48) 2609-2614. https://doi.org/10.1557/adv.2017.430.

2. A. Truszkowska, Q. Yu, P. A. Greaney, T. M. Evans, J. J. Kruzic, "A Discrete Element Method Representation of an Anisotropic Elastic Continuum," *Journal of the Mechanics and Physics of Solids*, 2018, accepted and in press.

Oral Presentations:

1. A. Truszkowska, Q. Yu, T. M. Evans, P. A. Greaney, J. J. Kruzic, "Developing a Crystal Plasticity Model for Nickel Based Turbine Alloys Based on the Discrete Element Method," Materials Science & Technology 2017, Pittsburgh, PA, October, 2017.

2. A. Truszkowska, Q. Yu, P. A. Greaney, T. M. Evans, J. J. Kruzic, "Developing a Crystal Plasticity Model for Nickel Based Turbine Alloys Based on the Discrete Element Method," 2017 MRS Spring Meeting, Phoenix, AZ, April 2017.

3. Invited: P. A. Greaney, J. J. Kruzic, A. Truszkowska, Q. Yu, T. M. Evans, "New Mechanistic Models of Long Term Evolution of Microstructure and Mechanical Properties of Nickel Based Alloys" NETL Crosscutting Review Meeting, Pittsburgh, PA, April 2017.

4. Invited: J. J. Kruzic, A. Truszkowska, Q. Yu, P. A. Greaney, T. M. Evans, "Developing a Crystal Plasticity Model for Nickel Based Turbine Alloys Based on the Discrete Element Method," Materials for Coal-Based Power Symposium, Energy Materials 2017, San Diego, CA, February 2017.

5. A. Truszkowska, Q. Yu, P. A. Greaney, T. M. Evans, J. J. Kruzic, "Developing a Crystal Plasticity Model Based on the Discrete Element Method," Materials Science & Technology 2016, Salt Lake City, UT, October, 2016.

6. Invited: J. J. Kruzic, T. M. Evans, P. A. Greaney, "New Mechanistic Models of Long Term Evolution of Microstructure and Mechanical Properties of Nickel Based Alloys" NETL Crosscutting Review Meeting, Pittsburgh, PA, April 2016.

Poster Presentations:

1. Invited: J. J. Kruzic, T. M. Evans, P. A. Greaney, Q. Yu, A. Truszkowska, "Discrete element method for deformation and microstructure evolution modeling," NETL Crosscutting Review Meeting, Pittsburgh, PA, April 2015.

4. References

Akhtar, A., Teghtsoo.E, 1971. Plastic Deformation of Ni-Cr Single Crystals. Metall. Trans. 2, 2757-2763.

Anand, L., Su, C., 2005. A theory for amorphous viscoplastic materials undergoing finite deformations, with application to metallic glasses. J Mech Phys Solids 53, 1362-1396.

Belheine, N., Plasslard, J.P., Donze, F.V., Darve, F., Seridi, A., 2009. Numerical simulation of drained triaxial test using 3D discrete element modeling. Comput. Geotech. 36, 320-331.

Betteridge, W., Heslop, J., 1974. The Nimonic Alloys and Other Nickel-Base High-Temperature Alloys, 2nd ed. Crane, Russak, & Company, Inc., New York, p. 498.

Cundall, P.A., 1971. A computer model for simulating progressive, large-scale movements in blocky rock systems, Proceedings of the International Symposium on Rock Mechanics, Nancy, France, pp. 129–136.

Cundall, P.A., Strack, O.D.L., 1979. Discrete Numerical-Model for Granular Assemblies. Geotechnique 29, 47-65.

da Cruz, F., Emam, S., Prochnow, M., Roux, J.N., Chevoir, F., 2005. Rheophysics of dense granular materials: Discrete simulation of plane shear flows. Phys. Rev. E 72.

Ding, J., Cheng, Y.Q., Ma, E., 2014. Full icosahedra dominate local order in Cu64Zr34 metallic glass and supercooled liquid. Acta Mater. 69, 343-354.

Dmowski, W., Iwashita, T., Chuang, C.P., Almer, J., Egami, T., 2010. Elastic Heterogeneity in Metallic Glasses. Phys. Rev. Lett. 105.

Dolbow, J., Moes, N., Belytschko, T., 2001. An extended finite element method for modeling crack growth with frictional contact. Comput. Meth. Appl. Mech. Eng. 190, 6825-6846.

Evans, T.M., Frost, J.D., 2007. Shear Banding and Microstructure Evolution in 2D Numerical Experiments, Advances in Measurement and Modeling of Soil Behavior, p. GSP 173.

Evans, T.M., Lee, J., Yun, T.S., Valdes, J.R., 2011. Thermal Conductivity in Granular Mixtures: Experimental and Numerical Studies. Deformation Characteristics of Geomaterials, Pts 1 and 2, 815-820.

Fu, X.Y., Falk, M.L., Rigney, D.A., 2001. Sliding behavior of metallic glass - Part II. Computer simulations. Wear 250, 420-430.

Furukawa, A., Tanaka, H., 2009. Inhomogeneous flow and fracture of glassy materials. Nature Mater. 8, 601-609.

Gao, M., Wang, C., Dong, J., Huan, Y., Bai, H.Y., Wang, W.H., 2016. Macroscopic tensile plasticity of Zr-based bulk metallic glass with surface screw thread shaped structure. Mater. Sci. Eng. A-Struct. Mater. Prop. Microstruct. Process. 673, 417-422.

Gould, D., Loveday, M., 1990. The Certification of Nimonic 75 Alloy as a Creep Reference Material. Commission of the European Communities, Directorate-General Science, Research and Development.

Greer, A.L., Cheng, Y.Q., Ma, E., 2013. Shear bands in metallic glasses. Mat Sci Eng R 74, 71-132.

Ha, Y.D., Bobaru, F., 2011. Characteristics of dynamic brittle fracture captured with peridynamics. Eng. Fract. Mech. 78, 1156-1168.

Hufnagel, T.C., Schuh, C.A., Falk, M.L., 2016. Deformation of metallic glasses: Recent developments in theory, simulations, and experiments. Acta Mater. 109, 375-393.

Ingelbrecht, C., Loveday, M., 2000. The Certification of Ambient Temperature Tensile Properties of a Reference Material for Tensile Testing According to EN 10002-1. Commission of the European Communities, Directorate-General Science, Research and Development.

Jebahi, M., Andre, D., Dau, F., Charles, J.L., Iordanoff, I., 2013. Simulation of Vickers indentation of silica glass. J. Non-Cryst. Solids 378, 15-24.

Ketov, S.V., Sun, Y.H., Nachum, S., Lu, Z., Checchi, A., Beraldin, A.R., Bai, H.Y., Wang, W.H., Louzguine-Luzgin, D.V., Carpenter, M.A., Greer, A.L., 2015. Rejuvenation of metallic glasses by non-affine thermal strain. Nature 524, 200-203.

Kocks, U.F., Mecking, H., 2003. Physics and phenomenology of strain hardening: the FCC case. Prog. Mater. Sci. 48, 171-273.

Kumar, R., Rommel, S., Jauffres, D., Lhuissier, P., Martin, C.L., 2016. Effect of packing characteristics on the discrete element simulation of elasticity and buckling. Int J Mech Sci 110, 14-21.

Li, B.S., Shahabi, H.S., Scudino, S., Eckert, J., Kruzic, J.J., 2015. Designed heterogeneities improve the fracture reliability of a Zr-based bulk metallic glass. Mater. Sci. Eng. A-Struct. Mater. Prop. Microstruct. Process. 646, 242-248.

Liu, Y.H., Wang, D., Nakajima, K., Zhang, W., Hirata, A., Nishi, T., Inoue, A., Chen, M.W., 2011. Characterization of Nanoscale Mechanical Heterogeneity in a Metallic Glass by Dynamic Force Microscopy. Phys. Rev. Lett. 106.

Lund, A.C., Schuh, C.A., 2003. Yield surface of a simulated metallic glass. Acta Mater. 51, 5399-5411.

Madenci, E., Oterkus, E., 2016a. Peridynamic theory and its applications. Springer.

Madenci, E., Oterkus, S., 2016b. Ordinary state-based peridynamics for plastic deformation according to von Mises yield criteria with isotropic hardening. J. Mech. Phys. Solids 86, 192-219.

Mehl, M.J., Osburn, J.E., Papaconstantopoulos, D.A., Klein, B.M., 1990. Structural properties of ordered high-melting-temperature intermetallic alloys from first-principles total-energy calculations. Phys Rev B Condens Matter 41, 10311-10323.

Militzer, M., Sun, W.P., Jonas, J.J., 1994. Modeling the Effect of Deformation-Induced Vacancies on Segregation and Precipitation. Acta Metall. Mater. 42, 133-141.

Murali, P., Guo, T.F., Zhang, Y.W., Narasimhan, R., Li, Y., Gao, H.J., 2011. Atomic Scale Fluctuations Govern Brittle Fracture and Cavitation Behavior in Metallic Glasses. Phys. Rev. Lett. 107.

Ning, Z., Khoubani, A., Evans, T.M., 2015. Shear wave propagation in granular assemblies. Comput. Geotech. 69, 615-626.

O'Sullivan, C., 2011. Particulate Discrete Element Modelling: A Geomechanics Perspective. Taylor & Francis.

Perdew, J.P., Burke, K., Ernzerhof, M., 1996. Generalized gradient approximation made simple. Phys Rev Lett 77, 3865-3868.

Picallo, C.B., Lopez, J.M., Zapperi, S., Alava, M.J., 2009. Optimization and Plasticity in Disordered Media. Phys Rev Lett 103.

Picallo, C.B., Lopez, J.M., Zapperi, S., Alava, M.J., 2010. From Brittle to Ductile Fracture in Disordered Materials. Phys Rev Lett 105.

Potyondy, D.O., Cundall, P.A., 2004. A bonded-particle model for rock. International Journal of Rock Mechanics and Mining Sciences 41, 1329-1364.

Ramberg, W., Osgood, W.R., 1943. Description of Stress-strain Curves by Three Parameters. National Advisory Committee for Aeronautics.

Rodriguez, P., 1984. Serrated plastic flow. Bulletin of Materials Science 6, 653-663.

Roux, J.-N., CHevoir, F., 2005. Discrete numerical simulation and the mechanical behavior of granular materials. Bulletin de Liaison des Laboratoires des Ponts et Chaussees 254, 109-138.

Rycroft, C.H., Bouchbinder, E., 2012. Fracture Toughness of Metallic Glasses: Annealing-Induced Embrittlement. Phys. Rev. Lett. 109, 194301.

Saad, Y., Schultz, M.H., 1986. Gmres - a Generalized Minimal Residual Algorithm for Solving Nonsymmetric Linear-Systems. Siam J Sci Stat Comp 7, 856-869.

Schuh, C.A., Hufnagel, T.C., Ramamurty, U., 2007. Overview No.144 - Mechanical behavior of amorphous alloys. Acta Mater. 55, 4067-4109.

Scudino, S., Jerliu, B., Pauly, S., Surreddi, K.B., Kühn, U., Eckert, J., 2011. Ductile bulk metallic glasses produced through designed heterogeneities. Scr. Mater. 65, 815-818.

Silling, S.A., 2000. Reformulation of elasticity theory for discontinuities and long-range forces. J. Mech. Phys. Solids 48, 175-209.

Simmons, G., Wang, H., 1971. Single crystal elastic constants and calculated aggregate properties: a handbook. M.I.T. Press.

Sun, B.A., Wang, W.H., 2015. The fracture of bulk metallic glasses. Prog. Mater. Sci. 74, 211-307.

Sun, S., Sundararaghavan, V., 2014. A peridynamic implementation of crystal plasticity. International Journal of Solids and Structures 51, 3350-3360.

Tandaiya, P., Ramamurty, U., Narasimhan, R., 2009. Mixed mode (I and II) crack tip fields in bulk metallic glasses. J Mech Phys Solids 57, 1880-1897.

Truszkowska, A., Yu, Q., Greaney, P.A., Evans, T.M., Kruzic, J.J., 2017. Developing a Crystal Plasticity Model for Metallic Materials Based on the Discrete Element Method. MRS Advances 2, 2609-2614.

Verlet, L., 1967. Computer Experiments on Classical Fluids .I. Thermodynamical Properties of Lennard-Jones Molecules. Phys Rev 159, 98-103.

Wang, Y.W., Li, M., Xu, J.W., 2016. Toughen and harden metallic glass through designing statistical heterogeneity. Scr. Mater. 113, 10-13.

Yilmaz, A., 2011. The Portevin-Le Chatelier effect: a review of experimental findings. Sci Technol Adv Mat 12.

Yun, T.S., Evans, T.M., 2010. Three-dimensional random network model for thermal conductivity in particulate materials. Comput. Geotech. 37, 991-998.

Yun, T.S., Evans, T.M., 2011. Evolution of at-rest lateral stress for cemented sands: experimental and numerical investigation. Granul. Matter 13, 671-683.

Zhang, F., Field, D.P., 2013. Characterization of Creep-Damaged Grain Boundaries of Alloy 617. Metall. Mater. Trans. A 44a, 4927-4936.

Zhang, H.Y., Zheng, G.P., 2014. Three-dimensional phase-field simulation on the deformation of metallic glass nanowires. J. Alloys Compd. 615, S102-S107.

Zhang, Y., Liu, J.P., Chen, S.Y., Xie, X., Liaw, P.K., Dahmen, K.A., Qiao, J.W., Wang, Y.L., 2017. Serration and noise behaviors in materials. Prog. Mater. Sci. 90, 358-460.

Zhang, Z.F., Eckert, J., Schultz, L., 2003. Difference in compressive and tensile fracture mechanisms of Zr59CU20Al10Ni8Ti3 bulk metallic glass. Acta Mater. 51, 1167-1179.

Zhao, M., Li, M., 2011. Local heating in shear banding of bulk metallic glasses. Scr. Mater. 65, 493-496.

Zhao, S.W., Evans, T.M., Zhou, X.W., Zhou, S., 2017. Discrete element method investigation on thermally-induced shakedown of granular materials. Granul. Matter 19, 11.

Zheng, G.P., Shen, Y., 2011. Simulation of shear banding and crack propagation in bulk metallic glass matrix composites. J. Alloys Compd. 509, S136-S140.

Zunger, A., Wei, S.H., Ferreira, L.G., Bernard, J.E., 1990. Special Quasirandom Structures. Phys Rev Lett 65, 353-356.

Appendix A. Analytic Model of Elasticity

Consider a DEM assembly that contains N_b parallel bonds per unit length, uniformly distributed over orientation, and with an average length l. The bonds have normal and shear stiffness that depend on orientation, $k_n\left(\hat{n}\right)$, and $k_s\left(\hat{n}\right)$ respectively. If the assembly is deformed with a homogeneous strain ε (and one assumes that deformation of the bonds is affine) then the displacement of a bond with orientation $\hat{n}$ is given by:

$$\mathbf{u} = l\left(\hat{n}\cdot\varepsilon\right) \qquad \text{A .1}$$

Where the displacement can be separated into normal and shear components:

$$u_n = \mathbf{u}\cdot\hat{n} = l\left(\hat{n}\cdot\varepsilon\right)\cdot\hat{n} \qquad \text{A .2}$$

and

$$u_s = \left|\mathbf{u} - u_n\hat{n}\right| = l\sqrt{\left(\hat{n}\cdot\varepsilon\right)\cdot\left(\hat{n}\cdot\varepsilon\right) - \hat{n}\left(\left(\hat{n}\cdot\varepsilon\right)\cdot\hat{n}\right)} \qquad \text{A .3}$$

The elastic energy stored in the deformed bond is:

$$\begin{aligned} E_b\left(\hat{n}\right) &= \frac{1}{2}k_n\left(\hat{n}\right)u_n^2 + \frac{1}{2}k_s\left(\hat{n}\right)u_s^2 \\ &= \frac{1}{2}l^2\left(k_n\left(\hat{n}\right) - k_s\left(\hat{n}\right)\right)\left(\left(\hat{n}\cdot\varepsilon\right)\cdot\hat{n}\right)^2 + \frac{1}{2}l^2k_s\left(\hat{n}\right)\left(\hat{n}\cdot\varepsilon\right)\cdot\left(\hat{n}\cdot\varepsilon\right) \end{aligned} \qquad \text{A .4}$$

Averaging over all orientations gives the total elastic energy density:

$$E_v = \frac{N_b}{4\pi}\int d\hat{n}E_b\left(\hat{n}\right) \qquad \text{A .5}$$

The elements of the elastic stiffness tensor C_{ijkl} are given by the second derivative of the elastic energy density so that:

$$C_{ijkl} = d_{ijkl}\frac{\partial^2 E_v}{\partial\varepsilon_{ij}\partial\varepsilon_{kl}} \qquad \text{A .6}$$

where d_{ijkl} is the multiplicity of the symmetry equivalent index combinations (so that for example $d_{1111}=1,\ d_{1122}=2,\ d_{1112}=4,\ d_{2323}=4,$ and $d_{2313}=8$).

Switching to the notation of the reduced stiffness matrix, we can compute the stiffness element C_{ij} by imposing a homogeneous strain state $\varepsilon = \eta_i\varepsilon^{(i)} + \eta_j\varepsilon^{(j)}$: the sum of two superimposed strains with magnitudes η_i and η_j along strain directions $\varepsilon^{(i)}$ and $\varepsilon^{(j)}$. The energy density of the assembly with this deformation is:

$$E_v = \frac{N_b l^2}{8\pi}\int d\hat{n}\left[\left(k_n - k_s\right)\left(\hat{n}\cdot\varepsilon\cdot\hat{n}\right)^2 + k_s\left(\hat{n}\cdot\varepsilon\right)\cdot\left(\hat{n}\cdot\varepsilon\right)\right]$$

$$= \frac{N_b l^2}{8\pi}\int d\hat{n}\left[\begin{array}{l}\left(k_n - k_s\right)\left(\begin{array}{l}\eta_i^2\left(\hat{n}\cdot\varepsilon^{(i)}\cdot\hat{n}\right)^2 + 2\eta_i\eta_j\left(\hat{n}\cdot\varepsilon^{(i)}\cdot\hat{n}\right)\left(\hat{n}\cdot\varepsilon^{(j)}\cdot\hat{n}\right)\\ +\eta_j^2\left(\hat{n}\cdot\varepsilon^{(j)}\cdot\hat{n}\right)^2\end{array}\right)\\ +k_s\left(\begin{array}{l}\eta_i^2\left(\hat{n}\cdot\varepsilon^{(i)}\right)\cdot\left(\hat{n}\cdot\varepsilon^{(i)}\right) + 2\eta_i\eta_j\left(\hat{n}\cdot\varepsilon^{(i)}\right)\cdot\left(\hat{n}\cdot\varepsilon^{(j)}\right)\\ +\eta_j^2\left(\hat{n}\cdot\varepsilon^{(j)}\right)\cdot\left(\hat{n}\cdot\varepsilon^{(j)}\right)\end{array}\right)\end{array}\right] \qquad \text{A .7}$$

Taking the second derivatives with respect to η gives:

$$C_{ii} = d_{ii}\frac{\partial^2 E_v}{\partial\eta_i^2} = \frac{N_b l^2}{8\pi}\int d\hat{n}\left[\left(k_n - k_s\right)\left(\hat{n}\cdot\varepsilon^{(i)}\cdot\hat{n}\right)^2 + k_s\left(\hat{n}\cdot\varepsilon^{(i)}\right)\cdot\left(\hat{n}\cdot\varepsilon^{(i)}\right)\right] \qquad \text{A .8}$$

$$C_{ij} = d_{ij}\frac{\partial^2 E_v}{\partial\eta_i\partial\eta_j}$$
$$= \frac{N_b l^2}{8\pi}\int d\hat{n}\left[\left(k_n - k_s\right)2\left(\hat{n}\cdot\varepsilon^{(i)}\cdot\hat{n}\right)\left(\hat{n}\cdot\varepsilon^{(j)}\cdot\hat{n}\right) + k_s 2\left(\hat{n}\cdot\varepsilon^{(i)}\right)\cdot\left(\hat{n}\cdot\varepsilon^{(j)}\right)\right] \qquad \text{A .9}$$

Appendix B. Proof of Cubic Elasticity from Spheroid Stiffness Distributions

Cubic elasticity requires that $C_{11} = C_{22} = C_{33} \neq 0$, $C_{12} = C_{21} = C_{13} = C_{31} = C_{23} = C_{32} \neq 0$, $C_{44} = C_{55} = C_{66} \neq 0$, all other elements are identically zero, and that $2C_{44} \neq C_{11} - C_{12}$. Each case will be considered separately, first showing that C_{11}, C_{12}, and C_{44} are non-zero and independent and then showing that C_{14} and C_{45} are identically zero. Finally, it will be shown that the symmetry of the stiffness functions k_n and k_s leads to equivalence between the symmetry related elastic constants in a cubic systems.

Demonstration that C_{11} is Non-zero

Considering strain path:

$$\varepsilon_1 = \begin{bmatrix}1 & 0 & 0\\ 0 & 0 & 0\\ 0 & 0 & 0\end{bmatrix} \qquad \text{B .10}$$

and direction $\hat{n}$ parameterized by polar angle, θ, and azimuthal angle, ϕ, the elastic constant C_{11} can be written as the integral:

$$C_{11} = \frac{N_b l^2}{4\pi} \int d\theta \sin(\theta) \int d\phi \begin{bmatrix} \left(k_n(\theta,\phi) - k_s(\theta,\phi)\right)\cos^4(\phi)\sin^4(\theta) \\ +k_s(\theta,\phi)\cos^2(\phi)\sin^2(\theta) \end{bmatrix} \neq 0 \qquad \text{B .11}$$

Demonstration that C_{12} is Non-zero

Considering the additional strain path:

$$\varepsilon_2 = \begin{bmatrix} 0 & 0 & 0 \\ 0 & 1 & 0 \\ 0 & 0 & 0 \end{bmatrix} \qquad \text{B .12}$$

one obtains:

$$C_{12} = \frac{N_b l^2}{4\pi} \int d\theta \sin(\theta) \int d\phi \left[\left(k_n - k_s\right)\sin^2(\phi)\cos^2(\phi)\sin^4(\theta) \right] \neq 0 \qquad \text{B .13}$$

where the angularly dependent stiffness functions have been written simply as k_n and k_s for the sake of brevity.

Demonstration that C_{44} is Non-zero

Using the strain path:

$$\varepsilon_4 = \begin{bmatrix} 0 & 0 & 0 \\ 0 & 0 & 1 \\ 0 & 1 & 0 \end{bmatrix} \qquad \text{B .14}$$

one obtains:

$$C_{44} = \frac{N_b l^2}{16\pi} \int d\theta \sin(\theta) \int d\phi \begin{bmatrix} \left(k_n - k_s\right)4\sin^2(\phi)\sin^2(\theta)\cos^2(\theta) \\ +k_s\left(\sin^2(\phi)\sin^2(\theta) + \cos^2(\theta)\right) \end{bmatrix} \neq 0 \qquad \text{B .15}$$

Demonstration that C_{14} is Identically Zero

Mixing the normal and shear deformation using the strain paths one obtains:

$$C_{14} = \frac{N_b l^2}{4\pi} \int d\theta \sin(\theta) \int d\phi \left[(k_n - k_s) 4 \sin(\phi) \cos^2(\phi) \sin^3(\theta) \cos(\theta) \right] = 0 \qquad \text{B .16}$$

The stiffness functions k_n and k_s are constructed to possess cubic symmetry (triad axes along $\langle 111 \rangle$) and so also posses mirror symmetry on the $\phi = 0$ plane. The term $\sin(\phi)\cos^2(\phi)$ is antisymmetric in ϕ and so the expression integrates identically to zero.

Demonstration that C_{45} is Identically Zero

Mixing shear deformations along different directions using the strain path:

$$\varepsilon_5 = \begin{bmatrix} 0 & 0 & 1 \\ 0 & 0 & 0 \\ 1 & 0 & 0 \end{bmatrix} = \frac{1}{2}\gamma_5 \qquad \text{B .17}$$

one obtains:

$$C_{45} = \frac{N_b l^2}{8\pi} \int d\theta \sin(\theta) \int d\phi \begin{bmatrix} (k_n - k_s) \sin(2\phi) \sin^2(\phi) \cos^2(\theta) \\ +k_s \sin(2\phi) \sin^2(\theta) \end{bmatrix} = 0 \qquad \text{B .18}$$

In this expression, $\sin(2\phi)$ is antisymmetric in ϕ and, as with C_{14}, the expression integrates identically to zero.

Demonstration that C_{11}, C_{12}, and C_{44} are Independently Tunable

For non-isotropic elasticity one requires that $2C_{44} \neq C_{11} - C_{12}$. Using the equations above:

$$C_{11} - C_{12} = \frac{N_b l^2}{4\pi} \int d\theta \sin(\theta) \int d\phi \begin{bmatrix} (k_n - k_s) \cos^2(\phi) \cos(2\phi) \sin^4(\theta) \\ +k_s \cos^2(\phi) \sin^2(\theta) \end{bmatrix} \neq 2C_{44} \qquad \text{B .19}$$

It can hence be seen by comparison of this with the equation for that C_{11}, C_{12}, and C_{44} must be independent.

Symmetry Relationships Between Stiffness Elements

The final task is to show that if k_n and k_s posses cubic symmetry, then the elastic constants also satisfy the cubic symmetry relations so that, for example, $C_{11} = C_{22} = C_{33}$. By possessing cubic symmetry, the stiffness function is invariant under a three-fold rotation about [111] so that:

$$k(\hat{n}) = k(\hat{n} \cdot L) \qquad \text{B .20}$$

where:

$$L = L_{3[111]} = \begin{bmatrix} 0 & 0 & 1 \\ 1 & 0 & 0 \\ 0 & 1 & 0 \end{bmatrix} \qquad \text{B .21}$$

is the transformation matrix for a three-fold rotation about [111] axis. Consider imposed normal strain along $\hat{y}$:

$$\varepsilon_2 = \begin{bmatrix} 0 & 0 & 0 \\ 0 & 1 & 0 \\ 0 & 0 & 0 \end{bmatrix} = L \cdot \varepsilon_1 \cdot L^{-1} \qquad \text{B .22}$$

so that C_{22} is given by:

$$C_{22} = \frac{N_b l^2}{8\pi} \int d\hat{n} \left[(k_n - k_s)(\hat{n} \cdot \varepsilon_2 \cdot \hat{n})^2 + k_s (\hat{n} \cdot \varepsilon_2) \cdot (\hat{n} \cdot \varepsilon_2) \right] \qquad \text{B .23}$$

Using the symmetry relationship, we can write this in terms ε_1, a normal strain path along $\hat{x}$:

$$C_{22} = \frac{N_b l^2}{8\pi} \int d\hat{n} \begin{bmatrix} (k_n - k_s)\left(\hat{n} \cdot \left(L \cdot \varepsilon_1 \cdot L^{-1}\right) \cdot \hat{n}\right)^2 \\ + k_s \left(\hat{n} \cdot \left(L \cdot \varepsilon_1 \cdot L^{-1}\right)\right) \cdot \left(\hat{n} \cdot \left(L \cdot \varepsilon_1 \cdot L^{-1}\right)\right) \end{bmatrix} \qquad \text{B .24}$$

Rearranging the order of these matrix products and substituting for $\hat{n}' = \hat{n} \cdot L$ gives:

$$C_{22} = \frac{N_b l^2}{8\pi} \int d\hat{n} \left[(k_n - k_s)(\hat{n}' \cdot \varepsilon_1 \cdot \hat{n}')^2 + k_s (\hat{n}' \cdot \varepsilon_1) \cdot (\hat{n}' \cdot \varepsilon_1) \right] \qquad \text{B .25}$$

and as $k_n(\hat{n}) = k_n(\hat{n} \cdot L) = k_n(\hat{n}')$ and $k_s(\hat{n}) = k_s(\hat{n} \cdot L) = k_s(\hat{n}')$, and the integral is performed over the full solid angle we see that:

$$C_{22} = \frac{N_b l^2}{8\pi} \int d\hat{n} \left[\left(k_n(\hat{n}') - k_s(\hat{n}') \right) \left(\hat{n}' \cdot \varepsilon_1 \cdot \hat{n}' \right)^2 + k_s(\hat{n}') \left(\hat{n}' \cdot \varepsilon_1 \right) \cdot \left(\hat{n}' \cdot \varepsilon_1 \right) \right] \qquad \text{B .26}$$

$$C_{22} = C_{11}$$

A similar approach can be used to prove the equivalence of the other symmetry related stiffness elements; however, this is left as an exercise for the reader.

Appendix C. Comparison of Analytic Model with DEM Model

As with the DEM simulation, a simple method for identifying the accessible elastic domain using the analytical model is to randomly sample the parameter space and plot the resulting cloud of elastic properties. The results are shown in Figure Fig. C.1(a). It can be seen that the domain is remarkably similar to that which is accessible by the DEM model presented in Figure 8. Also shown in Fig. C.1(b) is the deviation between the analytic model and the DEM model in both C_{12}/C_{11} and C_{44}/C_{11} for the case where Z>1. It can be seen that deviation of the models is lowest in C_{12}/C_{11} for high α_k and the reverse for C_{44}/C_{11}. It we assume that the deviation between the analytic and DEM models is due to the non-affine internal deformation in the DEM model, then we can see that an optimal choice of model parameters is to choose anisotropy factors a_n and a_s as close to 1 as possible, and choosing a_k to minimize the non-affine deformation of the assembly.

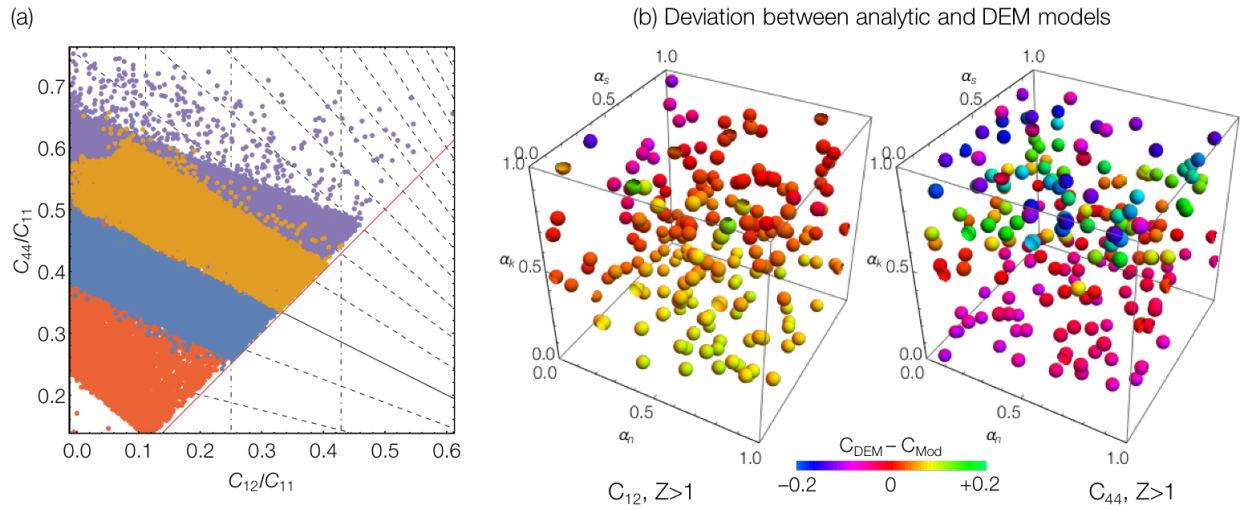

Figure C.1: (a) Domain of elasticity space accessible by spheroid based stiffness interactions demarked by plotting the elasticity from 10,000 randomly sampled points in the input parameter space. The blue and gold data is for the model using stiffness functions used in the DEM model, and it can be seen that the accessible domain is similar to the at in Figure 8 for the DEM model. The purple and orange data is generated using stiffness functions ad before but with the addition of correction terms from the addition of spheroids aligned along the <110> directions. (b) Deviation between the analytic model and DEM simulations plotted at 500 randomly sampled points of the log normalized input parameter space. Red is zero deviation.

Appendix D. Insights for expanding the accessible domain of elasticity

The accessible domain of elasticity space is enclosed in one direction by a line of constant Zener ratio and in the other by the Cauchy relationship $C_{12} = C_{44}$. The boundaries of accessible space of the DEM model are parallel to those of the analytic model, but while both models can achieve similar levels of elastic anisotropy, the DEM model can access a region considerably to the right of the $C_{12} = C_{44}$ boundary of the analytic model. That is, the analytic model cannot produce values of $C_{12} - C_{44} > 0$. To examine how the angular distributions of bond stiffness could be revised to push past the boundaries in Z and $C_{12} - C_{44}$, we can examine the integral equations that give rise to these quantities. The Zener ratio is given by:

$$Z = \frac{2\tilde{C}_{44}}{1-\tilde{C}_{12}} = \frac{\int d\hat{n}\left(\chi_n k_n + \chi_s k_s\right)}{\int d\hat{n}\left(\gamma_n k_n + \gamma_s k_s\right)} \qquad \text{D .27}$$

where the tilde denotes the dimensionless elastic stiffness element normalized by C_{11} and the functions χ and γ are

$$\begin{aligned}
\chi_n &= \sin^2(2\theta)\sin^2(\phi) \\
\chi_s &= \cos^2(\theta) - \sin^2(\theta)\left(2\cos(2\theta)+1\right)\sin^2(\phi) \\
\gamma_n &= 2\sin^4(\theta)\cos^2(\phi)\cos(2\phi) \\
\gamma_s &= -2\sin^2(\theta)\cos^2(\phi)\left(\sin^2(\theta)\cos(2\phi)-1\right)
\end{aligned} \qquad \text{D .28}$$

If we consider just the case for the Z > 0 model in which k_n peaked along $\langle 111 \rangle$ and k_s along $\langle 100 \rangle$, then to push the boundaries in Z, we wish to maximize the numerator of Z while minimizing its denominator. That is we wish to maximize the overlap of χ and *k* in the numerator, and minimize overlap of γ and *k* in the denominator. The functions χ and γ are plotted overlain with their respective stiffness functions in Figure D.1. From these figures it is clear that Z could be increased if k_n was altered so that bonds were stiffer for normal displacements along the $\langle 110 \rangle$ directions, and that k_s was varied to make bond softer in shear along $\langle 110 \rangle$. With the spheroid-based forms of k_n and k_s, it is not possible to independently tune the stiffness of the $\langle 110 \rangle$ directions, and thus the model predicts that the best next iteration of a stiffness function would include the flexibility to tune the stiffness in these directions as well. In the complementary direction the distance from the $C_{12} = C_{44}$ boundary is given by:

$$C_{12} - C_{44} = \int d\hat{n}\left(\zeta_n k_n + \zeta_s k_s\right) \qquad \text{D .29}$$

where:

$$\zeta_n = 2\sin^2(\theta)\sin^2(\phi)\left(\sin^2(\theta)\cos^2(\phi) - \cos^2(\theta)\right)$$
$$\zeta_s = \frac{1}{2}\left(\sin^4(\theta)\left(-\sin^2(2\phi)\right) + \sin^2(\theta)\left(2\cos(2\theta)+1\right)\sin^2(\phi) - \cos^2(\theta)\right) \quad \text{D .30}$$

These are also plotted in Figure D.1. The function ζ_n has maxima along the $\langle 110 \rangle$ directions, but is antisymmetric, and so the overlap with k_n integrates to zero. The term ζ_s is negative for all directions, and so the integral of its overlap with k_s is also negative. This means that not only is $\tilde{C}_{12} - \tilde{C}_{44}$ always less than or equal to zero, there is no change that can be made to the stiffness functions that will make $\tilde{C}_{12} - \tilde{C}_{44} > 0$ while still possessing cubic symmetry in k_n and k_s. This makes it all the more remarkable that the DEM model is able to obtain values of $\tilde{C}_{12} - \tilde{C}_{44}$ in excess of 0.1. We attribute this to a not overly redundant bond network permitting non-affine deformation of the assembly.

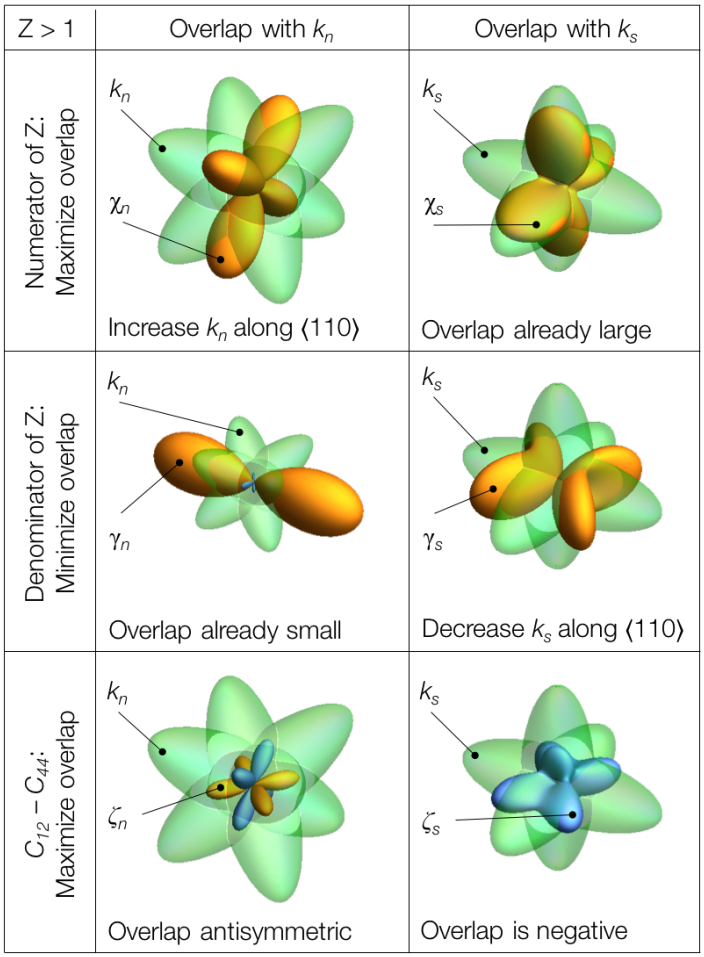

Figure D.1: The overlap kernels for the integrals for F and $\tilde{C}_{12} - \tilde{C}_{44}$ for the Z model. Bond stiffness functions are plotted as a translucent green surface. For the other function positive values are plotted in gold, and negative values in blue. The left-hand column is for the integral of the normal stiffness, and the right column for the shear stiffness. The top row is for the kernels in the integrals of the numerator of Z, the middle row for the terms in it denominator. Expanding the boundary of the accessible domain in Z requires maximizing the top row and minimizing the middle row. The bottom row shows the kernels of the integrals in $\tilde{C}_{12} - \tilde{C}_{44}$. The integral over k_n is identically zero by symmetry, and as function weighting the integral over k_s is everywhere negative $\tilde{C}_{12} - \tilde{C}_{44} \leq 0$, and there is no change to the stiffness functions consistent with the cubic symmetry that will ever make $\tilde{C}_{12} - \tilde{C}_{44}$ positive.